UNIVERSIDAD DE OVIEDO

Programa de Doctorado en Enería y Control de Procesos

DOCTORAL THESIS

High Capacity Cooling of Small Cavities with Swirl-Creating Geometries

PhD Candidate:

Matthias Feiner, M.Sc.

Karlsruhe and Gijón, 2022

RESUMEN DEL CONTENIDO DE TESIS DOCTORAL

1.- Título de la Tesis	
Español/Otro Idioma: Refrigeración de alta capacidad de pequeñas cavidades con geometrías que crean remolinos	Inglés: High Capacity Cooling of Small Cavities with swirl-creating Geometries

2.- Autor	
Nombre: Matthias Helmut Feiner	DNI/Pasaporte/NIE:
Programa de Doctorado: Energía y Control de Procesos	
Órgano responsable: Centro Internacional de Postgrado	

RESUMEN (en español)

Desde el comienzo de la revolución industrial, los ingenieros se proponen mejorar los procesos de producción para ahorrar tiempo, dinero y energía. Este desarrollo ha dado lugar a máquinas y componentes más compactos y potentes. Por tanto, la disipación de energía requiere de mayores flujos de calor. Con la tendencia a la miniaturización, las superficies de refrigeración disponibles son cada vez más pequeñas. Debido a ambas tendencias, en el futuro se necesitarán procesos de refrigeración cada vez más eficaces. Un enfoque actual para este reto es el llamado evaporador puntual. En el evaporador puntual, el refrigerante se pulveriza desde un tubo capilar en un orificio ciego y se expulsa en dirección opuesta a la de inyección. Con esta tecnología es posible disipar altos flujos de calor de hasta 1000-1500 kW/m². La desventaja de este proceso de refrigeración es su eficiencia comparativamente baja, ya que alrededor del 50-80% del refrigerante sale del proceso sin evaporar. La eficiencia debe aumentarse ampliando el recorrido del refrigerante a través del evaporador. Esto se consigue forzando una trayectoria helicoidal del refrigerante en el evaporador. Este tipo de evaporador se llama evaporador helicoidal o de remolino.

El diseño de este proceso requiere métodos para describir el área de secciones pequeñas de evaporadores helicoidales con diámetros hidráulicos pequeños, gradientes bajos y radios de curva ajustados, que actualmente no están disponibles. El objetivo de la investigación es cubrir esta falta de conocimiento y encontrar métodos para describir matemáticamente la transferencia de calor, pérdida de presión y el flujo de calor crítico. Esto debería permitir a otros ingenieros diseñar evaporadores de remolino para su aplicación específica de forma eficiente en tiempo y coste. Para describir la caída de presión, la transferencia de calor y el flujo de calor crítico en el evaporador de remolino, se dividió el evaporador en sus regímenes de flujo hidráulicamente activos. Se investigaron, aplicaron y verificaron experimentalmente los métodos para cada régimen. Se desarrollaron métodos y se encontraron modelos para calcular los procesos en el evaporador de remolino y la eficiencia se incrementó en un 60% en comparación con el evaporador puntual. En la transferencia a la aplicación, se introdujo un evaporador de remolino en un portaherramientas. Esto permitió que la herramienta de corte se enfriara internamente durante el proceso de torneado. Esta medida ha reducido a la mitad el desgaste de la herramienta. Como resultado, se puede duplicar la velocidad del proceso o la vida útil de la herramienta.

SR. PRESIDENTE DE LA COMISIÓN ACADÉMICA DEL PROGRAMA DE DOCTORADO EN ENERGÍA Y CONTROL DE PROCESOS

RESUMEN (en Inglés)

Since the beginning of the industrial revolution, engineers are aiming to improve production processes to save time, money and energy. This development led to more compact and powerful machines and components. Thus, energy dissipation involves higher heat fluxes. With the trend towards miniaturization, the available cooling surfaces are becoming even smaller. Due to both tendencies, more and more efficient cooling processes will be required in future. A current approach to this challenge is the so-called spot evaporator. In the spot evaporator refrigerant is sprayed from a capillary tube into a blind hole and exhausted against the direction of injection. With this technology it is possible to dissipate high heat flows up to 1000-1500 kW/m². The disadvantage of this cooling process is the comparatively low efficiency, since about 50-80 % of the refrigerant exits the process unevaporated. The efficiency is to be increased by extending the evaporator path of the returning refrigerant. This is achieved by returning the refrigerant in a helical evaporator path. This kind of evaporator is called a swirl evaporator.

The design of this process asks for methods to describe the area of short helical evaporator sections with small hydraulic diameters, low gradients and tight curve radii, which are currently not available. The research question aims at closing this gap and finding methods to describe heat transfers, pressure losses and the critical heat flux mathematically. This should enable other engineers to design swirl evaporators for their specific application in a time and cost-efficient manner. In order to describe the pressure drop, heat transfer, and critical heat flux in the swirl evaporator, the evaporator was divided into its hydraulically active flow regimes. Methods for each regime were researched, applied and then verified in experiments. Methods were developed and models were found to calculate the processes in the swirl evaporator and the efficiency was increased by 60% compared to the spot evaporator. In the transfer to the application, a swirl evaporator was introduced into a tool holder. This allowed the cutting tool to be cooled internally during the turning process. This measure has halved the tool wear. As a result, either the process speed or the tool life can be doubled.

SR. PRESIDENTE DE LA COMISIÓN ACADÉMICA DEL PROGRAMA DE DOCTORADO EN ENERGÍA Y CONTROL DE PROCESOS

High Capacity Cooling of Small Cavities with Swirl-Creating Geometries

Doctoral Thesis

of

Matthias Feiner, M.Sc.
born on 18.08.1987 in Herbolzheim, Germany

Director:	Prof. Dr.-Ing. Francisco Javier Fernández García
Co-Director:	Prof. Dr.-Ing. Martin Kipfmüller

Acknowledgement

I would like to take the opportunity to thank all those who have inspired, influenced and supported me far beyond creating this thesis. I am happy and grateful to have met you, to have worked with you and even to call some of you my close friends. Prof. Dr. Michael Arnemann, for the years of supervision, from the bachelor thesis to the doctorate. He always stood by my side with advice and support. Prof. Dr. Martin Kipfmüller, for the opportunity to write my doctoral thesis at the institute and for always supporting me. Many thanks for establishing contact with the partner university. Prof. Dr. Francisco Javier Fernández García for the supervision at the University of Oviedo. Our good conversations, advice and impulses of a professional and life philosophical nature. At times when I was struggling, he immediately understood and coached me to overcome the obstacle. Helping me to help myself. I hope to be able to continue working with you for many years to come and to further strengthen international collaboration through joint research, industry and teaching projects. I thank my IMP colleagues for the good atmosphere at the institute and our weekly after-work beers. Dr. Tobias Knipping for outstanding pioneer work in the field of near-contour cooling, the construction of the test stand and years of coaching: initially as a boss and later as a friend. One of my closest friends Timo Müller, for awakening my interest in refrigeration technology and its process simulation many years ago and for creating and training my deeper understanding of thermodynamic processes through long conversations and discussions. Mathias Fauth for his contribution to the scroll evaporator and helping with all production engineering issues. Matthias Risto and Szimonetta Matus for their support in manufacturing issues. Matthias, your erosion know-how made it possible to get holes in screws and to manufacture the swirl evaporator. Szimonetta, your commitment in the production of all test bench relevant components remains unforgotten and I thank you both very much. Oliver Hügel from Pforzheim University for the fast, unbureaucratic and great support in micro casting. Bernd Nonnenmacher and Knut Heitzmann of the company Nonnenmacher GmbH for the production of further swirl evaporators in the micro casting process with impressive quality. Norbert Nietzig from the company Endress and Hauser GmbH, for the donation of the coriolis mass flow meter. Marius Benkler, for his support as scientific assistant. Whether weekends, holidays and late at night. Marius, your commitment remains unforgotten. Many thanks also to Luca Keller for years of very good cooperation. The same is true for Alexander Cuzmanov. Thanks also to Tobias Klein, who delivered the most impressive bachelor project thesis I have ever supervised. Other notable works included those by Maximilian Seibt, Alexander Häusler, Imke Hille and Alexander Kitzbichler. You, too, deserve my great gratitude. I am deeply grateful to Markus Hirtler, who took me under his intellectual wing very early in my secondary school years and supported me all the way to my master's degree. Many thanks for the years of friendship. Above all, my deepest gratitude goes to my wife and family. To my parents Birgit and Silvio, thank you for always being there for me and always supporting me. In your values education has a very high status and this work and my whole way there is the fruit of this philosophy. I thank my sister Cathrin for many things, especially for the constructive advice and editing of almost all my scientific texts, since high school. My wife Claudi, I thank you for the support over all these years, without you I would not be the man I am.

Abstract

Since the beginning of the industrial revolution, engineers are aiming to improve production processes to save time, money and energy. This development led to more compact and powerful machines and components. Thus, energy dissipation involves higher heat fluxes. With the trend towards miniaturization, the available cooling surfaces are becoming even smaller. Due to both tendencies, more and more efficient cooling processes will be required in future. A current approach to this challenge is the so-called spot evaporator. In the spot evaporator refrigerant is sprayed from a capillary tube into a blind hole and exhausted against the direction of injection. With this technology it is possible to dissipate high heat fluxes up to $1000-1500\,\mathrm{kW/m^2}$. The disadvantage of this cooling process is the comparatively low efficiency, since about $50-80\,\%$ of the refrigerant exits the process unevaporated. The efficiency is to be increased by extending the evaporator path of the returning refrigerant. This is achieved by returning the refrigerant in a helical evaporator path. This kind of evaporator is called a swirl evaporator.

The design of this process asks for methods to describe the area of short helical evaporator sections with small hydraulic diameters, low gradients and tight curve radii, which are currently not available. The research question aims at closing this gap and finding methods to describe heat transfers, pressure losses and the critical heat flux mathematically. This should enable other engineers to design swirl evaporators for their specific application in a time and cost-efficient manner. In order to describe the pressure drop, heat transfer, and critical heat flux in the swirl evaporator, the evaporator was divided into its hydraulically active flow regimes. Methods for each regime were researched, applied and then verified in experiments. Methods were developed and models were found to calculate the processes in the swirl evaporator and the efficiency was increased by $60\,\%$ compared to the spot evaporator. In the transfer to the application, a swirl evaporator was introduced into a tool holder. This allowed the cutting tool to be cooled internally during the turning process. This measure has halved the tool wear. As a result, either the process speed or the tool life can be doubled.

Resumen

Desde el comienzo de la revolución industrial, los ingenieros se proponen mejorar los procesos de producción para ahorrar tiempo, dinero y energía. Este desarrollo ha dado lugar a máquinas y componentes más compactos y potentes. Por tanto, la disipación de energía requiere de mayores flujos de calor. Con la tendencia a la miniaturización, las superficies de refrigeración disponibles son cada vez más pequeñas. Debido a ambas tendencias, en el futuro se necesitarán procesos de refrigeración cada vez más eficaces. Un enfoque actual para este reto es el llamado evaporador puntual. En el evaporador puntual, el refrigerante se pulveriza desde un tubo capilar en un orificio ciego y se expulsa en dirección opuesta a la de inyección. Con esta tecnología es posible disipar altos flujos de calor de hasta 1000-1500 kW/m². La desventaja de este proceso de refrigeración es su eficiencia comparativamente baja, ya que alrededor del 50-80% del refrigerante sale del proceso sin evaporar. La eficiencia debe aumentarse ampliando el recorrido del refrigerante a través del evaporador. Esto se consigue forzando una trayectoria helicoidal del refrigerante en el evaporador. Este tipo de evaporador se llama evaporador helicoidal o de remolino.

El diseño de este proceso requiere métodos para describir el área de secciones pequeñas de evaporadores helicoidales con diámetros hidráulicos pequeños, gradientes bajos y radios de curva ajustados, que actualmente no están disponibles. El objetivo de la investigación es cubrir esta falta de conocimiento y encontrar métodos para describir matemáticamente la transferencia de calor, pérdida de presión y el flujo de calor crítico. Esto debería permitir a otros ingenieros diseñar evaporadores de remolino para su aplicación específica de forma eficiente en tiempo y coste. Para describir la caída de presión, la transferencia de calor y el flujo de calor crítico en el evaporador de remolino, se dividió el evaporador en sus regímenes de flujo hidráulicamente activos. Se investigaron, aplicaron y verificaron experimentalmente los métodos para cada régimen. Se desarrollaron métodos y se encontraron modelos para calcular los procesos en el evaporador de remolino y la eficiencia se incrementó en un 60% en comparación con el evaporador puntual. En la transferencia a la aplicación, se introdujo un evaporador de remolino en un portaherramientas. Esto permitió que la herramienta de corte se enfriara internamente durante el proceso de torneado. Esta medida ha reducido a la mitad el desgaste de la herramienta. Como resultado, se puede duplicar la velocidad del proceso o la vida útil de la herramienta.

Contents

List of Figures

List of Tables

Nomenclature

Latin Formula Symbols

a	$\mathrm{m^2/s}$	Thermal diffusivity
A	$\mathrm{m^2}$	Area
A_{HT}	–	Factor for calculating heat transfer in the spray
A_{Nu}	–	Correlation factor for the Nusselt-number-Correlation
B	–	Factor for pressure drop and heat transfer calculation in spray
B_{Nu}	–	Correlation factor for the Nusselt number
c	m/s	Flow velocity
c_{p}	$\mathrm{J/(kg \cdot K)}$	Isobaric specific heat capacity
C_{Nu}	–	Correlation factor for the Nusselt-number-Correlation
d	m	Diameter
D	m	Pipe diameter
Dev	–	Deviation
D_{i}	–	Inner diameter
e	–	Error
f	–	Pipe friction factor of a pipe
F	–	Factor for rib properties (fin factor) swirl-band
Fr	–	Froude number
F_{ts}	m	Surface and material properties factor of the twisted strip
g	$\mathrm{m/s^2}$	gravitational constant
G	$\mathrm{kg/(s \cdot m^2)}$	Mass flux
h	J/kg	Specific enthalpy
k_1	–	Correction factor to increase in axial velocity
k_{slip}	–	Velocity ratio
K_1	–	Correction factor of the heat transfer
K_2	–	Correction factor, iterative calculation
l	m	length
l_{wk}	m	Distance between capillary outlet and cooling wall
m	–	Experimental factor
$\dot{m}$	kg/s	Mass flow
m_{hf}	–	Factor heat flow calculation spray
M	mol	Molar weight
ME	–	Mean error
MAE	–	Mean absolute error
Meas	–	Measured value
n	–	Number of revolutions of the swirl
N	–	Number
Nu	–	Nusselt number
p	bar	Pressure
P	mm	Pitch
Pr	–	Prandtl number
Pred	–	Predicted value

$\dot{q}$	W/m^2	Heat flux
$\dot{Q}$	W	Heat flow
r	m	radius
Re	$-$	Reynolds number
T	K	Temperature
u	J/kg	Specific internal energy
U	m	Perimeter
v	m^3/kg	Specific volume
$\dot{V}$	m^3/s	Volume flow
w	J/kg	Specific work
We	$-$	Weber number
x	$-$	Vapor quality
X_p	$-$	Factor for pressure calculation in spray
X_tt	$-$	Lockhart–Martinelli parameter
y	$-$	Pitch at 180° rotation related to the diameter of the screw
z	m	Geodetic height

Greek Formula Symbols

α	W/(m$^2 \cdot$ K)	Heat transfer coefficient
β	1/K	Coefficient of volumetric expansion
Δ	$-$	Difference
ε	$-$	Void fraction
η	kg/(m $\cdot$ s)	Dynamic viscosity of a fluid
γ	$-$	Factor for calculation the pressure drop in spray
κ_slip	$-$	Correlation factor for pressure drop
Λ	$-$	Volume fraction
λ	W/(m $\cdot$ K)	Thermal conductivity
ν	m^2/s	Kinematic viscosity
Φ	°	Angle between capillary and socket wall in degrees
Φ_gd	$-$	Two-phase factor according to Grönnerud
Φ_L	$-$	Two phase factor for pressure drop, calculated with liquid phase properties
Ψ	$-$	Factor pressure drop calculation Swirl 2-phase
ϱ	kg/m^3	Density
σ	N/m	Surface tension
σ_ar	$-$	Area ratio
Θ	rad	Angle between capillary and socket wall in radiant
Θ_spray	rad	Spray angle
ζ	$-$	Pressure drop coefficient

Indices

′	Belonging to the boiling curve
″	Belonging to the saturated vapor line
1ph.	Concerning the 1-phase state
2ph.	Concerning the 2-phase state
abs	Absolute
b	Nucleate boiling
bore	bore
c	Convective boiling
cap	Belonging the capillary
CHF	Critical heat flux
chip	Belonging to the chip area
con	Condensing
crit	Belonging the critical condition of a refrigerant
cut	Belonging to the cut area
dyn	Dynamic
eq	Equilibrium
evap	Evaporation
factors	Factors
f	Belonging the fluid part
frict	Friction
G	Belonging the gaseous part
hom	Homogeneous
hv	Belonging enthalpy of vaporization
hyd	Belonging to the hydraulic diameter
i	Counting index of the operating conditions
i	Inner
in	Inlet
levels	Levels
LG	Belonging the Evaporation enthalpy
LHF	Leidenfrost Heat Flux
L	Belonging the liquid phase
m	Measured
M	Concern an averaged state or mixture
mom	Momentum
Nu	Nusselt number
out	Outlet
pool	Pool boiling
real	Real
s	Surface
sim	Simulation
spray	Belonging the spray
sp	Single phase
stat	Statistic
sto	Stochastic
sub	Subcooling
swirl	Belonging the swirl
sys	Systematic
total	Total

w	Belonging the wall temperature
wk	Distance between capillaries and socket front wall
wsh	Wall superheat

Abbreviations

A/D	Analog/Digital
CBN	Cubic Boron Nitride
CHF	Critical heat flux
CPU	Central Processing Unit
DNB	Depature from Nucleate Boiling
EES	Engineering Equation Solver (Software)
FEM	Finite Elements Method
GPU	Graphics Processing Unit
GWP	Global Warming Potential
HKA	Hochschule Karlsruhe University of Applied Sciences
ODP	Ozone Depletion Potential

1. Introduction

Cooling of a high heat flux is already of great importance in many technical areas today and will continue to be in the future. Due to the progress of miniaturization, larger heat loads must be cooled on smaller heat-transferring surfaces. According to Moore's law [99], the number of transistors on a microchip doubles approximately every two years. This means that after ten years, the performance will increase by the factor of 32. So it is reasonable to assume that a device one is holding in his or her hands will be 32 times as powerful in ten years' time as it is today. A higher power consumption consequently results in a higher cooling load, since for example, all electrical current (pure exergy) is converted into heat at some point in the processor and must then be dissipated, so that the component to be cooled does not suffer any damage. But it is not only in computer science and electrical engineering that process-oriented cooling of high heat fluxes will play an increasingly important role; process-oriented cooling is also gaining ground in the more traditional fields of mechanical engineering and production technology.

1.1. Motivation

According to Westkämper a high thermal stability is required for continuous improvement of modern production processes to achieve reproducible results [138, p. 67]. There is also a trend towards miniaturization to make tools and products lighter and less expensive. This tendency results in the challenge that the heat load remains constant or increases while the available heat transferring surface is continuously decreasing. Examples of this are injection moulding, the cooling of electrical motors or the machining of nickel-based alloys. One possibility to fulfill the new cooling requirements is the so-called "spot evaporator". A schematic sketch of the spot evaporator is shown in Figure 1.1. This type of evaporator has the advantage of precise positionability in the thermally loaded components. In the spot evaporator, refrigerant is sprayed through a capillary tube onto the face of the blind hole. After that the refrigerant moves in a kind of annular gap against the direction of injection. The arrows indicate the direction of flow.
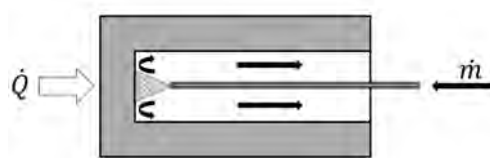
Figure 1.1.: Schematic sketch of a spot evaporator [44]

The spot evaporator has been investigated at the Institute of Materials and Processes (IMP) for about 10 years and has been used in a number of technical applications. Hot spots in injection molding have been cooled with spot evaporators, thus increasing productivity by significantly reducing the cooling time of the plastic [64, 129]. Figure 1.2 shows a schematic illustration of hot spot cooling with a spot evaporator during injection molding.
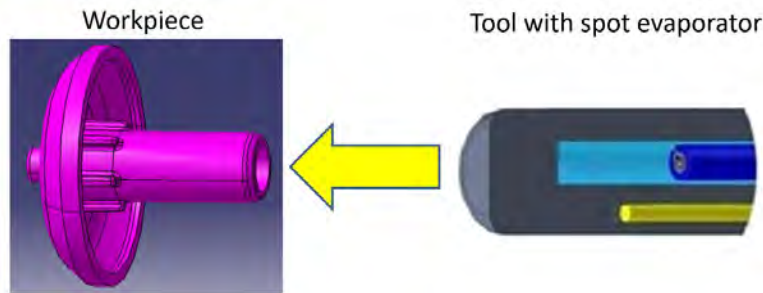
Figure 1.2.: Hot spot cooling with a spot evaporator during injection molding [77]

A further application of the spot evaporator is the cooling of stators of linear motors. It has been shown that in the cooled linear motor, the maximum holding force in continuous operation is increased by 50 % compared to water cooling. Compared to a non-cooled motor, the holding force could even be increased by 300 %. It has been proven that cooling is particularly useful for currents up to 8 A. At higher currents, the thermal resistance of the motor is reduced and the thermal behavior is dominated by the thermal mass of the rotor and the cooling in the ferrite core has only a subordinate influence [79]. A picture of a CAD design of a linear motor cooled with spot evaporators is shown in Figure 1.3.
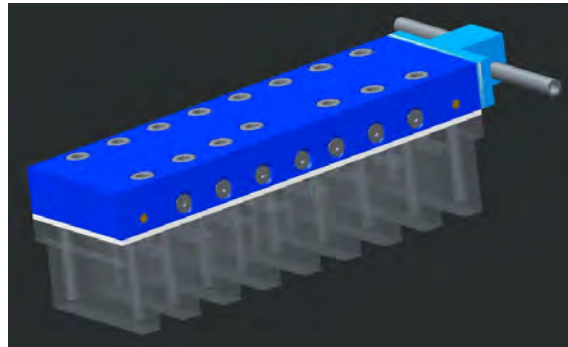
Figure 1.3.: CAD design of a linear motor cooled with spot evaporators [78]

One other innovative area of application is the internal cooling of indexable inserts during the turning process. The cutting temperature raises with the content of nickel increasing and the tool notch wear is extended along with the hardness increasing [42]. Therefore, it is necessary to cool the process in order to reduce wear. Figure 1.4 shows the hard turning process with the cutting material cubic boron nitride (CBN). The high dissipation of heat via the chip causes the flying sparks.

Main advantages of the spot evaporator are its ease of manufacture and the high heat transfer of more than $30.000 \, \text{W/m}^2\text{K}$ at the front surface of the bore provided by spray cooling. Spray cooling also allows cooling with heat fluxes above the critical heat flux for pool boiling [105, 25] and is therefore very suitable for cooling spot-shaped surfaces and hot spots, as they occur during injection molding.

However, turbulence of the evaporating fluid in the backflow path causes a relatively high pressure loss. A further disadvantage of the spot evaporator is that only $20-50 \, \%$ of the refrigerant evaporates before the critical heat flux is exceeded [75]. This also means

Figure 1.4.: Hard turning of a nickel-based alloy (Inconel 718) with the cutting material CBN [109]

that the two-phase refrigerant must be fully evaporated and superheated in an additional component (the post-evaporator) before it can be fed into the compressor. Since longer evaporator sections[1] tend to evaporate more refrigerant, a helical geometry was added to the spot evaporator to achieve this. According to Hardik [59], the pressure drop of two-phase flows in a helical evaporator geometry is lower than in a straight evaporator section. This issue was first explored by Humpfer [63] by axially drill-eroding a screw and inserting it into a spot evaporator. Due to the flow pattern in the backflow of the bore, this evaporator/heat exchanger structure is called a "swirl evaporator" [2]. A sketch of the swirl evaporator is shown in Figure 1.5.
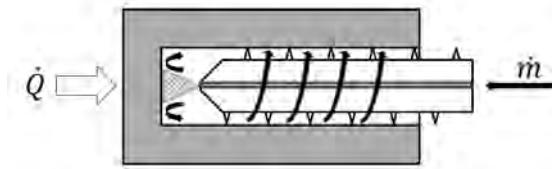
Figure 1.5.: Schematic sketch of a swirl evaporator [44]

1.2. Knowledge Gap

The literature on heat transfer phenomena in small (hydraulic) diameter helical evaporator geometries is rather rare compared with other fields of heat transfer. Helical coils were studied here because they are closest to the physics of the screw or helical evaporator geometry in the swirl evaporator. The evaporators studied in the literature typically have a coil diameter d_{Coil} between 50 and 300 mm and hydraulic diameters typically 5 – 9 mm. The fluid is usually water at high pressures, as they are applications for steam generators in power plants. Due to their coil shape, they can compensate well for material-specific thermal expansion. Because of their relatively compact design, they can also be

---

[1]An evaporator section is the distance or length of the section in which the refrigerant evaporates.

[2]Perhaps a more appropriate name for this evaporator structure would have been "spot-helical evaporator", since it cools the face of the bore with spray cooling and then the refrigerant flows back in a helical shape. In order not to break with terminology from previous work and publications [64, 44, ?, 46], the name swirl evaporator was retained in this work.

considered for special applications in aerospace. However, it is rather difficult to find scientifically relevant literature in this field. The literature for smaller hydraulic diameters ($d_{hyd} = 1\,mm$) and refrigerant as fluid is mentioned in the research of Elsayed [40] with R-134a and Kim et. al with R-22 [70, 71, 72].

In the coils studied in literature, the fluid is typically liquid and subcooled when introduced into the evaporator section. In swirl evaporators, it is two-phase and turbulent due to the preceding spray cooling as well as the redirection of the jet. For a better understanding of the geometrical parameters of coils/swirls/helical geometries they are displayed in Figure 1.6.
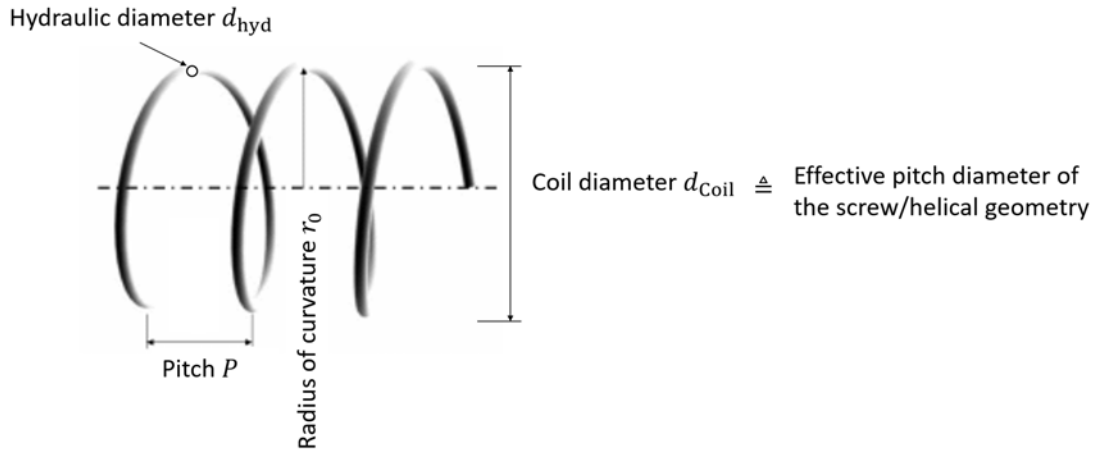
Figure 1.6.: Geometrical descriptions of the coil/helical geometry (mod. from [8])

In swirl evaporators, the coil diameter is $4.5\,mm$ and the pitch is between $1-5\,mm$, resulting in a relatively narrow curve radius, which, due to the high radial acceleration, has a reinforcing effect on the secondary flow. This effect is further enhanced by the lower evaporating pressures compared to steam generators. Furthermore, no work is known in which R-32[3] was used as refrigerant[4]. The length of the heated coil defines the length of the evaporator section, i.e. how long the section is in which the refrigerant evaporates. In literature, a distinction is made between the heated length of short, medium and long coils [57]:

- Short coil: $450-650\,mm$

- Medium coil: $900-1100\,mm$

- Long coil: $1400-2200\,mm$

The swirl evaporator however has a heated coil length between $200-400\,mm$, depending on the pitch of its helix or screw geometry. The coil length is the length of the uncoiled or unwound coil wire or in case of the swirl evaporator the length of the evaporator section. Although there are a number of methods to determine the heat transfer coefficient in a coil, most of these correlations are valid in a limited range of applications (limited to a particular fluid, mass flow or heat flux). However, in order to design a swirl evaporator, it

---

[3]R-32 also CH_2F_2 or difluoromethane, also difluoromethylene or HFC-32 Methylene Fluoride.

[4]The refrigerant R-32 was used in this work in order to establish comparability with the work of Knipping and the spot evaporators. A detailed justification for the use of R-32 refrigerant can be found in the thesis of Knipping [75, p. 31 – 38], a short summary in Section 3.1 of this thesis.

is extremely important to find a correlation that describes heat transfer phenomena. The research question therefore arises from the listed lack of previous knowledge:

- Small hydraulic diameter coil $d_{hyd} < 1\,\mathrm{mm}$

- R-32 as refrigerant

- Narrow curve radius at low pressures $\longrightarrow$ strong secondary flow

- Very short coil

- Low pitch of coil/screw/helical evaporator geometry

- Two-phase entry into the helical evaporator section

1.3. Objectives

This work is intended to make a fundamental contribution to the understanding of swirl evaporators in technical applications. A key role plays the relationship between the number of threads in the bore and the hydraulic diameter of the helical evaporator section. The smaller the hydraulic diameter, the higher the heat transfer coefficient at constant mass flow, since the mass flux and thus the flow velocity and Reynolds number increase.
In order to make the processes in the swirl evaporator calculable and visualizable, a model should be developed and evaluated which is based on physical principles. So it should be possible afterwards to design an industrial swirl evaporator for the respective application at the right performance. The equations enable optimization of a swirl evaporator regarding to pressure drop or heat transfer. The approach of this work is as follows:

1. Performing the experimental investigation of the swirl evaporator. Obtain a sufficient amount of data for
   a) comparison with the calculated results and
   b) optimization of the process.

2. Determining different hydraulically active parts and their roles in heat transfer and pressure drop. Then comparing these parts with models available in the scientific literature and verify them with experiments. The comparisons were made in the areas of
   a) pressure drop in parts of the swirl evaporator,
   b) critical heat flux for spray cooling and nucleated boiling in the swirl evaporator,
   c) heat transfer in the swirl evaporator and
   d) elaboration of FEM models of conduction,
      - to support the calculation of the heat flux dissipated by the system and
      - for indirect measurement of the heat transfer coefficient.

3. Optimizing of cooling capacity, reduction of energy consumption and use of refrigerants with low global warming potential.

4. Using the swirl evaporator in a real industrial application for the internal cooling of a cutting tool for the machining of nickel-based alloy (such as Inconel 718).

The main goal of this work is the research, development and validation of simulation models in order to be able to design swirl evaporators for industrial applications in a time- and cost-efficient manner.

1.4. Structure of Work

The structure of this work reflects the chronological sequence in which the swirl evaporator was investigated. The aim was to make the swirl evaporator calculable and designable for a wide range of industrial applications. This structure is displayed in Figure 1.7. The first Chapter presents the underlying motivation and places the work in the context of previous research at the University of Applied Sciences Karlsruhe (HKA). The goals and the necessary work steps are structurally presented. Chapter 2 describes the underlying physical principles of the spot and swirl evaporator. Here, the individual assemblies of the swirl and spot evaporator are described. The assemblies are further subdivided into regimes and subregimes in order to describe the pressure drop and heat transfer with empirical correlations. Previous works are described, their theoretical models as well as their experiments and experimental results. In Chapter 3 the correlation-based models are developed and described. Chapter 4 describes the test rig and the measurement equipment used in this thesis. It also describes the methodology and the model used to determine the heat transfer coefficients in the swirl evaporator. In Chapter 5 the experimental results are compared with the results from the simulation. In the 6th Chapter, the swirl evaporator is applied in an industrial application. It was introduced into a turning tool in order to cool the cutting edge of the tool from the inside during the machining of nickel-based alloy such as Inconel 718. In the last Chapter (7), the main conclusions are exposed that were obtained from the research results and discussion and an outlook on future work is given.

1. Introduction
Motivation – Initial situation and problem statement – Purpose, scope and structure of the thesis

2. Physical Principles and Emperical Correlations
Analysis of the current situation – Theoretical framework – Previous work – Research question

3. Development of the Models
Model building – Description of the algorithm –FEM- model for inverse calculation of the heat transfer coefficient

4. Experimental Examination
Experimental device – Experimental setup and execution – Screening tests – Experimental procedure

5. Results and Discussion
Validation of the simulation models – Discussion of the results

6. Transfer to Application Case
Use of a swirl evaporator for internal cooling of a turning tool for the turning of nickel-based materials

7. Conclusion and Future Work
Summary – Outlook– Patent spiral surface evaporator

Figure 1.7.: Work structure

2. Physical Principles and Empirical Correlations

Since industrialization, engineers have been concerned with handling high heat flux. For example in steam generators in steam engines, locomotives or in conventional or nuclear power plants. For the optimal generation of evaporation processes, knowledge in the field of heat transfer and boiling processes of liquids is indispensable, regardless of whether it is a power plant process or a cooling process, since they are identical in their physical principles. Therefore, a lot of research has been done in the last 150 years and quite a number of equations have been developed to make heat transfers, pressure drops and critical heat flux calculable (some research is even almost 300 years old). Due to the novelty of this work, no "ready-made model" is available to describe the heat transfer in the swirl evaporator. However, the process taking place in the evaporator can be divided into sub-processes, which are described in the literature. This chapter therefore describes the physical principles and correlations necessary to understand the thermodynamic processes in the swirl evaporator and the current state of knowledge.

2.1. The Enthalpy of Vaporization

The difference of the specific enthalpies of a saturated (boiling) liquid $h'(T)$ and a saturated vapor $h''(T)$ at the same isotherm and isobaric state.

$$\Delta h_\mathrm{v} = h''(T) - h'(T), \tag{2.1}$$

is called the specific enthalpy of vaporization . The specific energy that must be added to the boiling (saturated) liquid for complete isobaric evaporation corresponds to Δh_v. If $h = u + pv$ is inserted into 2.1, it results to

$$\Delta h_\mathrm{v} = h'' - h' = u'' - u' + p_\mathrm{s}(v'' - v'). \tag{2.2}$$

Most of the enthalpy of evaporation is due to the change in internal energy $u'' - u'$. This occurs when the relatively strong cohesion of the molecules in the liquid phase (caused by van-der-Waals forces and hydrogen bonding) are broken. After they are broken they form looser bonds in the saturated gas phase. The much smaller part of the evaporation enthalpy is the work of a volume change $p_\mathrm{s}(v'' - v')$ and this despite the large volume change $v'' - v'$ that occurs during evaporation [14].

2.2. Heat Transfer Coefficient

The heat transfer capability at the interface between a wall and a fluid is described by the heat transfer coefficient α. The heat transfer coefficient

$$\alpha = \frac{\dot{q}_\mathrm{w}}{T_\mathrm{w} - T_\mathrm{fl}} \tag{2.3}$$

can be considered as a proportionality factor between the heat flux $\dot{q}_\mathrm{w}$ transferred by the process (heat flow related to area) and the temperature difference between the heat-

transferring wall and the fluid [112, 31]. T_w is the temperature of the wall and T_fl the mean temperature of the fluid. The intensity of the heat transfer is described by the heat transfer coefficient α. In the case of boiling (saturated) liquids, the heat-transferring wall is the heating surface and the fluid, absorbing the specific enthalpy of vaporization, is used as heat-transfer medium. In the case of a phase change, heat transfer coefficients are generally much larger than in case of convective heat transfer where no evaporation or condensation takes place. Knowledge of the heat transfer coefficient is essential for calculating of heat transfer processes of all kinds. However, due to its complexity, it is not yet fully understood and has always been subject of ongoing research [14]. For flow boiling the heat transfer strongly depends on flow patterns as shown in Figure 2.1.
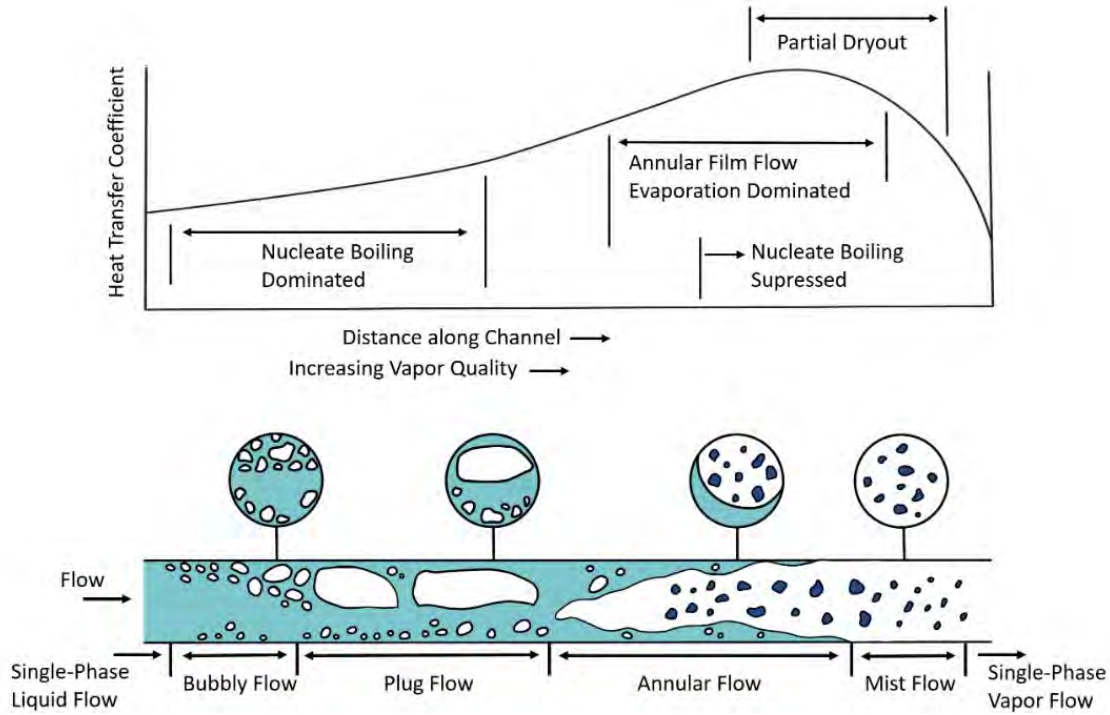
Figure 2.1.: Heat transfer mechanisms in flow boiling in a horizontal tube (acc. to [119])

2.3. Dimensionless Numbers

Dimensionless numbers are parameters in a dimensionless mathematical model of a physical state or process. If two states or processes are defined by the same mathematical model, all quantities of one can be converted into those of the other exactly when the dimensionless ratios have the same values. This means that both processes or states are similar to each other. Dimensionless key figures usually result from the de-dimensioning of a mathematical model.

2.3.1. Nusselt Number

The Nusselt number is a dimensionless number which defines the relationship between heat conduction and convective heat transfer according to the equation

$$Nu = \frac{\alpha \cdot L}{\lambda}. \tag{2.4}$$

It is often used for calculating the heat transfer coefficient α [20]. Where L the characteristic length of the considered section and λ the thermal conductivity of the fluid.

2.3.2. Prandtl Number

The material property ratio of the Prandtl number,

$$Pr = \frac{\nu}{a} = \frac{\nu \cdot \varrho \cdot c_\mathrm{p}}{\lambda} = \frac{\eta \cdot c_\mathrm{p}}{\lambda} \tag{2.5}$$

characterizes the ratio of diffusive momentum to diffusive heat transport in fluids with friction. It is a dimensionless quantity named after the scientist Ludwig Prandtl which is defined as the relationship between kinematic viscosity ν and thermal diffusivity a [20]. The density is ϱ, η the dynamic viscosity and c_p the specific heat capacity.

2.3.3. Reynolds Number

The Reynolds number is an empirically determined dimensionless number for describing the flow regime and can be interpreted as the ratio of inertial to frictional forces. Named after the Brit Osborne Reynolds, it is an indicator of which flow regime is predominant: laminar, turbulent or the transition region in between [126]. For circular pipes and one-phase flow the Reynolds number is defined as

$$Re = \frac{c \cdot d}{\nu}. \tag{2.6}$$

In pipe flows, the characteristic length would be the diameter d. For a two-phase flow, there are extended forms of the Reynolds number which will be discussed later in this thesis.

2.4. Hydraulic Diameter

The hydraulic diameter is the equivalent of a cross-section deviating from a round pipe with the same hydraulic properties, as displayed in Figure 2.2. There are two main factors that describe the flow resistance of a pipe with a flow through it. The cross-sectional area A_hyd and the length l of the tube or area in the direction of flow. The hydraulic diameter is defined as

$$d_\mathrm{hyd} = \frac{4 \cdot A_\mathrm{hyd}}{P_\mathrm{hyd}} \tag{2.7}$$

and is used to describe the resistance to flow, negated by the above geometric factors [126]. An example of the hydralulic diameter is shown in Figure 2.2. In some publications correlations with the hydraulic radius r_hyd are used. It should be noted that the hydraulic radius

$$r_\mathrm{hyd} = \frac{A_\mathrm{hyd}}{P_\mathrm{hyd}} = \frac{d_\mathrm{hyd}}{4} \tag{2.8}$$

is the result of the cross sectional area A_hyd divided by the wetted perimeter P_hyd [21].
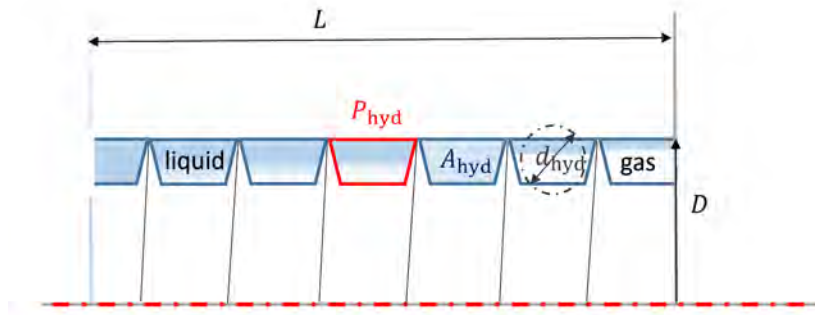
Figure 2.2.: Hydraulic diameter of a swirl evaporator [46]

2.5. Boiling Mechanism

An important parameter in boiling is the temperature difference between the wall and the fluid

$$\Delta T_{\text{wsh}} = T_{\text{w}} - T_{\text{fl}}, \tag{2.9}$$

the so-called wall superheat. It describes the temperature difference between the heating surface and the fluid. The first studies on the influence of wall superheat on the transferred heat output were carried out by the Japanese Shiro Nukiyama and published in 1934 [108]. In principle there are two different kinds of boiling mechanisms: pool boiling and flow boiling. Pool boiling is more observed in everyday live for example when water in a pot is boiling for cooking (evaporation in the interface with air). If the liquid, in this example water is heated, the evaporation starts after exceeding the saturation temperature $T_{\text{S}} = f(p)$ at $100\,°\text{C}$. At first, no phase change takes place within the fluid, but only at the phase boundary, here between the gas phase and the liquid. The heat transport in the fluid takes place due to heat conduction and convection. Since no vapor bubbles are visible, it is called silent boiling. If further energy is now introduced into the system, nucleate boiling begins. Vapor bubbles begin to form at activation points on the heating surface. After they have grown to a certain size they detach from the heating surface due to gravity (and the density difference) and rise upwards. If even more heating power is now introduced into the system, the so-called film boiling occurs. It is characterized by a continuous vapor film between the heating surface and the fluid. In everyday life, this effect only occurs when a drop of water is dropped onto a very hot stove or pan and the drop of water "dances" around on the hotplate. Since there is an insulating gas layer between the fluid and the heating surface, heat is transferred exclusively by radiation and convection in the vapor phase [53]. This phenomenon was first studied in 1756 by Johann Gottlob Leidenfrost in Duisburg, Germany, who gave the Leidenfrost effect its name [85].

In flow boiling, the kinetics of the flowing fluid play a major role. Due to the greater turbulence prevailing in the flow, relatively high heat quantities can be transferred at a relatively low temperature difference [73]. The flow patterns in a tube are illustrated in Figure 2.3.

Depending on the flow quality x, different kinds of flow patterns occur. The flow quality

$$x = \frac{\dot{m}_{\text{G}}}{\dot{m}}, \tag{2.10}$$
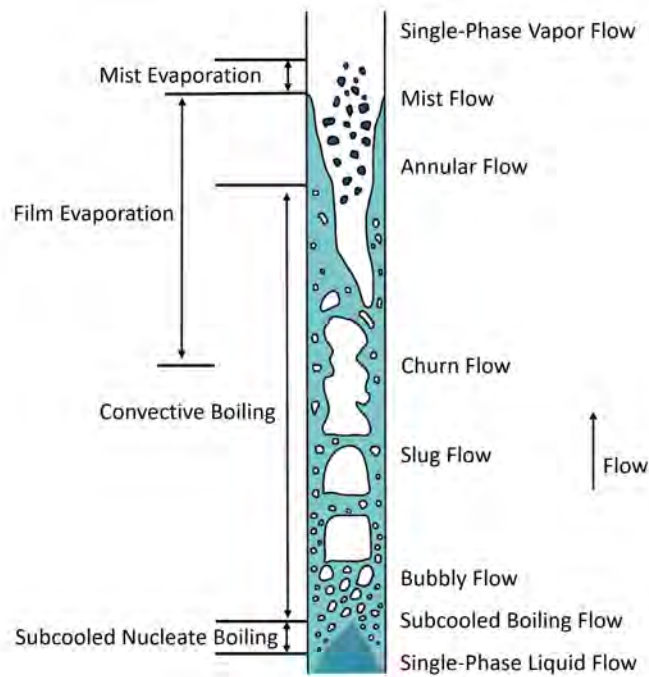
Figure 2.3.: Flow patterns and heat transfer mechanisms in a vertical tube (acc. to [26])

is defined as the proportion of the mass flow rate $\dot{m}_G$ of the gas phase and the total mass flow $\dot{m}$. Where the total mass flow

$$\dot{m} = \dot{m}_G + \dot{m}_L \tag{2.11}$$

is the sum of the gaseous mass flow and the liquid mass flow $\dot{m}_L$. In thermodynamic equilibrium the flow quality can be also calculated [67] as

$$x_{eq} = \frac{h(p) - h'(p)}{\Delta h_v(p)}. \tag{2.12}$$

2.6. Critical Heat Flux

The critical heat flux (CHF) describes the point, where the amount of heat transferred by convective boiling reaches a maximum. This means fully developed nucleate boiling without superheating on the heat exchanger wall. It's the point infinitesimally before the transition point from nucleate boiling to film boiling occurs. Figure 2.4 shows the schematic course of the Nukiyama diagram. Nukiyama studied before systems with pronounced heating surface temperature, which have a pronounced local minimum (LHF point) and maximum (CHF point). However, this course is rather academic in nature and virtually does not occur in practical applications. There, mainly systems with pronounced heat flux occur (the cooling load of a process is not reduced only because the cooling process collapses). This is measurable in a sudden increase of the wall temperature and is typically accompanied by a destruction of the heating surface.

Although Nukiyama conducted his experiments with water they are, however, also characteristic for refrigerants [128, 5, 4, 76, 93]. The critical heat flux corresponding to flow boiling depends on a number of factors:
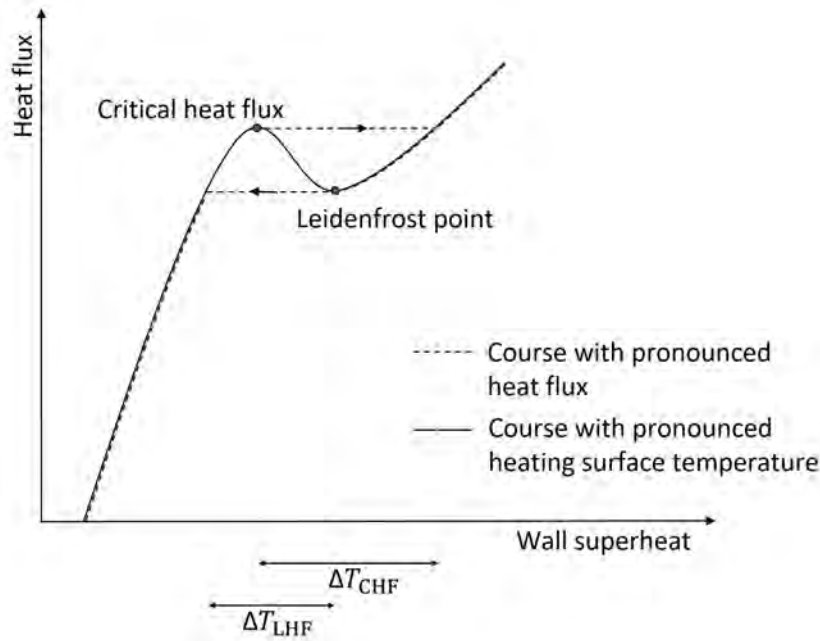
Figure 2.4.: Schematic course of the Nukiyama diagram

1. Distribution of the phases (flow pattern).

2. Flow type (laminar or turbulent, mass flux, quiescent or flowing, upward or downward inclined).

3. Surface condition of the heat transferring surface (smooth, rough, structured, material properties).

4. Type of heating (stationary/transient, homogeneous/inhomogeneous).

5. Type and thermodynamic state of the fluid (saturation temperature, material values of the fluid (e.g. enthalpy of evaporation, thermal conductivity, viscosity, etc.) composition, pressure, subcooling, void fraction).

6. Geometry of the cooling channel (hydraulic diameter, length to diameter ratio).

In the past, cooling of a high heat flux was mainly limited to power plant applications. However, advances in power electronics in recent years have created applications with power densities above those of power plants.

2.7. Void Fraction

An important factor of the two-phase flow is the so-called void fraction. With its help, various other parameters such as pressure drop, density and viscosity of the two-phase flow, heat transfer coefficient and the average velocity of the respective phase can be calculated. It is possible to define the void fraction in various ways. The ratio of the vapor volume to the total volume for a fixed channel length is called the volumetric void fraction. The fraction of the cross-sectional area of the channel occupied by the vapor phase is called the area-averaged void fraction. If the length of the vapor phase is divided by the channel length, this is called the chordal void fraction. The ratio of the time spent by the vapor

phase at a particular point to the total time is called the local void fraction. It varies along the length of the channel and is also a function of time. ε_{hom} indicates the void fraction for a homogeneous mass flow and represented by the equation

$$\varepsilon_{\text{hom}} = \frac{x_{\text{eq}}}{x_{\text{eq}} + (\varrho''/\varrho')(1 - x_{\text{eq}})}.$$

(2.13)

In this model it is assumed that the vapor velocity is corresponding to the velocity of the disperse phase. The void fraction content under the assumption of thermodynamic equilibrium x_{eq} is obtained from the enthalpy balance according to equation 2.12 [67]. The cross sectional void fraction is illustrated in Figure 2.5. Here ϱ' describes the density of the liquid and ϱ'' the density of the vapor.
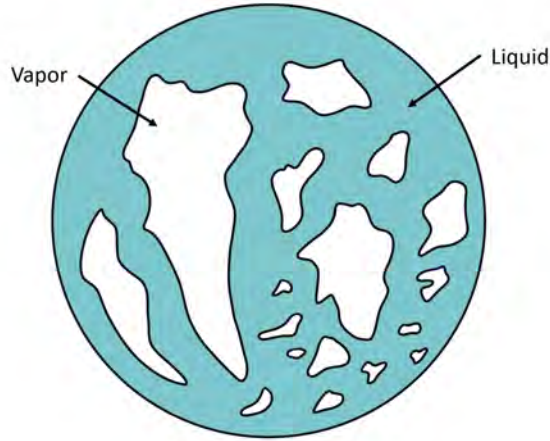
Figure 2.5.: Cross sectional void fraction (acc. to [29])

2.8. Pressure Drop in Pipe Systems

When liquids flow through pipes, exergy is converted into anergy. On the one hand, this is due to the friction that occurs between the pipe wall and the fluid (wall friction). On the other hand, friction effects also occur within the fluid due to the viscosity of the fluid (internal friction). The faster the fluid flows, the greater the internal friction [127]. Further pressure drops are caused by turbulence in the fluid. This occurs especially at valves, which can also be considered as flow obstacles. However, the kinetic energy contained in the turbulence is not transported through the pipe but is converted locally into friction [127]. The pressure drop is always related to a decrease in the total pressure (static pressure). Dynamic and hydrostatic pressures, which are determined by the geometry of the pipe, do not influence the conversion of exergy to anergy. To capture this mathematically, the initially friction-less (ideal) Bernoulli energy equation

$$p_1 + \frac{\varrho}{2} \cdot c_1^2 + \varrho \cdot g \cdot z_1 = p_2 + \frac{\varrho}{2} \cdot c_2^2 + \varrho \cdot g \cdot z_2 + \Delta p_{\text{v}},$$

(2.14)

is extended by a pressure loss term Δp_v. If this equation is converted in accordance with the pressure loss therm, the result is

$$\Delta p_v = p_1 - p_2 + \frac{\varrho}{2}\left(c_1^2 - c_2^2\right) + g \cdot \varrho\left(z_1 - z_2\right). \tag{2.15}$$

with:

- Acceleration due to gravity g in m/s^2

- Geodetic height z in m

- Pressure p in Pa

- Density ϱ in kg/m^3

- Mean flow velocity c in m/s

For both, laminar and turbulent flow, the pressure drop through a piping can be described with a dimensionless number f. This so-called pipe friction coefficient f describes the relationship between the pressure drop Δp_v and the kinetic energy contained in the flow in form of the dynamic pressure. Usually pipe systems consist of several fittings such as elbows, reducers, valves, etc. The pressure drop caused by these individual components can be described with the pressure drop coefficient ζ and is in most cases determined experimentally. The pressure drop coefficient is defined in an analogous way to the pipe friction coefficient, i.e. as the ratio between the pressure drop in the component and the dynamic pressure of the flow. For one pipe section of a length l with constant inner diameter d and constant density and therefore constant mean flow velocity c, the empirical equation

$$\Delta p_v = \frac{\varrho \cdot c^2}{2} \cdot \left(f \cdot \frac{l}{d} + \sum \zeta_i\right), \tag{2.16}$$

can be used [22]. For turbulent pipe flow, the degree of turbulence has an additional influence on the pressure drop. Furthermore, the roughness of the pipe wall has a major influence on the pipe friction coefficient. The fluid particles attach directly to the wall due to the adhesion conditions there. However, no turbulence can form in the immediate vicinity of the wall, since crossflows are prevented by the wall. For this reason, a so-called laminar boundary layer forms in the immediate vicinity of the wall.

Depending on the thickness of this laminar boundary layer and the size of the roughness, the boundary layer covers the roughness of the wall to a greater or smaller extent. Large roughness influence the flow very strongly and therefore lead to an increased turbulence. This is in turn responsible for a relatively large pressure drop. If the laminar boundary layer completely covers the surface roughness, the pipe is considered hydraulically smooth and the pressure drop is therefore lower. The roughness, which ultimately characterizes the edge region of the flow, must always be seen in relation to the entire flow cross-section, i.e. to the pipe inner diameter. The ratio of absolute roughness and pipe diameter is also referred to as relative roughness [32].

According to Schmidt [120], the calculation of the **two-phase** pressure drop differs fundamentally from the procedure for a single-phase flow. This is because the two phases

influence each other (this interaction is taken into account with void fraction). The two-phase pressure drop

$$\Delta p_{\text{total}} = \Delta p_{\text{frict}} + \Delta p_{\text{mom}} + \Delta p_{\text{static}}. \tag{2.17}$$

consists of static, momentum and frictional pressure drop [37]. Depending on the flow conditions, the distribution of the phases within a cross-section is different. Accordingly, the alternating conditions are also different, which is also influenced by the orientation. It makes a difference whether the refrigerant flows vertically or horizontally in the pipe. For **vertical flow** upwards the following flow forms occur, which are also displayed in Figure 2.6:

(A) In **bubbly flow**, the bubbles are almost homogeneously mixed with the liquid. In this case, the wall is only wetted by the liquid phase.

(B) In **plug slug flow**, very large bubbles occur in addition to smaller bubbles. The length of the bubbles is often several times the diameter of the tube.

(C) In **intermittent flow**, which is also called chaotic flow, there are small and large bubbles. The distribution seems random.

(D) In **stratified-wavy flow**, the liquid is mainly on the wall. The gas phase is inside. It mixes with droplets, which can be arranged in strands.

(E) In **annular flow**, the liquid is almost completely on the wall and the gas phase selects only a few drops of liquid.
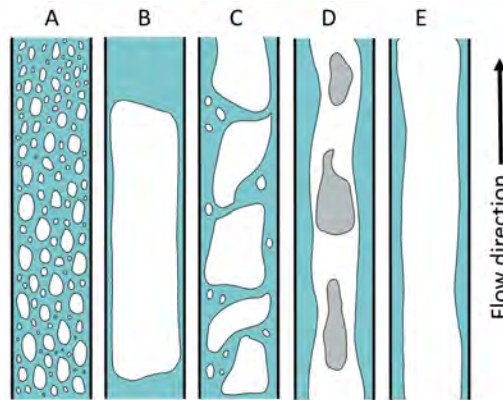
Figure 2.6.: Flow forms through a vertical pipe (acc. to [120])

In the case of **horizontal flow forms**, the following phenomena occur, which are also shown in Figure 2.7:

(a) In **bubbly flow**, small bubbles are present, which are increasingly found at the top of the tube due to gravity.

(b) In **stratified flow**, the gas flows over the liquid. No waves or the like can be seen at the phase boundary.

(c) In **wavy flow**, gas also flows over the liquid. However, in this case waves can be seen.

(d) In **slug flow**, liquid and gas are separated. The intense waves partially fill the entire cross-section. Bubbles often appear in the liquid phase. There are many liquid droplets in the gas phase.

(e) In **annular flow**, gas flows inside the tube. The wall is completely wetted. Due to gravity, most of the liquid is located in the lower part of the pipe.
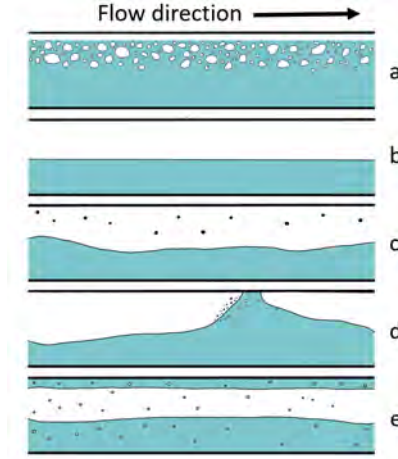
Figure 2.7.: Flow forms through a horizontal pipe (acc. to [120])

In some cases it is important to predict what type of flow will occur. In the case of surge flows, the pulses can cause damage to the fittings or pipe bends.

In practice, the type of flow can be determined from so-called flow pattern maps. For outward (vertical) flow, for example, the flow pattern map according to Hewitt and Roberts can be used [62]. For horizontal flow, the flow pattern map according to Taitel and Dukler is applicable [133]. The Lockhart-Martinelli parameter

$$X_{\text{tt}} = \frac{\dot{m}_{\text{L}}}{\dot{m}_{\text{G}}} \cdot \sqrt{\frac{\varrho_{\text{G}}}{\varrho_{\text{L}}}} \tag{2.18}$$

is often used to estimate the flow pattern [91]. The flow forms are partly discontinuous. This means that they can change in a step-like manner at one location. When modeling flow shapes, it is simplistically assumed that the form is continuous. There are different model approaches. The most common are

- the heterogeneous model,

- the homogeneous model,

- the drift-flux model and

- the two-fluid model.

Since both the drift-flux and the two-fluid model are very complex to simulate, they are only used in the context of very high-level simulation procedures [23, 92]. Therefore, the heterogeneous and homogeneous model are mostly used in practice. An essential quantity for describing gas-liquid flows is the void fraction mentioned above. For discontinuous flow (e.g. slug flow), the void fraction is averaged over a time interval. By averaging the

void fraction, this discontinuous flow can also be calculated like a continuous flow. For example, it is assumed that the flow velocity is the same for the liquid and the gas phase. A gas homogeneous model is well suited to describe two-phase flows when the phases are well mixed or differences between the phases are small. As the name suggests, the heterogeneous model is based on two phases with different properties. Here, for example, the slip ratio, i.e. the difference in flow velocities between the liquid and gaseous phases, can also be calculated. Most calculations of the two-phase friction pressure drop are based on empirical approaches. A two-phase multiplier Φ_L is often used. This was first introduced in 1948 by Matrinelli and Neslon [94]. The underlying assumption is that the two-phase pressure drop

$$\Delta p_{\text{frict}} = \Delta p_L \cdot \Phi_L^2 \tag{2.19}$$

can be calculated with either the liquid or the gaseous phase. A detailed example can be found in the appendix section A.1.

2.9. Regimes of Spot and Swirl Evaporators

In order to make comparisons and analogies, but also to see where the dissimilarities lie, the different regimes of both evaporator forms are presented here. Both evaporator designs have a cross-sectional constriction due to the fitting required to transition from the high pressure refrigerant line to the capillary tube. Both evaporator types have a relatively long capillary tube (200 mm) in which a single-phase and, depending on the material properties of the refrigerant and the geometry and surface roughness of the capillary tube, a two-phase pressure drop takes place. Characteristics for both evaporator types is the spray cooling on the front side of the blind hole as well as the deflection by 180° which is connected with a corresponding turbulence.

From here on, the flow regimes of both evaporator designs differ. In the spot evaporator shown in Figure 2.8, the flow returns in the annular gap. The pressure drop and the heat transfer coefficient in the annular gap can be calculated as normal two-phase pressure drop and heat transfer with the aid of the hydraulic diameter (the diameter of the capillary must be subtracted from the total diameter).
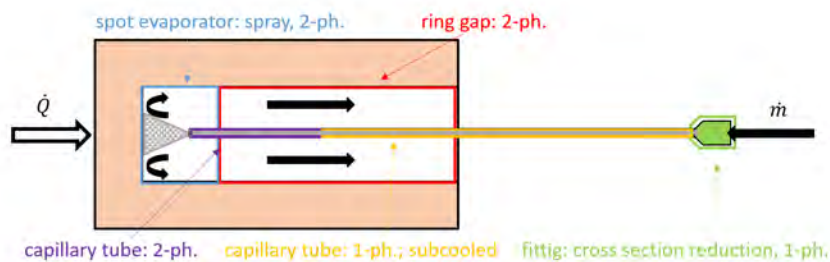
Figure 2.8.: Regimes of a spot evaporator

As the name suggests, the backflow in the swirl evaporator takes place in a swirl-generating helix geometry. Firstly it reduces the hydraulic diameter, which has a positive effect on the heat transfer coefficient, but also significantly extends the evaporator path. Therefore, the reflux path splits into two-phase pressure drop and heat transfer and, if superheating occurs, single-phase pressure drop (and heat transfer) to the end of the evaporator path.

The regimes of a swirl evaporator are shown in Figure 2.9. The regimes of the swirl
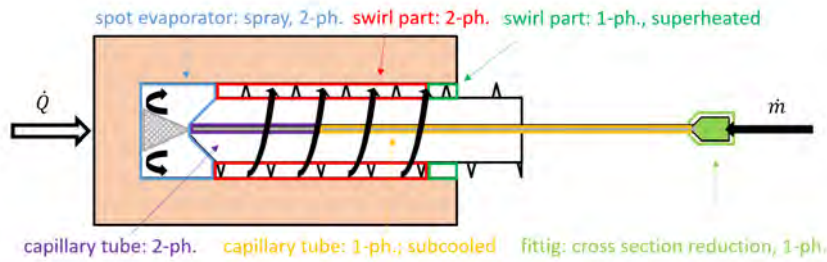
Figure 2.9.: Regimes of a swirl evaporator [46]

evaporator can be divided into regimes which are only relevant for hydraulic purposes (such as the estimation of the pressure drop) and thermally active regimes. The thermally active regimes again can be subdivided into heat transfer obtained with nucleate boiling (which is the most efficient form of boiling) and the departure from nucleate boiling (DNB) when later in the process film boiling occurs after the critical heat flux has been reached. The following list breaks down the points to be examined.

Regimes of the spot evaporator

- Hydraulically active:
    - sudden cross section narrowing
    - single-phase pressure drop in the capillary
    - two-phase pressure drop in the capillary
    - pressure drop in the spray and in the backflow
    - two-phase pressure drop in the ring gap
- Regimes involved in the heat transfer:
    - spray cooling.
    - heat transfer in the ring gap
- Regimes in which CHF might occur:
    - CHF in spray cooling
    - CHF in the ring gap

Regimes of the swirl evaporator

- Hydraulically active:
    - sudden cross section narrowing
    - single-phase pressure drop in the capillary
    - two-phase pressure drop in the capillary
    - pressure drop in the spray and in the backflow
    - two-phase pressure drop in the swirl
    - single-phase pressure drop in the swirl
- Regimes involved in the heat transfer:

- spray cooling

- heat transfer in the swirl

- Regimes in which CHF might occur:

    - CHF in spray cooling

    - CHF in the swirl area

Since the area of the lateral area exceeds the area of the face surface (depending on the length to diameter ratio) by factors, the heat transfer mechanisms of the lateral area is of great interest. What comes closest to this behavior in the literature are the so-called coiled tubes. Due to their compact structure and good thermal expansion behavior, coiled tubes (or spiral tube heat exchangers) are used in many industrial applications. In power plants, they are used as steam generators for power generation. Due to their compact structure, they are also interesting for marine and aviation applications [59]. Another similarity to the swirl evaporator is the work of Yagov [142], who put a twisted tape into a tube to improve the heat transfer.

Also involved in heat transfer in the swirl evaporator is spray cooling (however, due to the smaller heat transfer surface, it has less influence than the heat transfer in the helical part of the swirl evaporator). After the refrigerant is sprayed at the face of the bore, it is deflected by 180° in relatively limited space and exhausted against the direction of flow. This is where the swirl and spot evaporators also differ. In case of the swirl evaporator, suction takes place between 170° for a helix geometry with a high pitch and 100° for helix geometries with a low pitch, depending on the pitch of the helix geometry (screw). Since the pitch also directly influences the number of threads, most helix geometries have an inlet angle of 100° to 110° in the evaporator section of the helix geometry. The relationship between the pitch and the deflection angle is shown in Figure 2.10.
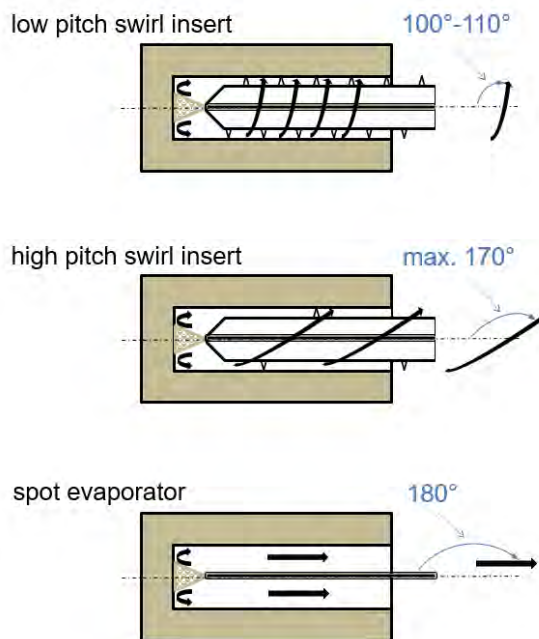
Figure 2.10.: Relationship between pitch and deflection angle of the flow

2.9.1. Spray Cooling

In spray cooling, liquid refrigerant is directed through a nozzle onto a surface to be cooled. The refrigerant hits the cooling surface as a full jet or already atomized. Due to the kinetic energy, the barrier layer can be penetrated during film boiling, enabling the high heat flux in spray cooling. The work of Katto and Kunihiro is seen as fundamental work in the field of spray cooling with low wall superheat [68]. Two experiments are compared. In the first, a heated surface is cooled by a refrigerant. In the second, this surface is cooled by a jet produced by a nozzle. Both experiments took place under atmospheric pressure. The jet could increase the CHF by 20 % when doubling the jet velocity. It was found that a larger mass flow of the refrigerant, leads to an increase of the critical heat flux.Figure 2.11 shows schematically how spray cooling works with the most important influencing variables. Heat transfer takes place at the heating surface on the basis of thermal conduction, which makes it possible to realize the high heat flux in spray cooling.
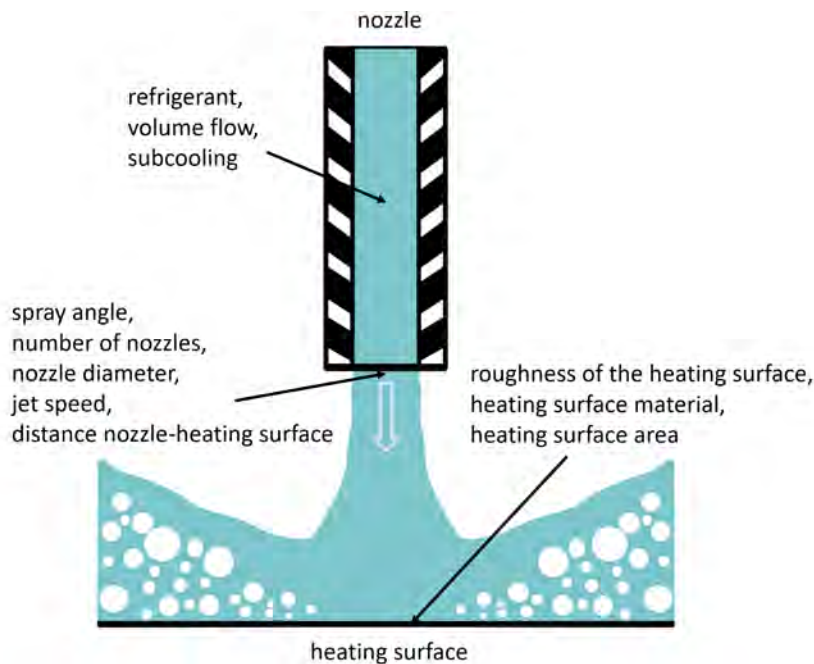
Figure 2.11.: Principle sketch of spray cooling and influencing variables (acc. to [75])

A model for calculating the critical heat flux in spray cooling is provided by Monde and Katto [97]. Water and the refrigerant R-113 were studied. For calculation, the fluid is considered as one substance. For this purpose, the proportion of the liquid and gaseous substance is averaged according to their volume fraction. In this model, the factors, mass flux, orientation of the heating surface, heating surface and internal diameter of the nozzle, type of fluid, are also considered.

Mudward and Estes [100] found out in the experiments with the refrigerant FC-72 that the type of spray has a decisive influence on the critical heat flux. There is spray cooling, where the pressure difference at the nozzle outlet causes the fluid to be atomized, and impingement jet cooling, where the fluid is atomized by the addition of a gas. In the calculations of Mudward and Estes the volume flux and the sauter diameter are included, also the subcooling is considered and not a correction factor is used. The influence of the subcooling under consideration does not contribute to an increase in the critical heat flux.

Pautsch and Shedd have found that higher turbulence of the refrigerant leads to lower effectiveness [110, 125]. Thus, impingement cooling is less effective compared to spray cooling. In addition, the critical heat flux is increased when the jet of refrigerant wets a small area of the heat exchanger. Kim et al. found that a larger spray duct, of the refrigerant, on the surfaces, leads to a larger heat transfer coefficient [3]. Thus, the heat flux is increased. The experiments were carried out with the refrigerant PF-5060. Hybrid systems can be used to increase the heat transfer coefficient. In these, spray and impingement cooling is combined with another heat transfer mechanism. Barreau et al. combined spray cooling with a mini-channel [15]. Liquid water was used for cooling, which remained in the single-phase region throughout the process. By combining both systems, a more uniform temperature distribution was obtained compared to spray cooling alone.

2.9.2. Coiled Tubes

For flows in coiled tubes or pipes, there is a pressure gradient acting perpendicular to the main flow direction generated by the centrifugal force. The centrifugal force results in secondary flow which has a significant influence on the distribution of the two phases in the pipe helix, which characterize the local heat transfer, as shown in Figure 2.12. The liquid has a higher density compared to the gas, therefore it is assumed that the liquid is pressed against the outer wall [60]. The secondary flow exerts a shear stress on the inner surface of the liquid film. This causes the liquid flow to move from 270° to 90°, improving the rewetting of the surface. Young and Bell [144] found out that the liquid film disappeared first at the top of the coil 0° and then at the bottom of the 180° when measuring the local heat transfer coefficient along the length and circumference of the coil.
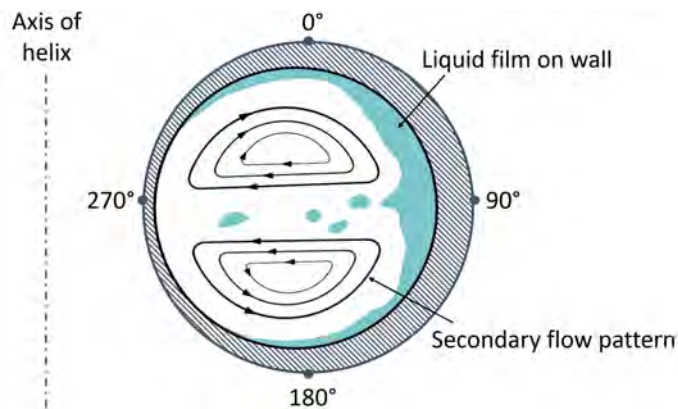
Figure 2.12.: Secondary flow in a coiled tube (acc. to [144])

The position of the liquid film varies depending on the mass flux and operating pressure. In Figure 2.13, the positions of the liquid film are clarified. At a mass flux $G > 850\,\mathrm{kg/(m^2\,s)}$ the centrifugal force prevails, pushing the liquid against the outer wall. If the mass flux drops below $850\,\mathrm{kg/(m^2\,s)}$, gravity prevails and the liquid film forms at the bottom of the pipe helix. Ishida [65] finds that when the gas content is large, the liquid migrates to the inner wall of the pipe helix. This phenomenon is called "film inversion" and it occurs at high gas but low liquid flow rates. If the liquid fraction continues to decrease, the film migrates upward until the liquid layer breaks off and is thrown to the outer wall of the pipe helix. Film movement of the liquid at various gas mass flow rates shown in Figure 2.13

corresponds with the following items:

a) With upward, helical flow and low gas flow rates, the liquid film was mainly located on the outer wall of the tube

b) The liquid film moves to the neutral position as the gas velocity increases.

c) As the gas velocity continues to increase, the liquid film moves into the inverted position.

d) As the gas velocity increases, the film continues to move up the inner wall of the tube.

e) At higher velocities, the liquid was carried away from the film and flung onto the outer part of the wall.
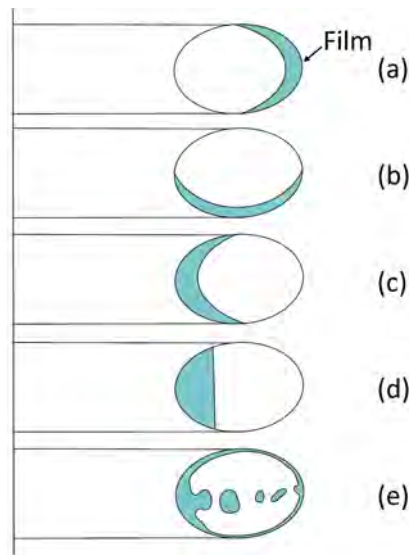
Figure 2.13.: Film movement of the liquid at various vapor mass flow rates (acc. to [65])

Smaller pipe diameters of $d = 4\,\mathrm{mm}$ were tested by Yi et al. [143]. Pure liquid flow, surge flow, and unsteady stratified flow were found, as shown in Figure 2.14. A ring flow did not occur due to the small flow velocities.
Hardik investigates in his work the pressure drop in small diameter coiled tubes and comes to the conclusion that the curvature effect is fully included in the correlation for single phase pressure drop [59]. In a later work he investigates the distribution of heat transfer in the pipe coil. This is realized with temperature measurement around the pipe helix. The diameters of the tubes are chosen between $5\,\mathrm{mm}$ and $10\,\mathrm{mm}$. It was found that with larger radius, the inner heat transfer coefficient increases, while the outer one decreases more and more. Overall, the average heat transfer coefficient remains the same compared to a straight tube [58].
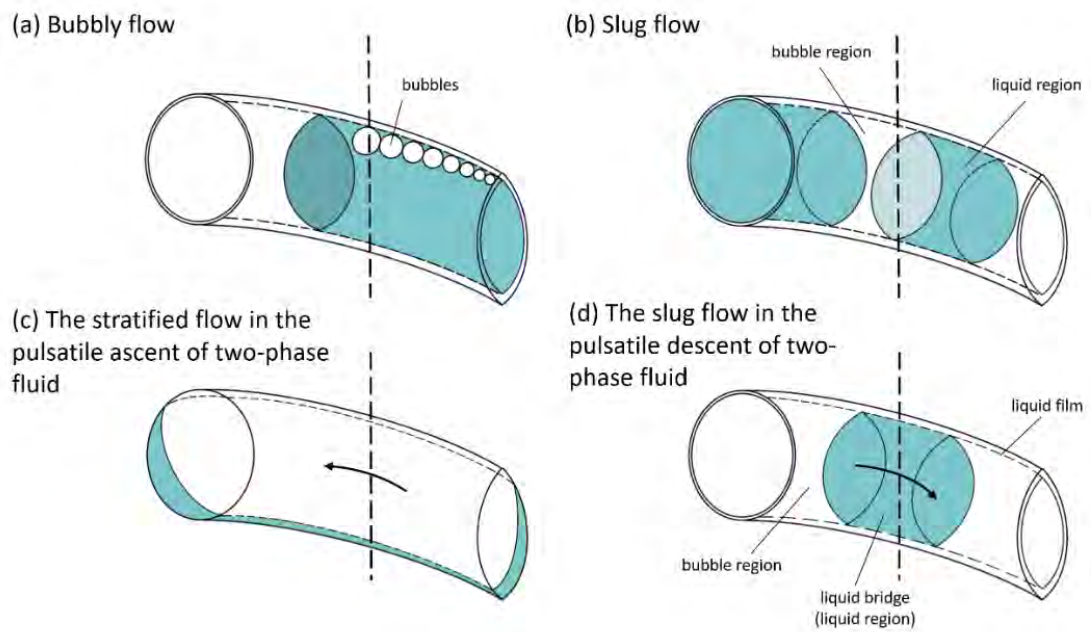
Figure 2.14.: Two-phase flow patterns in coiled tubes (acc. to [143])

3. Development of the Swirl Evaporator Model

This chapter presents the calculation models and correlations used to simulate the thermodynamic processes within the swirl evaporator. Due to the novelty of the swirl evaporator, there is currently no model in the literature that can be used for comparison. Therefore, several correlations are proposed that could theoretically be used. The simulation model is based on theoretical, empirical and semi-empirical equations proposed in literature to calculate single and two-phase pressure drops, heat transfer coefficients and CHF for different geometries. The input variables should be easily measurable quantities, such as the geometric parameters, evaporating and condensing pressure, temperature of the refrigerant before entering the capillary tube, temperature after the refrigerant leaves the swirl evaporator and its subcooling.

Before going into more detail about how the swirl evaporator model works, the processes that occur in the evaporator are explained using the pressure enthalpy diagram illustrated in Figure 3.1. The corresponding steps in the cycle process are shown in Table 3.1 and the regimes are already described in Chapter 2 (Figure 2.9). The refrigerant mass flow $\dot{m}$ enters the capillary through a fitting, which causes a pressure drop due to the sudden cross section reduction. After that, the refrigerant flows through the capillary tube, which causes a pressure drop because of the frictional losses. Depending on the pressure drop in the capillary tube a two-phase condition may occur. This is mainly a function of hydraulic diameter, length and flow velocity. After that the refrigerant is sprayed against the hot end face of the blind hole, where it partly evaporates and is deflected by 180° in the process. Depending on the insertion depth of the swirl generating geometry, the refrigerant is first passed through a small section of "spot evaporator" or "pre-swirl" before entering the helical geometry. The process steps that take place in the swirl evaporator itself are shown in the bold line in Figure 3.1. The process steps outside the swirl evaporator, which do not differ from an ordinary refrigeration cycle, are illustrated with the thin black line.
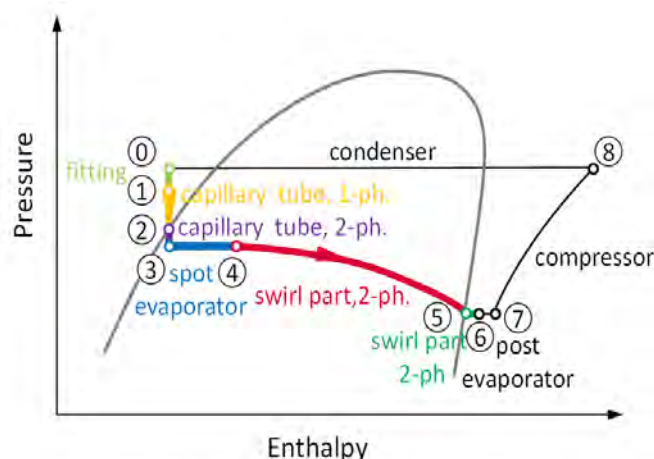
Figure 3.1.: Cycle process in the swirl evaporator in the pressure-enthalpy diagram [46]

Table 3.1.: Steps in the cycle process

Step	Process
0→1	refrigerant flows through the fitting into the capillary tube sudden cross-section narrowing from 6 mm to 0.5 mm
1→2	single phase pressure loss in the capillary tube
2→3	two-phase pressure drop in the capillary tube
3→4	at the capillary outlet, the refrigerant expands as a spray channel onto the end face of the pocket hole
4→5	the refrigerant counterflow enters the helical geometry against the inflow direction and continues to evaporate This area is also called the swirl part of the evaporator
5→6	if the heat input is above the latent heat the refrigerant will already overheat in this area
6→7	for compressor safety there is also an additional post evaporator in the test bench to assure a fixed overheating of the refrigerant
7→8	the refrigerant is compressed to condensation pressure
8→0	the refrigerant condensates in the condenser and gets subcooled in an additional heat exchanger

In the swirl evaporator test carrier, the heat load is transferred into the system with the use of an electric heater tape via the outer surface of the cylinder. The test carrier housing, which is displayed in Figure 3.2, is made out of copper which has a relatively high thermal conductivity of around $380\,\mathrm{W/(m^2\,K)}$ [2] and distributes the heat along the heat transferring surface. The heat is dissipated in the blind hole by the evaporation of the refrigerant.

To model the swirl evaporator, 3 different physical principles must be considered:

- pressure drop

- heat transfer

- critical heat flux

Knowledge of the pressure drop Δp is essential, as it allows calculation of the mass flow $\dot{m}$. The mass flow influences the Nusselt number Nu which influences the heat transfer coefficient. Knowledge of the heat transfer coefficient α is important because it can be used to infer the cooling capacity of the evaporator. Understanding the CHF $\dot{q}_{\mathrm{crit.}}$ is important because it limits the evaporator capacity upwards.

Basically, there are 3 different models which would work on their own, but which can also interact with each other. In order to determine the two-phase pressure loss in the pressure loss model, however, it is important to know not only the geometry and roughness, but also the change in vapor quality (or the power introduced into the swirl evaporator) in order to be able to calculate the pressure loss.

To determine the pressure drop, various pressure drop models from the literature are simply evaluated and "connected in series" to calculate the pressure drop with the experimentally determined mass flow. However, the model also works "the other way around".

Since in refrigeration systems in industry, pressures can be measured very easily but mass flows only with an increased effort. Therefore, a algorithm was programmed to determine the mass flow based on the pressure loss. This is an iterative procedure in which from an estimated starting value of the mass flow, the mass flow is increased or decreased incrementally in the numerical simulation. This is repeated until the calculated pressure loss matches with the measured. However, it should be mentioned at this point that either the pressure loss **or** the mass flow must be known in order to apply this model.

To connect the individual models already mentioned "in series", the swirl evaporator must first be divided into different assemblies. These assemblies are then further subdivided into sectors, or more precisely, into fluidic regimes in order to be able to calculate the thermodynamic processes. For calculating the processes in the individual regimes, suitable models from the literature are used. To get a better idea of the system and to get an idea for the geometry and dimensions, the profile of the swirl evaporator is shown in Figure 3.2.
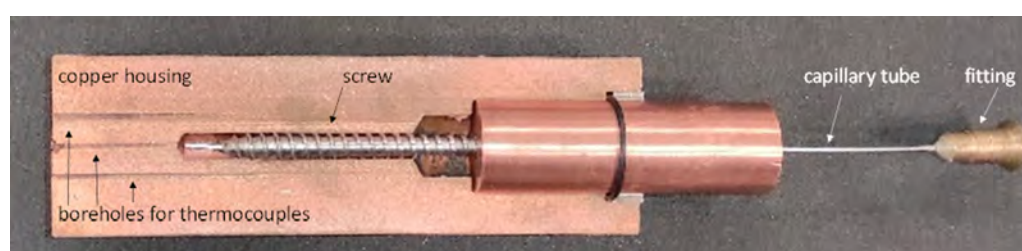
Figure 3.2.: Profile of a swirl evaporator with hydraulically relevant parts [46]

3.1. Refrigerant

All calculations and investigations in this work have been carried out with the refrigerant R-32. It meets all relevant criteria to be used in an industrial environment in a swirl evaporator. Since it is used in many applications (e.g. air conditioning) and it is the replacement refrigerant of R-410A, low investment costs are needed to set up a refrigeration system for R-32. Due to its wide distribution, it has also a good availability in the market. Furthermore, all relevant parameters for the choice of a refrigerant for a swirl evaporator are fulfilled [66]:

- The vapor pressure remains below $20-30$ bar even in critical situations.

- Evaporating temperature at atmospheric pressure is $-51.7\,°C$ and the specific enthalpy of evaporation is $280.8\,kJ/kg$.

- Toxicity and flammability are in class A2L [38]. This means:
    - The flame spread velocity is less than $10\,cm/s$,
    - an explosion limit of $100\,g/m^3$
    - and a combustion enthalpy of $<19\,MJ/kg$.
    - The workplace guideline limit is $\geq 400\,ml/m^3$.
    - In the application case, this means that a filling quantity of the total system of $11.4\,kg$ of refrigerant must not be exceeded, but this can be achieved in practice without any problems.

- Environmental compatibility is within acceptable limits.
    - Global Warming Potential (GWP) is 675 [41] and the
    - Ozone Depletion Potential (ODP) is zero [41].

All substance data were determined using the software Engineering Equation Solvers (EES). This means

- This means the thermodynamic properties of R-32 are described using the equations of state by Tillner-Roth and Yokozeki [134].

- The correlation applies to temperatures from the triple point at $136.34\,\mathrm{K}$ to $435\,\mathrm{K}$ and pressures up to $70\,\mathrm{MPa}$.

- The liquid phase viscosity and conductivity data are from the general correlation described by Assael et al. [12].

- The property correlation is applicable over the same range as the equation of state.

- The surface tension is determined using the correlation of Mulero et al. [101].

3.2. Fitting/Cross-Section Constriction Model

The first hydraulically active regime is the model for the pressure loss caused by the fitting. The fitting connects the capillary with the rest of refrigeration cycle. A cross-section constriction model is used to calculate the pressure loss. Since there is no heat input here, it is assumed to be adiabatic. To describe the thermodynamic change of state, a simple single-pass pressure drop model is sufficient. A picture of the fitting and the capillary tube is shown in Figure 3.3.
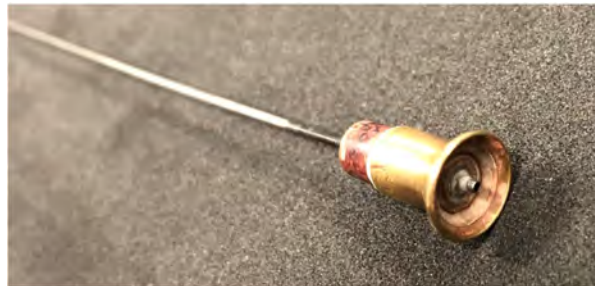
Figure 3.3.: Picture of the fitting and capillary tube
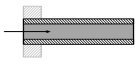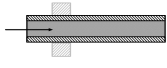
Pressure Loss in the Cross-Section Constriction

The sudden cross-section constriction caused by the fitting can be calculated with the Borda-Carnot equation [106]

$$\Delta p = \zeta_{\mathrm{E}} \cdot \frac{\varrho}{2} \cdot c^2, \tag{3.1}$$

which is a derivation from the Bernoulli equation. The pressure loss coefficients ζ_{E} for the respective inlets can be found, for example, in the corresponding chapter of the VDI Heat

Table 3.2.: Pressure loss coefficients for the outlet from vessels with quiescent fluids

edged inlet	very sharp	$\zeta_\mathrm{E} = 1.69$	
	normal broken	$\zeta_\mathrm{E} = 0.5$	
far ahead edged inlet	very sharp (Borda Estuary)	$\zeta_\mathrm{E} = 3$	
rounded inlet	depending on smoothness	$\zeta_\mathrm{E} = 0.005$ to 0.06	
	normal	$\zeta_\mathrm{E} = 0.05$	
rounded inlet under angle δ normal broken	$\zeta_\mathrm{E} = 0.5 + 0.3 \cdot \cos(\delta) + 0.2 \cdot \cos^2(\delta)$		

Atlas [106] or other relevant literature [21] as shown in Table 3.2. Since the capillary tube protrudes into the high-pressure side tube area, a Borda Estuary is assumed here.

In the original application form, these equations are used to calculate pressure losses from vessels containing liquids at rest into various inlets of pipes as displayed in Table 3.2. However, this simplification seems appropriate since the diameter of the inlet pipe and the capillary tube differs by a factor of 12. Furthermore, the assumption is made that the pressure loss is isenthalp. In this way, step "0→1" from Figure 3.1 resp. Table 3.1 can be calculated.

3.3. Capillary Model

The second hydraulically active regime that directly follows the fitting respectively cross-section constriction is the capillary. Since there is no heat input or output from the capillary, this model can also be assumed to be adiabatic.

Pressure Loss in the Capillary Tube

Depending on the flow velocity and the subcooling of the refrigerant, a single-phase and two-phase pressure loss could occur in the capillary tube due to the frictional pressure losses. Because of this phenomenon the capillary tube (which is a throttling element) must be divided into two subareas: A single-phase and a two-phase pressure drop

$$\Delta p_\mathrm{cap} = \Delta p_\mathrm{cap;\,1ph} + \Delta p_\mathrm{cap;\,2ph}. \tag{3.2}$$

If the latter is the case, the correlation for the calculation of the pressure drop must be changed, hence the single-phase pressure drop correlation is no longer sufficient to describe the pressure loss. Since the capillary is a throttling element, it is assumed that an isentalpic expansion takes place. Thus, the enthalpy can be used to determine the corresponding saturated vapor pressure. If the enthalpy falls below the saturated vapor pressure, the correlation is changed to the two-phase correlation. The transition point is calculated by the moving boundary model and is a result of the thermodynamic conditions. Thus, for each calculation, the respective distance of the single-phase and the two-phase pressure

loss is calculated. An illustration of the capillary-model with the variable transition point from single-phase to two-phase is shown in Figure 3.4.
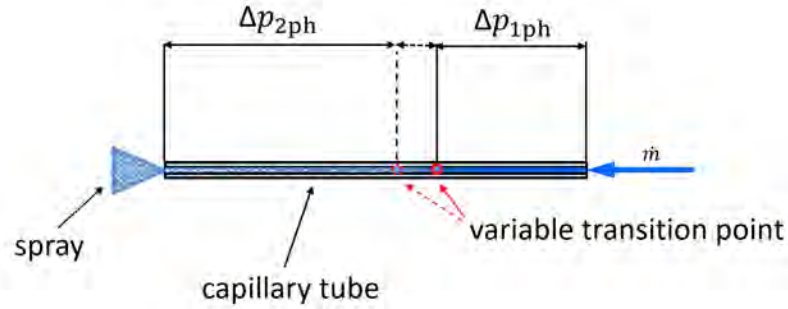
Figure 3.4.: Capillary model with variable transition point

To determine the exact length of the capillary tube at which the flow becomes two-phase, the capillary must be divided into n small length increments as shown in Figure 3.5. Here, the individual pressure losses of the segments from $i = 0$ to $i = x$ are added up until the saturated steam pressure is reached, the remaining capillary tube is then further calculated with a two-phase correlation and has $n - x$ increments.
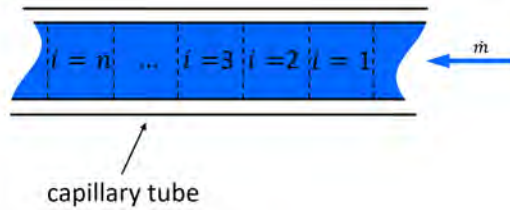
Figure 3.5.: Capillary model segmentation

To recap: The capillary tube pressure loss model consists of a single-phase and a two-phase submodel or subregime. The length of each regime is defined by the variable transition point of the moving boundary model and depends on the frictional pressure loss in the capillary tube and the thermodynamic input variables of the refrigerant.

Single-Phase Correlation Capillary Tube

In order to find out the appropriate correlation, it must first be clarified whether the pipe is hydraulically smooth or hydraulically rough as proposed in [21]. The roughness coefficient of the capillary was assumed to be $k = 0.0015\,\text{mm}$ for drawn stainless steel and the inner diameter of the tube is $d_\text{cap} = 0.5\,\text{mm}$. According to Colebrook [32], pipes can be divided into hydraulically smooth, rough, or a transition area between smooth and rough. The following criterion

$$65 < Re \cdot \frac{k}{d_\text{cap}} < 1300 \tag{3.3}$$

helps to determine this. If the calculated value is below 65, the pipe is hydraulically smooth, if it is between 65 and 1300, the pipe is in a transition zone and if the value is above 1300, the pipe is hydraulically rough. The individual correlations are listed below [21, 32].

Hydraulically Smooth Pipes

Depending on the degree of turbulence, which is defined by the Reynolds number, two different equations can be used to calculate the pressure loss coefficient ζ_{E}. For the range $2320 < Re < 10^5$, the equation of Blasius [19],

$$\zeta_{\mathrm{E}} = 0.3164 \cdot Re^{-0.25} = \left(\sqrt[4]{100 \cdot Re} \right)^{-1} \tag{3.4}$$

is used. For the range $10^5 < Re < 5 \cdot 10^6$,

$$\zeta_{\mathrm{E}} = 0.0032 + 0.221 \cdot Re^{-0.217} \tag{3.5}$$

is applied.

Hydraulic Transition Area

If the value obtained from Equation 3.3 is between 65 and 1300, the pipe is in a transition zone that can be calculated with the equation of Altschoul [21, p. 163],

$$\frac{1}{\sqrt{\zeta_{\mathrm{E}}}} = 1.8 \cdot \lg \left(\frac{Re}{Re \cdot \left(\frac{k}{10 \cdot d_{\mathrm{cap}}} \right) + 7} \right) . \tag{3.6}$$

Hydraulically Rough Pipes

And if the value from Equation 3.3 is above 1300 the pipe is hydraulically rough, which an be calculated with the equation of Moody [98],

$$\zeta_{\mathrm{E}} = 0.0055 + 0.15 \cdot \left(\frac{k}{d_{\mathrm{cap}}} \right)^{1/3} . \tag{3.7}$$

In case there is only a single-phase pressure loss, it can be calculated via Equation 3.8,

$$\Delta p = \zeta_{\mathrm{E}} \cdot \frac{l}{d_{\mathrm{cap}}} \cdot \frac{\varrho}{2} \cdot c^2 . \tag{3.8}$$

with the capillary length of $l_{\mathrm{cap}} = 220\,\mathrm{mm}$. In case of phase change in the capillary, the total length of the capillary is divided into, for example, n segments. The pressure loss for the length

$$\Delta l = \frac{l_{\mathrm{cap}}}{n} \tag{3.9}$$

is determined cyclically and it is queried whether the operating pressure has fallen below the saturation vapor pressure and whether the two-phase area has been reached. At this moment the length of the single-phase area and the pressure drop in it is known and can be considered in the single-phase and also the two-phase pressure loss correlation.

Two-Phase Correlation Capillary Tube

Since a gas and liquid phase occur in a two-phase flow, the viscosity cannot be determined exactly, a viscosity model must be used in this case. In regimes with two-phase refrigerant

state, gaseous and liquid phase are described together in one model, ergo defined with the same flow velocity. For the simulation, a viscosity model according to Akers [7],

$$\nu_{2\text{ph}} = \frac{\nu_{\text{L}}}{1 - x + x \cdot \left(\frac{\varrho_{\text{L}}}{\varrho_{\text{G}}}\right)^{0.5}} \tag{3.10}$$

is used. The viscosity is calculated for the two-phase state with the vapor content x and the density for liquid and gas phase. The viscosity model is also used to calculate material properties such as thermal conductivity, thermal diffusivity and surface tension.

For the pressure loss in a two-phase flow in a pipe with unknown flow form, the correlation of Garcia et al. [52],

$$\Delta p_{2\text{ph}} = \frac{\Delta l \cdot 2 \varrho_{\text{M}} c_{\text{M}}^2}{D} \cdot \left(0.0925 \cdot Re^{-0.2534} + \frac{13.98 \cdot Re^{-0.9501} - 0.0925 \cdot Re^{-0.2534}}{\left(1 + \left(\frac{Re}{293}\right)^{4.864}\right)^{0.1972}}\right) \tag{3.11}$$

can be used. Since this is a two-phase flow an average velocity c_{M} and an average mixture density ϱ_{M} are given. The mean flow velocity c_{M}

$$c_{\text{M}} = \frac{c_{\text{L}} + c_{\text{G}}}{2}, \tag{3.12}$$

is the sum of the empty pipe gas velocity c_{G} and empty pipe liquid velocity c_{L},

$$c_{\text{L}} = \frac{\dot{V}_{\text{L}}}{A} = \frac{\dot{m} \cdot (1 - x)}{\varrho_{\text{L}} \cdot A} \tag{3.13}$$

with

$$c_{\text{G}} = \frac{\dot{V}_{\text{G}}}{A} = \frac{\dot{m} \cdot x}{\varrho_{\text{G}} \cdot A}. \tag{3.14}$$

The mixture density ϱ_{M}

$$\varrho_{\text{M}} = \varrho_{\text{L}} \cdot \Lambda_{\text{L}} + \varrho_{\text{G}} \cdot (1 - \Lambda_{\text{L}}) \tag{3.15}$$

is defined as in Equation 3.15 with

$$\Lambda_{\text{L}} = \frac{\dot{V}_{\text{L}}}{\dot{V}_{\text{L}} + \dot{V}_{\text{G}}}. \tag{3.16}$$

Due to the dominant share of the liquid phase in the total pressure drop, the average Reynolds number,

$$Re = \frac{c_{\text{M}} \cdot d \cdot \varrho_{\text{L}}}{\eta_{\text{L}}} \tag{3.17}$$

is calculated exclusively with the viscosity for the liquid phase. To simplify the overview, the variables are listed here.

c_M	m/s	Mean flow velocity
ϱ_L	kg/m^3	Density of the liquid phase
ϱ_G	kg/m^3	Density of the gaseous phase
ϱ_M	kg/m^3	Mixture density
Λ_L	–	Volume flow portion liquid phase
Δl	m	Length of the pipe relevant for pressure loss
D	m	Pipe Diameter
Re	–	Reynolds number
$\dot{V}_\mathrm{L}$	m^3/s	Liquid volume flow of the stream
$\dot{V}_\mathrm{G}$	m^3/s	Gas volume flow of the stream

3.4. Spray Model

After leaving the capillary tube, the refrigerant is sprayed onto the evaporator wall by a sudden expansion of the cross-section. Since the refrigerant is sprayed onto a heat transfer surface and is also deflected against inflow direction, pressure drop and heat transfer must be considered in the spray model.

3.4.1. Pressure Loss in the Spray

The spraying against the hot wall and the deflection of 180° with a sudden expansion of the geometrical cross-section but also the refrigerant itself (because of the phase change) results in pressure changes. Since this can be a two-phase flow, a correlation must be used which takes this into account. Figure 3.6 shows the schematic structure in the spray.
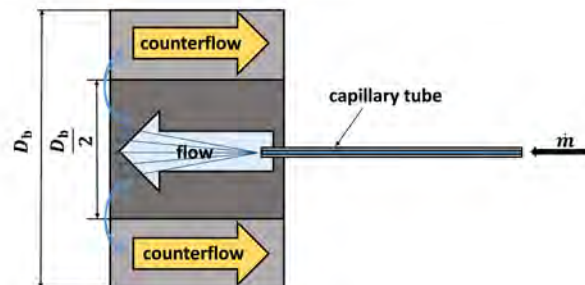
Figure 3.6.: Illustration of spray from the capillary tube with a sudden change in cross section [46]

Here a jet flows at a 90° angle from the capillary tube against the evaporator wall. On the outside of the evaporator there is a counter-flow which is exhausted via the swirl. For the estimation of the pressure drop in the spray area the assumption is made that flow and counter-flow of the spray are in each case related to half of the evaporator diameter $D_\mathrm{b} = 4.5\,\mathrm{mm}$ [28]. This takes into account the two-phase flow as well as the occurring counter-flow. The model considers a two-phase state during spraying from the capillary and the influence of the counter-flow. It assumes an expansion due to a sudden change in cross-section up to half the bore diameter. As shown in Figure 3.6 In the other half of the bore diameter, the reverse flow takes place in the model. The two-phase pressure drop of the occurring flow in the spray is completely defined when the single-phase pressure drop

and the two-phase pressure drop factor γ_{spray} are calculated. The two-phase pressure drop $\Delta p_{\text{2ph, spray}}$ consists of the product

$$\Delta p_{\text{2ph, spray}} = \Delta p_0 \cdot \gamma_{\text{spray}}. \tag{3.18}$$

Were γ_{spray} is the two-phase component that factor is calculated according to

$$\gamma_{\text{spray}} = 1 + \left(\left(\frac{\nu_{\text{G}}}{\nu_{\text{L}}} - 1 \right) \cdot (B \cdot x \cdot (1 - x) + x^2) \right). \tag{3.19}$$

Were x is the vapor content at the capillary tube outlet and $\nu_{\text{G}}/\nu_{\text{L}}$ the ratio of the gas and liquid viscosities. A distinction is made, depending on the ratio of the vapor content and the specific volume.

The coefficient for the two-phase flow is determined as

$$B = \left(\frac{1}{k_{\text{slip}}} \right)^{0.28}. \tag{3.20}$$

Depending on the ratio of vapor fraction to the specific volume, different calculation methods must be used to calculate the velocity ratio k_{slip}.

For $X_{\text{xp}} > 1$ holds

$$k_{\text{slip}} = \left(\frac{\nu_{\text{G}}}{\nu_{\text{L}}} \right)^{0.25} \tag{3.21}$$

and for $X_{\text{xp}} \leq 1$

$$k_{\text{slip}} = 1 + x \cdot \left(\frac{\nu_{\text{G}}}{\nu_{\text{L}}} - 1 \right)^{0.5}. \tag{3.22}$$

X_{xp} is calculated according to the equation

$$X_{\text{xp}} = \frac{1 - x}{x} \cdot \left(\frac{\nu_{\text{L}}}{\nu_{\text{G}}} \right)^{0.5}. \tag{3.23}$$

The equation for determining Δp_0 applies to the single-phase pressure drop,

$$\Delta p_0 = \frac{\xi_{\text{spray}} \cdot G^2 \cdot \nu_{\text{L}}}{2} \tag{3.24}$$

with

$$\xi_{\text{spray}} = \left(\frac{-2}{\sigma_{\text{ar}}} \right) \cdot \left(1 - \left(\frac{1}{\sigma_{\text{ar}}} \right) \right) \tag{3.25}$$

and

$$\sigma_{\text{ar}} = \frac{1}{4} \cdot \frac{D_{\text{b}}^2}{d_{\text{cap}}^2}. \tag{3.26}$$

3.4.2. Heat transferred by the Spray

The Nusselt correlation which is used to calculate the heat transfer through the spray is from Lindemann et al. [89]. The Lindemann correlation is a modification of the Goldstein correlation [114], which is for the fluid air in its original form. By modification, the correlation is also applicable to other unspecified fluids. This correlation describes the heat transfer of jets at a certain angle onto a wall, this is shown in Figure 3.7.
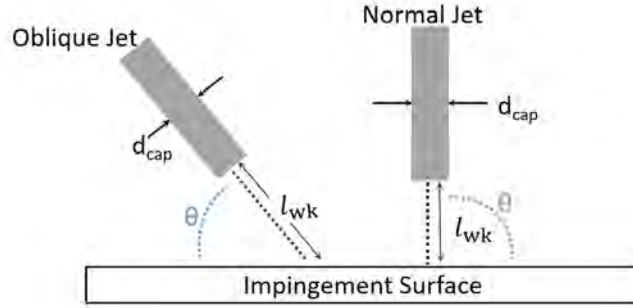
Figure 3.7.: Injection angle to the cooling surface

The variables have the following meaning:

l_{wk}	Distance between capillary outlet and the cooling wall (end face of the blind hole)
Θ	Injection angle in dregrees
Pr	Prandtl number
m	Factor experimentally determined to 0.75 after [89]

If a two-phase flow is present, the required material data are calculated with the viscosity model for two-phase fluids. The result is a correlation for the Nusselt number,

$$Nu_{\text{spray}} = Re_{\text{cap}}^{0.7} \cdot Pr^{1/3} \cdot A \cdot e^{-(B+C \cdot cos(\Phi)) \cdot \left(\frac{l_{\text{wk}}}{d_{\text{cap}}}\right)^m}. \tag{3.27}$$

To calculate the Nusselt number, the Prandtl number, the factors

$$A = -1.45 \cdot 10^{-4} \cdot \left(\frac{l_{\text{wk}}}{d_{\text{cap}}}\right) + 0.151, \tag{3.28}$$

$$B = 0.18 \cdot \Theta^2 - 0.54 \cdot \Theta + 0.78, \tag{3.29}$$

$$C = 0.16 \cdot \Theta^2 - 0.67 \cdot \Theta + 0.66 \tag{3.30}$$

and the Reynolds number must first be determined. Since a single-phase liquid state is implied for the correlation, the material properties are determined according to the previously described viscosity model. From the Nusselt number calculated above, the

heat transfer coefficient can be determined via

$$Nu_{\text{spray}} = \frac{\alpha_{\text{spray}} \cdot d_{\text{cap}}}{\lambda_{\text{spray}}} \implies \alpha_{\text{spray}} = \frac{Nu_{\text{spray}} \cdot \lambda_{\text{spray}}}{d_{\text{cap}}}. \tag{3.31}$$

3.5. Swirl Model

After the refrigerant is sprayed onto the hot evaporator wall front surface and is deflected 180° it enters the swirl area. In the swirl area, the refrigerant evaporates in the helical evaporator section which can be e.g. a screw or a 3D printed insert. Due to the helical flow guidance, the refrigerant is pressed against the lateral surface of the bore and the evaporator distance is extended by factors. Since the lateral surface of the borehole has the largest share of the heat-transferring surface, the greatest potential lies in the subsequent optimization of this section. All three aspects,

- pressure drop
- heat transfer
- critical heat flux

must be considered in the swirl model.

3.5.1. Pressure Loss in the Swirl

In the regimes with phase change, such as in the capillary and swirl range, a different location for the phase change occurs depending on the operating parameters. The size of an individual phase area must be determined accordingly in the simulation by discretising the regimes concerned.

According to Hardik [59] the two-phase pressure drop in a helical coil can be calculated with the stretched length of the evaporator section hence "the influence of a helical coil is completely included in the single phase pressure drop correlation for helical coils" [59].
So the pressure drop in the swirl can be described with acceptable accuracy by a two-phase pipe flow correlation. For this purpose, the length of the tube must correspond to the unrolled or stretched swirl length. For a better understanding of the geometrical relations they are illustrated in Figure 3.8.
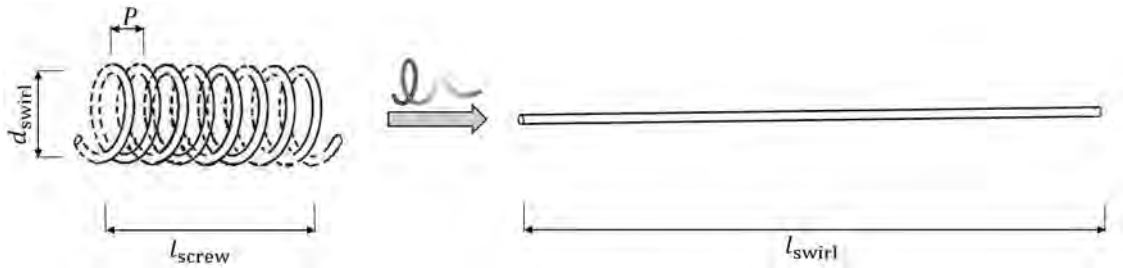
Figure 3.8.: Stretched length of the swirl (mod. from [51] and [49])

The mean helical diameter d_{swirl} corresponds to the effective pitch diameter of a screw. The stretched length of the swirl l_{swirl} can be calculated with

$$l_{\text{swirl}} = ((\pi \cdot d_{\text{swirl}} \cdot n)^2 + l_{\text{screw}}^2)^{0.5} + 2 \cdot d_{\text{swirl}} \cdot \pi \tag{3.32}$$

which can be derived from the theorem of Phytagoras [107]. The number of windings n is calculated as

$$n = \frac{l_{\text{screw}}}{P}. \tag{3.33}$$

To calculate the two-phase pressure drop the method of Didi [37] is used. For the correlation an input vapor content and an output vapor content are required. These are calculated from the heat flow to be dissipated. The input vapor content results from the previous pressure changes as well as the heat input into the spray which, correspond to approximately 7 % of the total heat flux and around 13 % in the pre-swirl area. So the inlet vapor content of the swir is approximately 20 %. For the initial vapor pressure in this work, the simplification was made that the vapor content in the swirl changes only with the heat input and not with the pressure drop. Since the latter has a significantly smaller effect on the vapor content compared to an enthalpy change.

The pressure drop is calculated from the sum of momentum pressure drop Δp_{mom}, friction pressure drop Δp_{frict} and static pressure drop,

$$\Delta p_{\text{total}} = \overbrace{\Delta p_{\text{static}}}^{=0} + \Delta p_{\text{mom}} + \Delta p_{\text{frict}}. \tag{3.34}$$

Since in a horizontal pipe the static pressure drop $\Delta p_{\text{static}} = 0$ can be can be neglected here. The momentum pressure drop is calculated as

$$\Delta p_{\text{mom}} = G_{\text{total}}^2 \cdot \left\{ \left[\frac{(1-x)^2}{\varrho_{\text{L}}(1-\varepsilon)} + \frac{x^2}{\varrho_{\text{G}} \cdot \varepsilon} \right]_{\text{out}} - \left[\frac{(1-x)^2}{\varrho_{\text{L}}(1-\varepsilon)} + \frac{x^2}{\varrho_{\text{G}} \cdot \varepsilon} \right]_{\text{in}} \right\} \tag{3.35}$$

with

$$\varepsilon = \frac{x}{\varrho_{\text{G}}} \cdot \left[(1 + 0.12 \cdot (1-x)) \cdot \left(\frac{x}{\varrho_{\text{G}}} + \frac{1-x}{\varrho_{\text{L}}} \right) + \frac{1.18 \cdot (1-x) \cdot [g \cdot \sigma \cdot (\varrho_{\text{L}} - \varrho_{\text{G}})]^{0.25}}{G_{\text{total}}^2 \cdot \varrho_{\text{L}}^{0.5}} \right]^{-1}. \tag{3.36}$$

Here G_{total} stands for total mass flux of liquid and vapor and is defined as:

$$G_{\text{total}} = \frac{\dot{m}_{\text{total}}}{A_{\text{hyd}}}. \tag{3.37}$$

Didi's paper compares several correlations for frictional pressure losses. It shows that the correlation of Grönnerud [55] has the highest accuracy for intermittent flow and stratified-wavy flow. The correlation of Müller-Steinhagen and Heck[103] has the highest accuracy for annular flows.
In Grönnerud's [55] correlation the single-phase pressure drop of the liquid phase is multiplied by a two-phase factor. This gives the total pressure drop for the two-phase flow,

$$\Delta p_{\text{frict}} = \Phi_{\text{gd}} \cdot \Delta p_{\text{L}} \tag{3.38}$$

with

$$\Delta p_{\mathrm{L}} = 4 f_{\mathrm{L}} \cdot \left(\frac{L}{d_{\mathrm{hyd,swirl}}} \right) \cdot G_{\mathrm{total}}^2 \cdot . \cdot (1 - x)^2 \cdot \left(\frac{1}{2 \varrho_{\mathrm{L}}} \right). \tag{3.39}$$

Here f_{L} is the fluid friction factor which is determined as in Equation 3.40,

$$f_{\mathrm{L}} = \frac{0.079}{Re_{\mathrm{L}}^{0.25}} \tag{3.40}$$

with

$$Re_{\mathrm{L}} = \frac{G_{\mathrm{total}} \cdot d_{\mathrm{hyd,swirl}}}{\eta_{\mathrm{L}}}. \tag{3.41}$$

The indice L refers to the use of fluid properties to calculate the characteristic numbers. The factor for the two-phase flow can be calculated by the correlation in Equation 3.42 with the given hydraulic diameter of the swirl,

$$\Phi_{\mathrm{gd}} = 1 + \left(\frac{dp}{dz} \right)_{\mathrm{Fr}} \left[\frac{\varrho_{\mathrm{L}}}{\varrho_{\mathrm{G}} \cdot \left(\frac{\eta_{\mathrm{L}}}{\eta_{\mathrm{G}}} \right)^{0.25}} - 1 \right] \tag{3.42}$$

with

$$\left(\frac{dp}{dz} \right)_{\mathrm{Fr}} = f_{\mathrm{Fr}} \cdot \left[x + 4 \cdot \left(x^{1.8} - x^{10} \cdot f_{\mathrm{Fr}}^{0.5} \right) \right] \tag{3.43}$$

and

$$Fr_{\mathrm{L}} = \frac{G_{\mathrm{total}}^2}{g \cdot d_{\mathrm{hyd,swirl}} \cdot \varrho_{\mathrm{L}}^2}. \tag{3.44}$$

When the fluid Froude number $Fr_{\mathrm{L}} \leq 1$, the friction factor $f_{\mathrm{Fr}} = 1$ is set. Otherwise, it is calculated as in Equation 3.45,

$$f_{\mathrm{Fr}} = Fr_{\mathrm{L}}^{0.3} + 0.0055 \cdot \left(\ln \left(\frac{1}{Fr_{\mathrm{L}}} \right) \right)^2. \tag{3.45}$$

Since the penetration depth of the screw is variable, evaporator distances of different lengths are produced depending on the engagement length of the screw. However, since the capillary remains in the same place, a pre-swirl area is created in front of the screw. This is accounted for by two successive pressure drop correlations with different hydraulic diameter lengths. This is illustrated in Figure 3.9.

If the swirl is not in full engagement, the remaining length of the evaporator must be calculated with the proportional heat input to the total length plus a different hydraulic diameter as in Equation 3.46. The hydraulic diameter d_{hyd} of the spot evaporator and the pre-swirl area,

$$d_{\mathrm{hyd, \, pre\text{-}swirl}} = d_{\mathrm{bore}} - d_{\mathrm{cap}} \tag{3.46}$$

would be calculated in the same manner. The calculation of the two-phase pressure drop in the swirl is then determined with the correlations described above with the new output
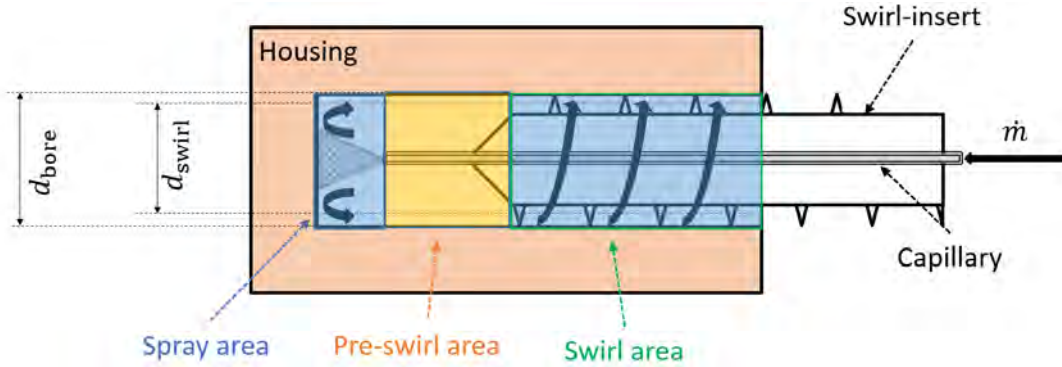
Figure 3.9.: Sliding swirl insert

pressure from the pre-swirl area. The swirl model has thus been extended with a pressure loss in the annular gap.

3.5.2. Heat Transfer Swirl

Determining the heat transfer in the swirl area with the highest possible accuracy is of great importance, since the lateral surface of the borehole accounts for approx. 97 % of the heat transfer area. A large number of correlations for estimating flow boiling have been proposed over the past 80 years: For example [31, 30, 122, 39, 48, 18, 104, 10, 132, 86, 88, 83, 56, 33, 24, 87].

As briefly mentioned in the previous chapter, none of the equations covers a range of a coil diameter D smaller than 50 mm and a pitch steeper than 10 mm but Hardick [58] comes to the conclusion that: "The circumferential averaged heat transfer coefficient during a saturated flow-boiling in a helical coil is same as a straight tube". Therefore, a number of correlations are proposed here. The correlation should cover a whole range from subcooled to nucleate boiling. An early correlation still quoted is the one of Chen [24]. He divided the heat transfer in two parts: A macro-convective and a micro-convective one. The macro-convective, or non boiling forced convection, is based on the single-phase Dittus-Boelter equation (liquid only) [39]. The micro-convective or nucleate boiling contribution is based on the equation for pool boiling by Foster and Zuber [48]. Chen combined both parts,

$$\alpha_{2\text{ph}} = f \cdot \alpha_{\text{L}} + s \cdot \alpha_{\text{pool}}, \tag{3.47}$$

to form a correlation which provides an overall heat transfer coefficient. Because there are much higher velocities in the two-phase flow compared to the liquid only one-phase flow there is a factor $f > 1$ included to represent that. The factor f was determined by correlating it with the Martinelli parameter. Due to the thinner boundary layer in forced convection than in pool boiling (lower superheat) a suppression factor $s < 1$ is needed in the correlation. The suppression factor can be obtained by correlating it with a two-phase Reynolds number. In the work of Chen [24] these factors are presented in diagrams, but Bergles [18] has established equations for the diagrams.

Shah Correlation

A different but still widely quoted approach for estimating heat transfer coefficients is the one of Shah [122]. Also in the correlation by Shah two different heat transfer mechanisms

are considered to apply: forced convection and nucleate boiling. In the case of Shah those two parameters are not added but the bigger one of the two is chosen [122]. An important part in the Shah correlations plays the boiling number Bo which was first described in a correlation by Mumm [104]. The famous Shah correlation

$$\alpha_{2\text{ph}} = max(E, S) \cdot \alpha_{\text{sp}} \tag{3.48}$$

with

$$\alpha_{\text{sp}} = 0.0023 \cdot Re_{\text{L}}^{0.8} \cdot Pr_{\text{L}}^{0.4} \cdot \frac{k_{\text{L}}}{d_{\text{hyd}}}, \tag{3.49}$$

is still widely used in the industry and for example also included in the internal functions of the program Engineering Equation Solver (EES). The correlation is valid for the geometric diameter of $6-25\,\text{mm}$ and for the media refrigerant and water [122]. E is the enhancement and S is the supression factor which can be calculated with

$$N = Co \,\text{if} \, (Fr_{\text{L}} \geq 0.04) \tag{3.50}$$

or

$$N = 0.38 Fr_{\text{L}}^{-0.3} Co \,\text{if} \, (Fr_{\text{L}} < 0.04) \tag{3.51}$$

with

$$Co = \left(\frac{1-x}{x}\right)^{0.8} \cdot \left(\frac{\varrho_{\text{G}}}{\varrho_{\text{L}}}\right)^{0.5} \tag{3.52}$$

and

$$Fr_{\text{L}} = \frac{G^2}{\varrho_{\text{L}}^2 \cdot g \cdot d_{\text{hyd}}}. \tag{3.53}$$

For $N > 1.0$,

$$S = \frac{1.8}{N^{0.8}} \tag{3.54}$$

and

$$E = 230 Bo^{0.5} \,\text{if} \, \left(Bo \geq 3 \cdot 10^{-5}\right) \tag{3.55}$$

or

$$E = 1 + 46 Bo^{0.5} \,\text{if} \, \left(Bo < 3 \cdot 10^{-5}\right). \tag{3.56}$$

For $0.1 < N \leq 1.0$,

$$S = \frac{1.8}{N^{0.8}} \tag{3.57}$$

and

$$E = F \cdot Bo^{0.5} \cdot e^{2.74N^{-0.1}}. \tag{3.58}$$

For $N \leq 0.1$,

$$S = \frac{1.8}{N^{0.8}} \tag{3.59}$$

and

$$E = F \cdot Bo^{0.5} e^{2.47N^{-0.15}} \tag{3.60}$$

with

$$F = 14.7 \, \text{if} \, \left(Bo \geq 11 \cdot 10^{-4} \right) \tag{3.61}$$

or

$$F = 15.43 \, \text{if} \, \left(Bo < 11 \cdot 10^{-4} \right). \tag{3.62}$$

Characteristic of the Shah correlation is the step function-like change of the heat transfer coefficient by taking the maximum value of E or S. This leads to the fact that in one area the heat transfer can still be predicted very accurately and by a small parameter variation in the next area no longer. This should result in Chapter 4 in the fact that for some geometries the values are acceptable and for others they could be very far off the mark.

Gungor and Winterton

The application of the correlation refers to refrigerants and water with diameters $3 - 32$ mm. Gungor and Winterton [56] modified the Chen correlation and their basic form of a heat transfer correlation is the enhancement factor multiplied by the proportion for the liquid only α_{L} by the Dittus-Boelter equation [39] to which an suppression factor S for the pool boiling equation, α_{pool} proposed by Forster and Zuber [48] is added,

$$\alpha_{2\mathrm{ph}} = E \cdot \alpha_{\mathrm{L}} + S \cdot \alpha_{\mathrm{pool}}. \tag{3.63}$$

α_{L} is given by the Dittus-Boelter equation (for liquid only flowing) in a pipe,

$$\alpha_{\mathrm{L}} = \frac{0.023 \cdot Re_{\mathrm{L}}^{0.8} \cdot Pr_{\mathrm{L}}^{0.4} \cdot \lambda_{\mathrm{L}}}{d_{\mathrm{hyd}}}. \tag{3.64}$$

In two-phase flows even for very small vapor qualities velocities are higher (and also the void fraction) and the boundary layer is thin. Therefore, for the same mass momentum G, an amplification factor E must be introduced which is much higher than for single-phase heat transfer. It is quite obvious that this effect depends on the liquid to gas density ratio $\varrho_{\mathrm{G}}/\varrho_{\mathrm{L}}$ and the quality x. It is a common practice to correlate this in the Martinelli parameter,

$$X_{\mathrm{tt}} = \left(\frac{1-x}{x} \right)^{0.9} \left(\frac{\varrho_{\mathrm{G}}}{\varrho_{\mathrm{L}}} \right)^{0.5} \left(\frac{\eta_{\mathrm{L}}}{\eta_{\mathrm{G}}} \right)^{0.1}. \tag{3.65}$$

Where η_L/η_G describes the dynamic viscosity ratio between the liquid and the gas phase. Not only the the axial velocities but also the generation of vapor in the boiling process itself disturbs the boundary layer and enhances the heat transfer and is given by the dimensionless number of the boiling number,

$$Bo = \frac{q}{\Delta h_{\text{evap}} \cdot G}. \tag{3.66}$$

So it is possible to write the enhancement factor E as a function of X_{tt} and Bo. In forced convection the boundary layer of the superheated liquid, in which the vapor bubble grows, is thinner than in pool boiling. Therefore the pool boiling term from equation 3.63 needs to be reduced by multiplying it with the suppression factor S. The extend of it is defined by the two-phase Reynolds number,

$$Re_{2\text{ph}} = E^n \cdot Re_L \tag{3.67}$$

provided in Chen [24]. Gungor and Winterton [56] investigated a number of literature expressions for α_{pool} and concluded that the best one is proposed by Cooper [33],

$$\alpha_{\text{pool}} = 55 \cdot p_r^{0.12} \left(-\log 10(p_r) \right)^{-0.55} M^{-0.5} \dot{q}^{0.67}. \tag{3.68}$$

Care should be taken not to confuse the reduced pressure $p_r = p/p_{\text{crit}}$ with the Prandel number Pr. They came to the conclusion that the enhancement factor E can be expressed as

$$E = 1 + 24000 \cdot Bo^{1.16} + 1.37 \left(1/X_{\text{tt}} \right)^{0.86} \tag{3.69}$$

and the suppression factor S can be represented as

$$S = \frac{1}{1 + 1.15 \cdot 10^{-6} \cdot E^2 \cdot Re_L^{1.17}}. \tag{3.70}$$

They also suggested to calculated the heat transfer in saturated boiling (all values are calculated at the saturation temperature)

$$\alpha_{2\text{ph}} = E \cdot \alpha_L + S \cdot \alpha_{\text{pool}} \tag{3.71}$$

with

$$\alpha_L = 0.023 Re_L^{0.8} \cdot Pr_L^{0.4} \cdot \frac{\lambda_L}{d_{\text{hyd}}} \tag{3.72}$$

and

$$\alpha_{\text{pool}} = 55 \cdot P_r^{0.12} \cdot \left(-log_{10} P_r \right)^{-0.55} M^{-0.5} q^{0.67}. \tag{3.73}$$

Additionally they found out that for certain Froude numbers the enhancement factors E_2 (in their case $Fr < 0.05$) should be calculated by

$$E_2 = Fr^{0.1-2Fr} \tag{3.74}$$

and the suppression factor S_2 should be calculated as

$$S_2 = \sqrt{Fr}. \tag{3.75}$$

Lazarek and Black Correlation

The correlation was used for the refrigerant R-113 with a pipe diameter of 3.15 mm while boiling [83]. Lazarek and Black suggested a simply correlation based on 738 experimental data sets on the boiling of saturated R-113 in a pipe with an inner diameter of 3.15 mm and indicated that the heat transfer coefficient showed a strong dependence on the heat flux with insignificant influence of the vapor quality, which indicates that the mechanism of nuclear boiling controls the heat transfer process at the wall [132],

$$\alpha_{2\mathrm{ph}} = \frac{30 Re_{\mathrm{L}}^{0.857} \cdot Bo^{0.714} \cdot \lambda_{\mathrm{L}}}{d_{\mathrm{hyd}}} \tag{3.76}$$

with

$$Re_{\mathrm{L}} = \frac{G \cdot d_{\mathrm{hyd}}}{\mu_{\mathrm{L}}} \tag{3.77}$$

and

$$Bo = \frac{\dot{q}}{G \cdot \Delta h_{\mathrm{evap}}}. \tag{3.78}$$

Kew-Cornwell Correlation

A modified formula of the Lazarek-Black equation was proposed by Kew and Cornwell [69] to account for the observed increase in the heat transfer coefficient with steam quality in larger tubes [132],

$$\alpha_{2\mathrm{ph}} = 30 \cdot Re_{\mathrm{L}}^{0.857} Bo^{0.714} (1 - x)^{-0.143} \cdot \frac{\lambda_{\mathrm{L}}}{d_{\mathrm{hyd}}}. \tag{3.79}$$

Sun and Mishima Correlation

The Sun and Mishima correlation is valid for refrigerants and water with pipe diameters from 0.21 - 5.5 mm. Lazarek and Black [83] suggested that the predominant boiling process is nucleate boiling. The fact that the correlation predicts the database well also suggests that nucleate boiling may be the main mechanism. The result that nucleation dominates was also supported by studies of boiling in small channels [135]. Tranet al. [135] and Yu et al. [145] introduced the Weber number, i.e., the ratio of inertia and surface tension of the fluid, in their correlations for calculating the heat transfer in small channels and found that the heat transfer coefficient was weakly dependent on the pore quality, similar to Lazarek and Black. However, when looking at trends in experimental data, it was found that the heat transfer coefficient was much more dependent on the Weber number than on the vapor quality, so a new correlation was developed based on the Lazarek-Black correlation, taking into account the effect of the Weber number. Using the regression method, the following equation [132],

$$\alpha_{2\mathrm{ph}} = \frac{6 \cdot Re_{\mathrm{L}}^{1.05} Bo^{0.54}}{We_{\mathrm{L}}^{0.191} \cdot \left(\frac{\varrho_{\mathrm{L}}}{\varrho_{\mathrm{G}}}\right)^{0.142}} \cdot \frac{\lambda_{\mathrm{L}}}{d_{\mathrm{hyd}}} \tag{3.80}$$

is obtained. The Weber number for the liquid phase is calculated as

$$We_{\mathrm{L}} = \frac{G^2 \cdot d_{\mathrm{hyd}}}{\sigma \cdot \varrho_{\mathrm{L}}}. \tag{3.81}$$

3.6. Critical Heat Flux in the Swirl

As the CHF usually limits the amount of heat transferred, a collapse of the cooling process and a subsequent failure of the heated surface may occur once exceeding CHF. In order to calculate the CHF in the swirl evaporator, it must be taken into account that the radius of the curvature as well as the pitch of the geometry might effect the CHF. The number of empirical CHF correlations has increased steadily over the last 50 years. It is now well over 1000 correlations for water-cooled tubes alone [54]. This large number of CHF prediction methods suggests that the CHF mechanism is complex. No single theory or equation can be applied to all CHF conditions. The complexity of CHF prediction increases significantly when additional factors such as transients, non-uniform flow distributions and asymmetric cross sections are considered. Since no correlation was found which covers the exact phenomenon and geometry of a swirl evaporator, several correlation and methods are compared and discussed:

- Yagov correlation [142]

- Qi correlation [113]

- Groeneveld's method [54]

Yagov Correlation

The correlation of Yagov offers the possibility to give a statement about the CHF in the wet steam region by an interpolation between the gaseous and liquid CHF,

$$\dot{q}_{\mathrm{CHF,sat}} = \left(\dot{q}_{\mathrm{CHF,L}}^3 + \dot{q}_{\mathrm{CHF,G}}^3 \right)^{1/3} \tag{3.82}$$

with

$$\dot{q}_{\mathrm{CHF,G}} = 0.06 \cdot \Delta h_{\mathrm{evap}} \cdot \varrho_{\mathrm{G}}^{0.6} \cdot \sigma^{0.4} \cdot \left(\frac{g \cdot (\varrho_{\mathrm{L}} - \varrho_{\mathrm{G}})}{\mu} \right)^{0.2} \tag{3.83}$$

and

$$\dot{q}_{\mathrm{CHF,L}} = 0.5 \cdot \frac{\Delta h_{\mathrm{evap}}^{81/55} \cdot \sigma^{9/11} \cdot \varrho_{\mathrm{G}}^{13/110} \cdot \lambda^{7/110} \cdot f(Pr) \cdot g_{\mathrm{z}}^{21/55}}{\nu^{1/2} \cdot c_{\mathrm{p}}^{3/10} \cdot R_{\mathrm{i}}^{79/110} \cdot T_{\mathrm{wall}}^{21/22}} \tag{3.84}$$

with

$$f(Pr) = \left(\frac{Pr^{9/8}}{1 + 2Pr^{1/4} + 0.6Pr^{19/24}} \right)^{4/11}. \tag{3.85}$$

In addition, it is possible to adapt the correlation to a pipe swirl flow. This is done in this work by replacing the acceleration due to gravity occurring in the correlation by the centrifugal acceleration occurring in the swirl. This is to increase the CHF of the liquid phase by simulating an increase of the liquid film occurring at the wall by the larger

centrifugal acceleration. To do so the acceleration due to gravity g from the original papers [140, 141] in Equation 3.83 and Equation 3.84 is replaced by $g_c = \pi^2 \cdot c_a^2 / (2y^2 D_i)$ and results in

$$g_c = \frac{\pi^2 \cdot c_a^2}{2y^2 \cdot d_{hyd,swirl}}. \tag{3.86}$$

The twist ratio is given by $y = P/D_b$. D_b is the bore diameter of the bore in which the swirl evaporator is inserted. It is the same bore diameter as shown in Figure 3.6.

Qi Correlation

The correlation of Qi has actually been validated for liquid nitrogen but is suitable for the same geometrical orders of magnitude as well as the same mass flow rates. Another advantage of this correlation is the low error deviation of less than $\pm 30\%$. Since the acceleration due to gravity lowers the CHF, the adjustment of the correlation by replacing the acceleration due to gravity with the centrifugal acceleration makes little sense for this correlation,

$$\dot{q}_{CHF} = (0.214 + 0.14 Co) \cdot \left(\frac{\varrho_G}{\varrho_L}\right)^{0.133} \cdot \left(\frac{1}{We}\right)^{0.333} \frac{G \cdot \Delta h_{evap} \cdot d_{hyd,swirl}^2}{d_{hyd,swirl}^2 + 0.03L} \tag{3.87}$$

with

$$Co = \left(\frac{\sigma}{g \cdot (\varrho_L - \varrho_G) \cdot d_{hyd,swirl}^2}\right) \tag{3.88}$$

and

$$We_L = \frac{G^2 \cdot d_{hyd,swirl}}{\sigma \cdot \varrho_L}. \tag{3.89}$$

Groeneveld's Method

Due to the complexity of predicting the CHF with a correlation Groenevend et al. [54] developed a look-up table (which is basically a normalized data base) to predict the CHF. The look-up table predicts the CHF as a function of the refrigerant mass flux (G), its pressure (p) and vapor quality (x),

$$CHF = f(G, p, x). \tag{3.90}$$

They researched the CHF for flow boiling of water in $8\,\text{mm}$ vertical tubes for more than 30.000 data points with pressure, vapor quality and mass flux as varying parameters. The values in between are obtained by interpolation. In order to extrapolate to other diameters, the authors proposed the equation

$$CHF = \frac{CHF_{8\,\text{mm}}}{\sqrt{\frac{d_{hyd}}{8\,\text{mm}}}}. \tag{3.91}$$

The Groeneveld method seems to have several advantages over correlation-based CHF prediction methods, such as

- ease of use

- wide application range

- no iteration required

- based on a very large database

- there is no need to choose among the many CHF prediction methods that are currently available

Groeneveld's look-up table appears to be the Swiss Army knife among the methods of CHF determination. Because of its 30.000 data points the estimation of the CHF in the swirl evaporator should be relatively accurate.

Since the CHF for flow boiling is lower than for spray cooling and since the CHF occurs towards the end of the evaporator section, i.e. with low vapor contents, the swirl area was identified as the section which limits the heat transfer and in which the CHF occurs. For the above mentioned reasons variation of the method proposed by Groeneveld was used [54] for calculating the CHF in the swirl evaporator.

A certain heat flux $\dot{Q}_{\text{swirl}}$ is absorbed in the evaporator section of the swirl area. The quantity is defined by the specific enthalpy of evaporation Δh_{vap}, the mass flow rate $\dot{m}$ and the change in vapor quality between inlet x_{in} and outlet x_{out},

$$\dot{Q}_{\text{swirl}} = \dot{m} \cdot \Delta h_{\text{vap}} \cdot (x_{\text{out}} - x_{\text{in}}). \tag{3.92}$$

The inlet vapor quality can be determined using the specific enthalpies h,

$$x_{\text{in}} = \frac{h_{\text{in}} - h_{\text{l}}}{h_{\text{g}} - h_{\text{l}}}. \tag{3.93}$$

Using Groeneveld's look-up table, the local CHF can be determined at the current (local) vapor quality x. Using the exit vapor content x_{out} for x here, it would show how much "reserve" is left before the CHF is reached. This works because CHF decreases with increasing quality and therefore CHF is reached first at the evaporator outlet (before it starts to grow in the upstream direction).
The exit vapor quality x_{out} corresponding to the vapor content at which the CHF occurs is called the critical vapor quality $x_{\text{crit.}}$,

$$\text{CHF}_{\text{swirl}} = f(p, G, x_{\text{crit.}}, d_{\text{hyd}}) \tag{3.94}$$

with

$$G = \frac{\dot{m}}{\frac{\pi \cdot d_{\text{hyd}}^2}{4}}. \tag{3.95}$$

The maximum transmissible heat flow $\dot{Q}_{\text{max}}$ can therefore be calculated by multiplying $\text{CHF}_{\text{swirl}}$ by the heat transferring area A_{swirl} (here the lateral surface area of the borehole defined by its length and its diameter $A_{\text{swirl}} = \pi \cdot d_{\text{bore}} \cdot l_{\text{bore}}$),

$$\dot{Q}_{\text{max}} = \text{CHF}_{\text{swirl}} \cdot A_{\text{swirl}}. \tag{3.96}$$

$x_{\text{crit.}}$, thus serves as an indicator whether the CHF is reached and at which power the departure from nucleate boiling (DNB) occurs or whether it occurs at all (as long as $x_{\text{out}} < x_{\text{crit.}}$ the DNB does not occur). So if the outlet vapor quality x_{out} is below the critical vapor quality $x_{\text{crit.}}$, the entire swirl region is in the nucleate boiling range, resulting in a correspondingly low wall superheat as displayed in Fig. 3.10.
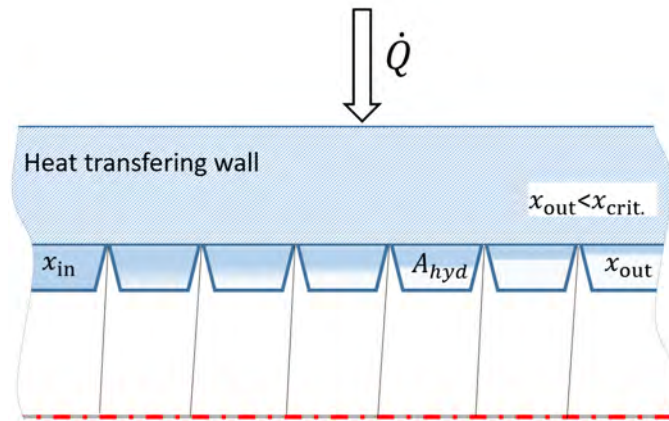
Figure 3.10.: Heat transfer in the swirl area for $x_{\text{out}} < x_{\text{crit.}}$

The exit vapor quality corresponding to the vapor quality at which CHF occurs (i.e., $x_{\text{crit.}}$), a small insulating vapor film forms at the evaporator exit. This point is reflected in a slight increase in wall superheat as shown in Figure 3.11.
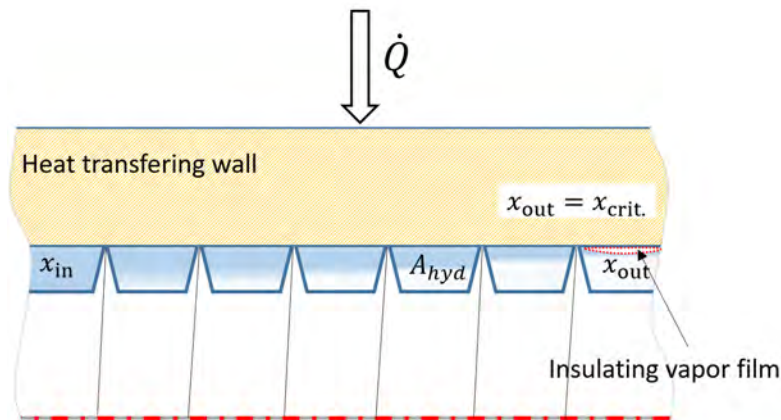
Figure 3.11.: Heat transfer in the swirl area for $x_{\text{out}} = x_{\text{crit.}}$

Since less heat can be transferred at this local point because of the insulating film, but the average heat flow remains constant, the heat flux at the remaining upstream heat transfer surface increases. This leads to a continued increase in wall superheat which then results in film boiling in further upstream areas of the swirl path. Figuratively speaking, the insulating vapor film spreads from the outlet upstream along the evaporator section as illustrated in Figure 3.12.
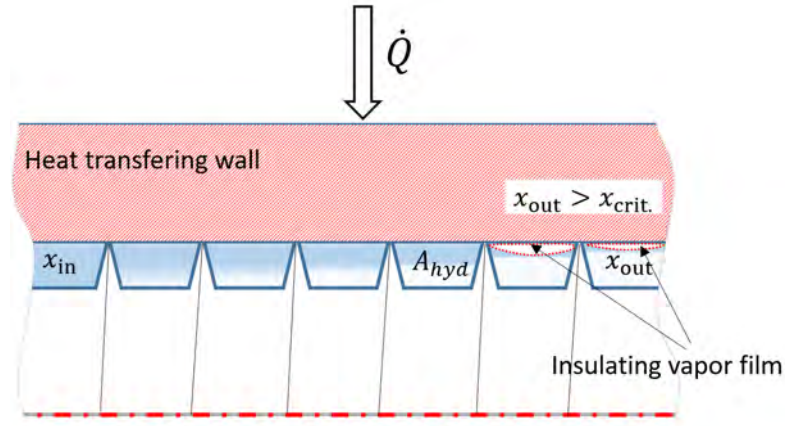
Figure 3.12.: Heat transfer in the swirl area for $x_\text{out} > x_\text{crit.}$

The insulating vapor film occurring at $x_\text{out} = x_\text{crit.}$ can be seen as the "nucleus" of film boiling and the impending collapse of the cooling process as shown in Figure 3.11. After that point the CHF is reached, DNB starts and the vapor film increases.

The vapor quality x_out with which the refrigerant exits the swirl section at the end of the evaporator section is therefore the critical parameter $x_\text{crit.}$ that can be used to evaluate whether CHF occurs or not. At $x_\text{out} = x_\text{crit.}$ CHF occurs. By inserting

$$x_\text{out} = x_\text{crit.} \tag{3.97}$$

in Equation 3.92, $\dot{Q}_\text{crit}$ can be calculated as

$$\dot{Q}_\text{crit} = \dot{m} \cdot \Delta h_\text{vap} \cdot (x_\text{crit} - x_\text{in}). \tag{3.98}$$

By equating the two equations Equation 3.96 and Equation 3.98,

$$\dot{Q}_\text{max} = \dot{Q}_\text{crit}, \tag{3.99}$$

the maximum heat flow that can be transferred under the prevailing conditions is obtained,

$$\text{CHF}_\text{swirl}(p, G, x_\text{crit.}, d_\text{hyd}) \cdot A_\text{swirl} = \dot{Q}_\text{crit} \tag{3.100}$$

and the heat flux could be calculated with

$$\text{CHF}_\text{swirl} = \frac{\dot{Q}_\text{crit}}{A_\text{swirl}} \tag{3.101}$$

or with Equation 3.94 now that x_crit is known. Figure 3.13 shows the curve of $\dot{Q}_\text{swirl}$ and $\dot{Q}_\text{crit}$ 2 as a function of the outlet vapor quality x_out. The critical vapor quality x_crit can be read from the intersection of the two curves. At this point, the CHF is reached.
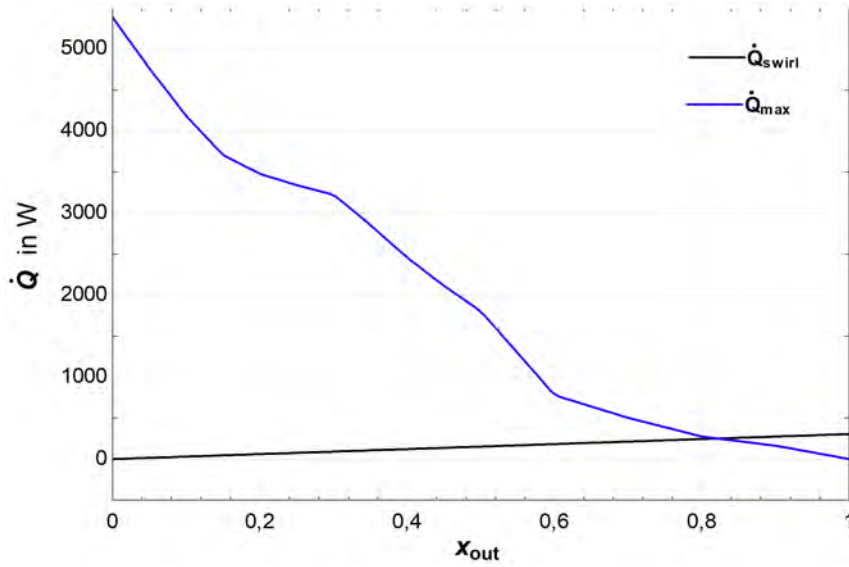
Figure 3.13.: Performance curve for $\dot{Q}_{\text{swirl}}$ and $\dot{Q}_{\text{max}}$

3.7. Hydraulic Optimization of the Swirl Geometry

The two-phase pressure drop is calculated from the sum of momentum pressure drop Δp_{mom}, friction pressure drop Δp_{frict} and static pressure drop. Since in a horizontal pipe the static pressure drop $\Delta p_{\text{static}} = 0$ can be can be neglected.

The friction pressure loss Δp_{frict} depends on the geometrical conditions such as evaporator length and diameter and on manufacturing conditions such as surface roughness. To achieve an improvement that is independent of geometry and manufacturing process, momentum pressure drop Δp_{mom} must be minimized. Δp_{mom} occurs when refrigerant is accelerated or decelerated. To minimize Δp_{mom}, the flow velocity must therefore be kept constant.

In a swirl evaporator that uses a screw or helical geometry with a constant step the flow velocity c of the refrigerant increases because it evaporates as it flows through the evaporator section. Due to the higher quality and lower mixed density the volume flow increases,

$$\dot{V} = \frac{\dot{m}}{\varrho} \tag{3.102}$$

and because

$$c = \frac{\dot{V}}{A_{\text{hyd}}}, \tag{3.103}$$

the flow velocity increases, too. In order to minimize the momentum pressure drop Δp_{mom} the flow velocity should be kept constant. This can be achieved by increasing the cross-sectional area A_{hyd} simultaneously in the right proportion,

$$\frac{\mathrm{d}V}{\mathrm{d}t} \cdot \frac{\mathrm{d}z}{\mathrm{d}A_{\text{hyd}}} = const.. \tag{3.104}$$

In a discretized model this can be expressed as

$$c[i] = c[i+1] = const. \qquad\qquad (3.105)$$

or

$$\frac{V[i]}{A[i]} = \frac{V[i+1]}{A[i+1]} = const., \qquad\qquad (3.106)$$

respectively.

In practice, this means that the screw with a constant step size is changed to a screw with variable step size as shown in Figure 3.14 to maintain a constant flow velocity of the refrigerant and therefore minimize momentum pressure loss. (This has the additional benefit of minimizing the evaporation temperature slide without the use of azeotropic mixtures).
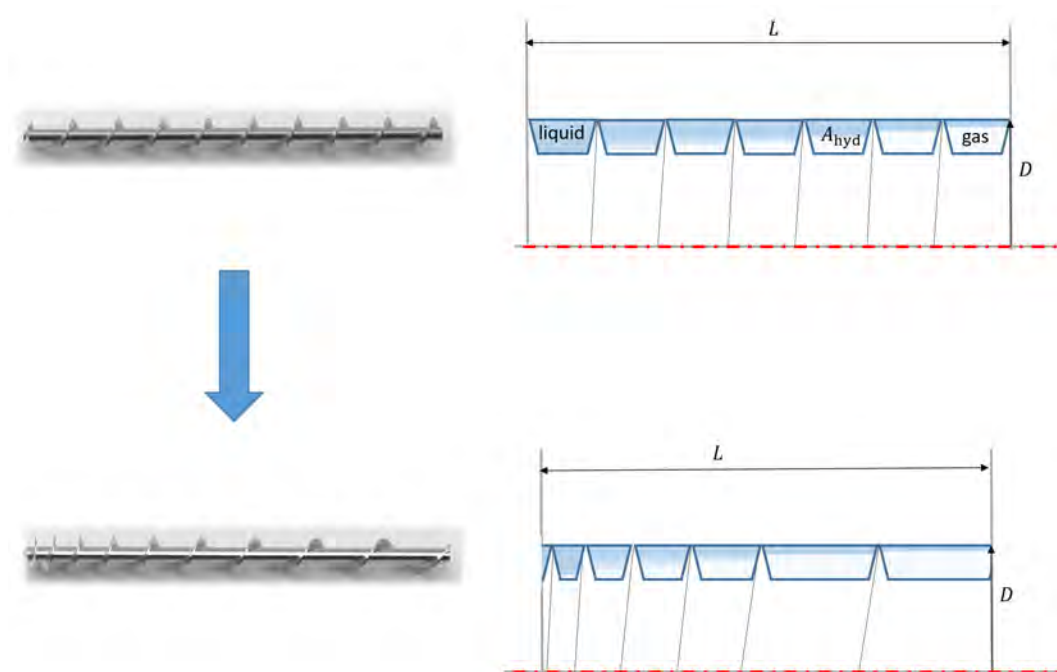
Figure 3.14.: Screw or helical evaporator geometry with constant and variable step [46]

4. Experimental Examination

This chapter presents the measuring test section i.e. the swirl evaporator test carrier and the measuring circuit. It describes which experiments were carried out to obtain evidence-based knowledge about the pressure loss, heat transfer coefficient (HTC) and critical heat flux (CHF) in a swirl evaporator system. In the first section of this chapter, the test carrier for the swirl evaporator itself is presented and the way how it was designed is described. The second section describes the test rig, its sensors, the data acquisition and the experimental uncertainties. Since this system is fundamentally new, extensive screening tests are performed. In the next stage of the screening experiments, a statistical design of experiments was carried out in order to prove main influences on the process with statistical certainty within a confidence interval of 95 %. In the following section, the inverse principle for determining the HTC is described together with the corresponding FEM model.

4.1. Measuring Section: Swirl Evaporator Test Carrier

Figure 4.1 shows the functional sketch of the swirl evaporator test carrier. The screw engagement length can be varied either by moving the adapter along the longitudinal axis or by replacing the screw by using a longer or shorter screw. To vary the position of the adapter, the circumferential screws must be loosened. Thus, the O-rings return to their original position and no longer put pressure on the adapter. The swirl evaporator test support is also free-standing to reduce the influence of external interferences and to concentrate the heat conduction path on the refrigerant inside. Each additional bearing point degrades the thermal insulation. The bearing point on the U-profile is therefore as far away as possible from the heat input of the heater band. Five temperature measuring points, which are displayed in Figure 4.3, are provided for measuring the temperature profile from the spray cooling to the exit of the swirl.

Figure 4.1.: Swirl evaporator with variable screw engagement length [44]

In Figure 4.2, the entire evaporator is shown in cross-section. The housing and adapter are made of copper. The housing contains a stepped blind hole. The right side of the

housing shows the adapter through which the capillary tube enters from the right side and terminates at the exit of the screw. On the left side of the adapter there is a screw connection which helps fixing the screw. After the adapter, the outlet of the gaseous refrigerant can be seen. The outlet can be connected to the system with the help of a sc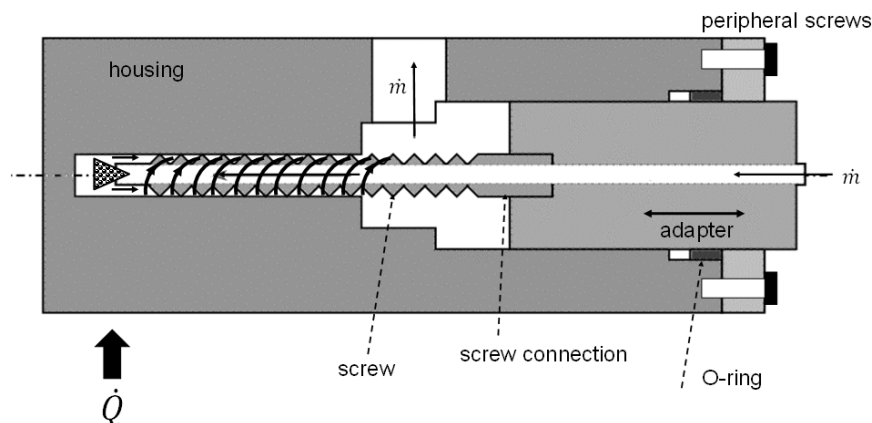rew connection. On the left side of the housing there are holes for thermocouples. The holes are of different lengths in order to be able to measure the temperature at different points of the housing. The system is sealed gas-tight with three sealing rings. In the entrance area of the capillary tube to the adapter is also threaded. The screw in the thread has also been eroded so that the capillary tube can be passed through. At the end of this screw is a small O-ring to seal the capillary tube passage.

In the middle of the adapter there is an O-ring. This seals the housing against the adapter. The O-ring is followed by a clamping ring. This exerts pressure on the inner O-ring and holds it in position. After the clamping ring comes another O-ring. This seals the adapter and housing from the outside. The cylindrical blind hole into which the screw is inserted has an inner diameter of 4.5 mm, into which a suitably turned screw or 3D-printed screw geometries can be inserted. A through-hole with a diameter of 0.85 mm was eroded into the screw and screw-shaped geometries were micro-cast (the screw-shaped geometries created using the stereolithography process were already printed with a through-hole). A capillary tube with an outer diameter of 0.8 mm and an inner diameter of 0.5 mm is guided in this through-hole. The capillary tube is made of drawn stainless steel. A fitting is brazed to the right side of the capillary to connect the swirl evaporator test support to the rest of the cold test stand.
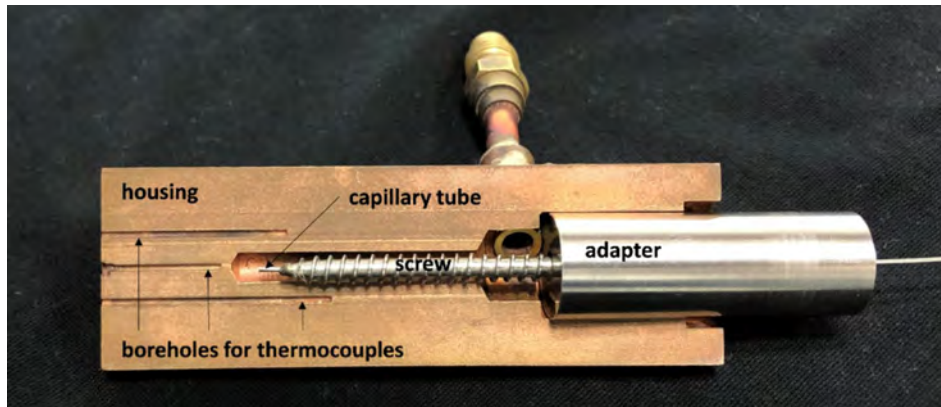
Figure 4.2.: Profile of a swirl evaporator with hydraulically relevant parts [47]

To minimize external influences, the design is in an insulated housing. The heater tape, which is attached around the housing and is the heat source for all the experiments, is not shown in this illustration.

The thermocouples measure the temperature in different positions of the housing to obtain a temperature field which in Section 4.8 is used for the estimation of local heat transfer coefficients via inverse thermal analysis. The position of the 5 thermocouples are shown in Figure 4.3. The exact dimensions are displayed in Figure 4.3. The exact position of the thermocouples can also be seen in Table 4.1.
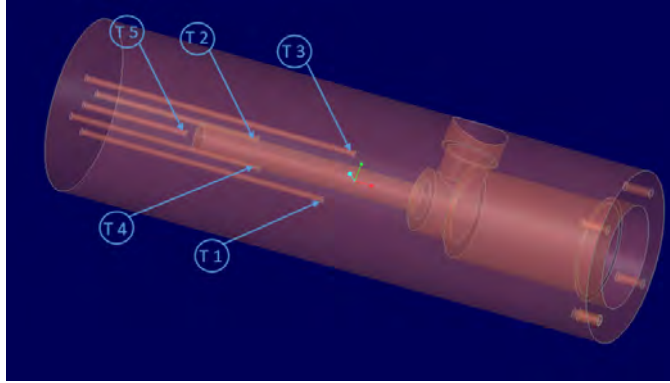
Figure 4.3.: Positions of the thermocouples in 3-D

Table 4.1.: Position of the thermocouples

No.	Axial position	Radial position
T 1	45 mm	5 mm
T 2	30 mm	5 mm
T 3	50 mm	5 mm
T 4	35 mm	5 mm
T 5	19 mm	central

4.2. Representation of Measuring Cycle

The refrigeration test stand is basically a normal refrigerant cycle with a number of auxiliaries to control superheat, subcooling and condensing temperature. The test stand and measuring section contain a total of 22 sensors for logging pressures, temperatures, mass flow and the performances of the main and auxiliary aggregates. In addition, the cooling load, which is introduced into the measuring section in the form of a heating jacket, can be set and controlled. The test stand is set up in an air conditioned room which is regulated to 22 °C. In Figure 4.4 the RI flow diagram of the test stand is shown. In Table 4.2 the components of the test setup are listed. The photo of the test stand is shown in Figure 4.5.
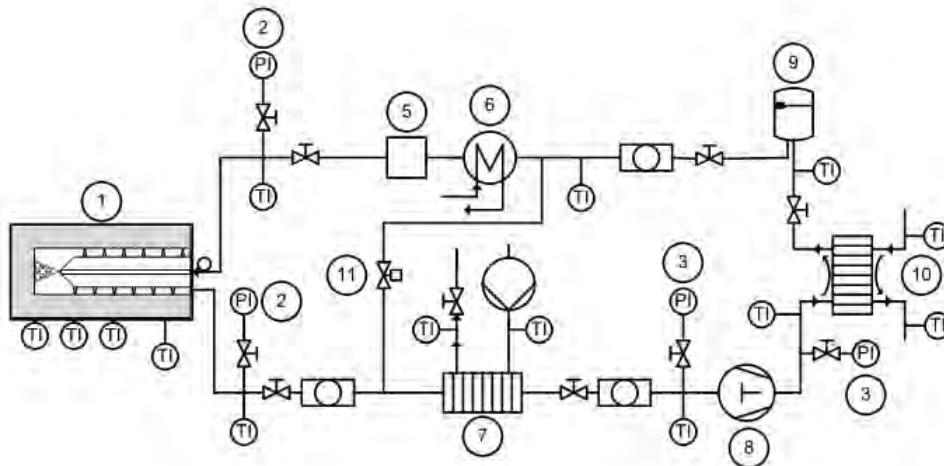
Figure 4.4.: RI flowchart of the experimental setup (mod. from [75])

The refrigeration test stand has suitable connections to connect the swirl evaporator test section to the rest of the refrigeration cycle. After the refrigerant has passed through the evaporator test section (1) (shown in Figure 4.4 and Figure 4.5), the temperature and pressure (2) are measured to determine the thermodynamic state after the test section. Before the refrigerant flows to the oil-free two-piston compressor (8), it passes through a plate heat exchanger (7). This is coupled to a water-glycol circuit which has the task of evaporating and superheating the refrigerant so that only gaseous refrigerant is entering the compressor. On the one hand, this ensures compressor safety; on the other hand, the mass flow can also be controlled via the density of the gas. However, it is important to keep the superheat at a constant temperature within a test series to ensure constant test conditions. Condensation then takes place in a plate heat exchanger (10), which is connected to a thermostat via a water-glycol cycle. Based on the discharge temperature of the refrigerant from the plate heat exchanger, the discharge temperature of the thermostat is selected to provide the desired condensing pressure in the circuit. After condensation, the refrigerant is directed to a collector (9). Then the liquid refrigerant flows into a finned tube heat exchanger (6). Here, too, a water-glycol mixture serves as heat transfer medium for another thermostat which controls the subcooling temperature. The subcooling is set and measured by the temperature difference between the temperature of the refrigerant at the outlet of the receiver and the liquid temperature at the inlet to the capillary (1). All temperatures are measured with type J thermocouples.

After the liquid refrigerant flows through the heat exchanger to set the subcooling, the mass flow and density of the refrigerant are measured with a Coriolis mass flow meter (5). Before entering the capillary, temperature and pressure of the refrigerant are measured with a temperature and a pressure sensor (2), and the thermodynamic state of the refrigerant is calculated using these values. An inner diameter of 4 mm is chosen for the liquid lines to minimize the pressure losses. In the application, the pressure losses in the liquid line are measured at $p_c = 11$ bar resulting in a pressure loss of $\Delta p = 200$ mbar. The suction line has a diameter of 9 mm. Stainless steel 1.4301 is used as the line material. All lines are sheathed with Armaflex foam insulation. The layer thickness of the insulation is 10 mm and have a thermal conductivity of 0.03 W/(m K) at 0 °C. Because of the Armaflex insulation, the assumption of an adiabatic piping system is made. Components causing
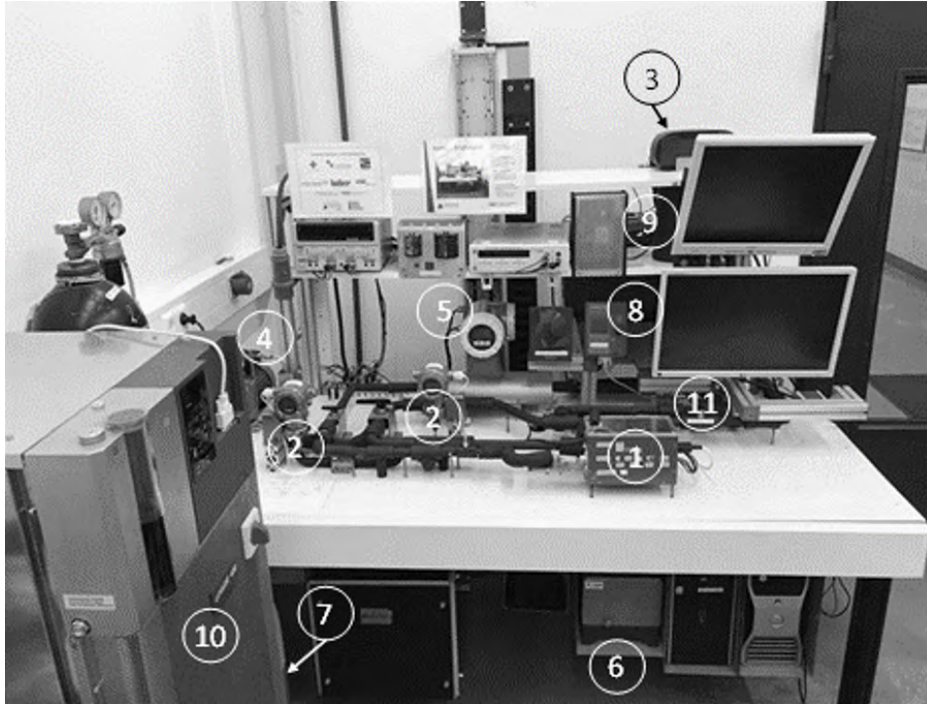
Figure 4.5.: Photograph of the test stand [44]

Table 4.2.: Components of the test setup

No.	Designation	Manufacturer	Value range
1	Swirl evaporator and capillary support	In-house production	
2	Pressure sensor	Endress+Hauser	$0-1\,\mathrm{MPa}$
3	Pressure sensor	Endress+Hauser	$0-1\,\mathrm{MPa}$
4	Vacuum pump	D.V.P	$0.01\,\mathrm{mbar}$ abs.
5	Coriolis mass flow meter	Endress+Hauser	$0-30\,\mathrm{kg/h}$
6	Thermostat, subcooler	Peter Huber GmbH	$-25-150\,°\mathrm{C}$
7	Post evaporator	In-house production	
8	Compressor	REFCO	$33\,\mathrm{kg/h}$; gas-phase
9	Refrigerant assembler	ESK Schulze	
10	Thermostat, condenser	Peter Huber GmbH	$40-250\,°\mathrm{C}$
11	Bypass valve, step motor controlled	Peter Huber GmbH	$0.75\,\mathrm{mm}$
-	Power meter	HAMEG	$1\,\mathrm{mW}-8\,\mathrm{kW}$
-	DC power supply	Gwinstek	$0-30\,\mathrm{V}$, $3\,\mathrm{A}$
-	Data acquisition	National Instruments	$32\,\mathrm{bit}$
-	Computer	Dell	
-	Thermocouples Type J	TMH GmbH	$-50-150\,°\mathrm{C}$

vibrations are separated from the circuit by hoses and are vibration damped by foam mats.

4.3. Data Acquisition and Processing

A/D converters from National Instruments (NI) and LabVIEW are used to implement the data acquisition and processing of the test bench. Figure 4.6 shows the circuit diagram and Table 4.2 lists the components. All thermocouples are processed via the NI-9211 and NI-9213 A/D converters. A maximum resolution of 0.02 K possible due to an integrated cold junction compensation and work on a 24-bit basis, which both boards have. With this, a calibrated accuracy of 0.1 K can be achieved over the complete temperature measurement chain. This ensures that accuracy of data acquisition can be reproduced and processed.
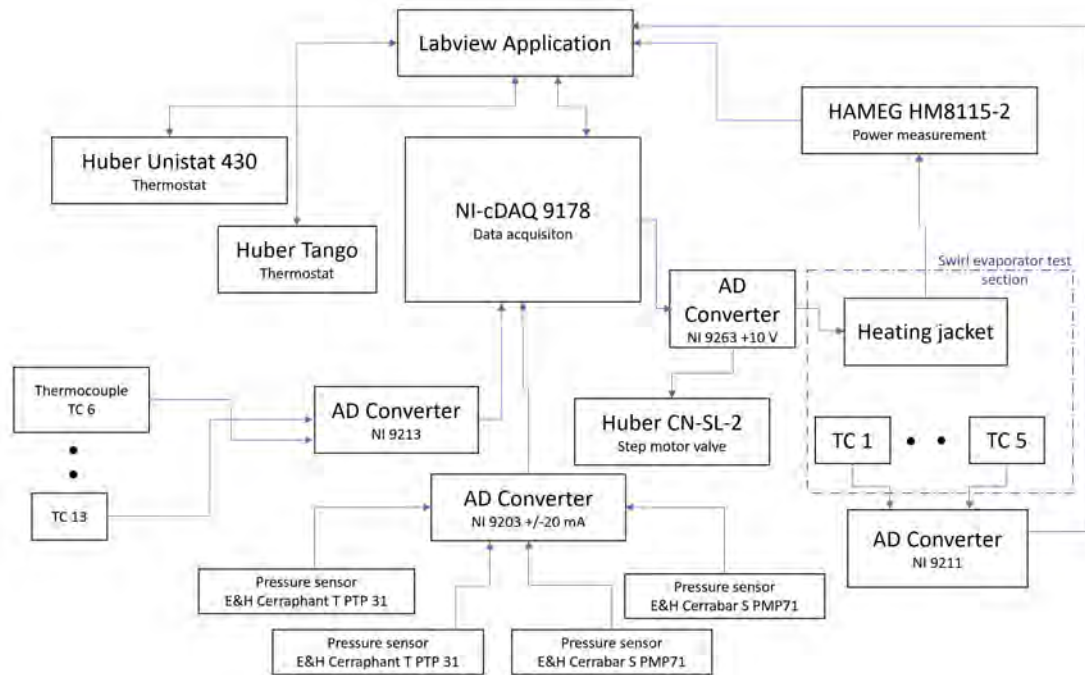
Figure 4.6.: Schematic of data acquisition and processing

The measuring signals of the pressure sensors and the mass flow meter are converted in an NI-9203 A/D converter. In the 4 to 20 mA range, the transducers supply the signals analogously as current signals. Since the sampling rate of 2 Hz is implemented on the test bench, this is not decisive for the decision whether a current or voltage signal is used. Current signals were chosen because they are not susceptible to interference from external influences. For the error tolerances of the various sensors, the sampling rate of the A/D converter is 16 bits, which is a sufficiently high resolution.

The test bench uses the software programmed in LabVIEW, various valves and a NI-9263 control card for control. The output signal is a voltage signal of ± 10 V and the working resolution is 16 bits. This control card controls both the stepper motor controlled expansion valve and the power of the heating tape around the sample chamber. By feeding back the power of the heater band to LabVIEW via the power meter, the power control loop is closed. Direct integration of the thermostats for subcooling control and condensing pressure control into LabVlEW allows direct control therein. Alternatively, the control can be also set manually. The changes of the measured values over a longer period of time are graphically displayed in the user interface, as well as evaporation temperature, evaporation pressure, condensation pressure and mass flow. The graphical user interface shows the curve progression of all measured data for the past 20 minutes. This enables

the identification of steady-state operating conditions. The value for the discretization of all processes (e.g sampling rates and speed of the individual control loops) in the test bench was determined according to the Nyquist-Shannon sampling theorem [124]. The sampling theorem states that a signal can be accurately reconstructed from a sequence of equally sized samples if it was sampled at a frequency that is at least twice as high. Since the system time constant is about $1-2$ seconds, the measured values are recorded every $500\,\mathrm{ms}$, i.e. with a clock rate of $2\,\mathrm{Hz}$. The data is then written to a .CSV file together with the header, which provides information about which signal comes from which sensor. Depending on the evaluation case, this file is then evaluated using Excel, Matlab or EES.

4.4. Estimation of System-related Uncertainties

According to DIN 1319 [1], the essential task of measurements is to detect the actual value. Due to the fact that no measurement can detect the true value, deviations will occur in all measurements. These are quantified in the form of a error bar or error band around the actual value. These deviations result of the following causes:

1. Error in the conversion in the measuring chain

2. Calibration errors of the measuring equipment

3. Manufacturing tolerances

4. External influences that cannot be taken into account

5. Error of the measuring person, etc.

As shown in Figure 4.7, a measurement chain consists of several elements. Each of these elements can be subject to uncertainties and thus cause a deviation from the actual measured value.
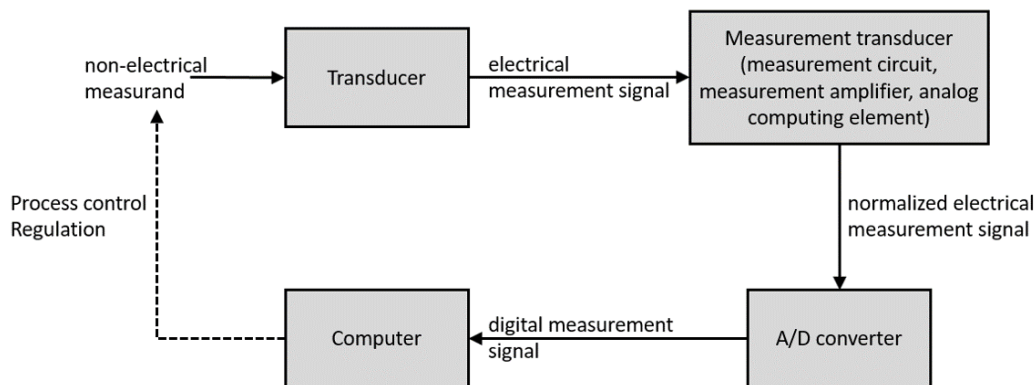
Figure 4.7.: Elements of a measuring system [136]

The uncertainty factor can be divided into relative and absolute factors for transducers. The relative factor e_{rel} is dimensionless and refers to the maximum measuring range of the respective measuring device,

$$e_{\mathrm{rel}} = \frac{x_{\mathrm{m}} - x_{\mathrm{real}}}{x_{\mathrm{m}}}. \tag{4.1}$$

It should be mentioned that in this subsection, the variable x refers to a measured value and not the vapor quality. The absolute factor e_{abs} is the difference between the measured value x_{m} and the real value x_{real}, expressed by the equation

$$e_{\text{abs}} = x_{\text{m}} - x_{\text{real}}. \tag{4.2}$$

The uncertainty factors that are used in the experimental setup, are listed in Table 4.3.

Table 4.3.: Absolute and relative factors of the measuring equipment

Designation	Measured quantity	Calibrated range	Value range		Factor
Cerabar S PMP71	$p_{\text{c}}, p_{\text{o}}$	$0-25$	$0-10$	MPa	$\pm\,0.05\,\%$ of the measuring range
Promass 83A	$\dot{m}$	$0-25$	$0-30$	kg/h	$\pm\,0.1\,\%$ of the measured value
Ministat 125-cc	T_{sub}	$-25-450$	$-25-450$	°C	$\pm\,0.1\,\text{K}$
Unistat 430	T_{c}	$-50-90$	$-40-250$	°C	$\pm\,0.01\,\text{K}$
HM 8115-2	P	$0-500$	$0.001-8$	W	$\pm\,0.8\,\%$ of the measured value
Thermocouple Typ J	$T_{\text{o}}, T_{\text{c}}, T_1-T_5,$	$-50-200$			

For sums and differences in simple equations, the absolute factors can be added and for products or quotients the relative factors have to be multiplied. The statistical factor e_{stat} and the dynamic factor e_{dyn} result in the total factor of a measurement e,

$$e = e_{\text{stat}} + e_{\text{dyn}}. \tag{4.3}$$

If input and output of a measured value in the measurement chain have a time offset, dynamic factors occur. Dynamic factors can be neglected in this test, since the measurements were carried out under stationary operating conditions. Static factors are composed of stochastic factors e_{sto} and systematic measurement deviations e_{sys}. The measurement factor is a result of these two factors

$$e_{\text{stat}} = e_{\text{sto}} + e_{\text{sys}}. \tag{4.4}$$

Accurate calibration of the measurement technique can eliminate the systematic factor, which is usually a constant offset. The stochastic factor of a measurement is more difficult to determine, since there are various factors that have an influence:

- Measuring chain error

- Noise of sensors

- Environmental influences

- Interpretation errors, etc.

By repeating measurements several times and forming an average, the stochastic factor can be counteracted. Relative factors of the measurement means can be found in stochastic factors. Normal distributions, such as the Gaussian normal distribution, are used to counter stochastic factors. The sampling of measurements of all sensors was done with a frequency of $2\,\mathrm{Hz}$. A mean value was created from 1200 individual values, which represents the elaborated measurement results of this work. The 1200 individual values correspond to a measurement time of 10 minutes under unchanged conditions. Averaging of the individual measurements x_i is determined as

$$\bar{x}_\mathrm{i} = \frac{1}{n} \sum_{j=1}^{n} x_{ij}. \tag{4.5}$$

The empirical standard deviation can be described as

$$s = \sqrt{\frac{1}{n-1} \sum_{j=1}^{n} \left(x_{ij} - \bar{x}\right)^2} \tag{4.6}$$

and describes the mean square deviation of the arithmetic mean. From the previous calculations, the uncertainty u

$$u = \frac{1}{\sqrt{n}} \cdot s \tag{4.7}$$

can be determined by limiting finite measured values. In addition, the extreme values x_min and x_max are formed from the 1200 values of a measurement with unchanged conditions. The target variable $\bar{y}$, which is a function of $\bar{x}_\mathrm{i}$, can be given by the equation

$$\bar{y} = f(\bar{x}_\mathrm{i}). \tag{4.8}$$

The purpose of this calculation is to determine how the uncertainties in each of the measured variables x propagate to the value of the calculated quantity y. Where the partial differential $\partial \bar{y}$ represents the uncertainty of the variables and is represented by

$$\partial \bar{y} = \sqrt{\sum_{i=1}^{n} \left(\frac{\partial y}{\partial x_\mathrm{i}} |_{\partial \bar{x}_\mathrm{i}} \partial \bar{x}_\mathrm{i}\right)^2}. \tag{4.9}$$

To determine uncertainties for the CHF, the pressure drop and the HTC, a function integrated in EES was used to determine the uncertainty. The uncertainty for the calculation of the pressure loss is $9.6\,\%$ and for the CHF is $7.7\,\%$. Since different heat transfer models have been presented, the respective model-specific uncertainties are shown in Table 4.4.

4.5. Experimental Procedure

Before each series of measurements, the system is operated for at least one hour to ensure that it is in a stable operating state. Before the start of each measurement series, it can be selected whether the power change in the heating tape is to take place as a step or as a ramp function. In addition, the slope of the ramp function can be determined. A ramp

Table 4.4.: Heat transfer model-specific uncertainties

Correlation	Uncertainty
Gungor-Winterton	9.7 %
Kew-Cornwell	9.1%
Shah	14.5 %
Sun-Mishima	7.1 %
Lazarek-Black	9.1 %

has the advantage that the power is not changed in one jump, but in smaller steps, so that the system is overshooting less. For each measurement, the power is increased by 10 W every 10 minutes when the temperatures are in steady state and do not change by $\pm 0.3\,°C$ (the ramp function increases the power by 1 W every 2 seconds, so an increase of 10 W takes 20 seconds). In this band, the temperature can be assumed to be constant (i.e., the standard deviation in subsequent evaluation is less than $0.05\,°C$). If the temperature rises even though the power is constant, the power is not increased until either a steady state is reached or the temperature in the evaporator rises to $20\,°C$. At an evaporator temperature of $20\,°C$, it can be assumed that equilibrium is no longer present and the CHF has been reached.

4.5.1. Set of Experiments: Group A

Two different set of experiments have been defined. In the first set or "Group A", screws or helical evaporator geometries of different engagement length were tested with the same hydraulic diameter. This extends or shortens the helical evaporator path. Thus, the influence of the length of the evaporator section on HTC, CHF and pressure loss in the helical evaporator section can be determined. By changing the adapter, the engagement length of the screw or evaporator geometry can be varied as desired. The capillary tube can also be adjusted as desired, but for the settings in Group A it always remains in the same position. Illustration of the principle and the variation in Group A is shown in Figure 4.8. The screw is pulled outwards incrementally or removed completely in the last step. An experiment without a screw corresponds to the functional principle of the spot evaporator. A fully engaged screw refers to 100 % engagement and a evaporator with no screw refers to 0 % engagement. These interrelationships are also shown in Table 4.5.
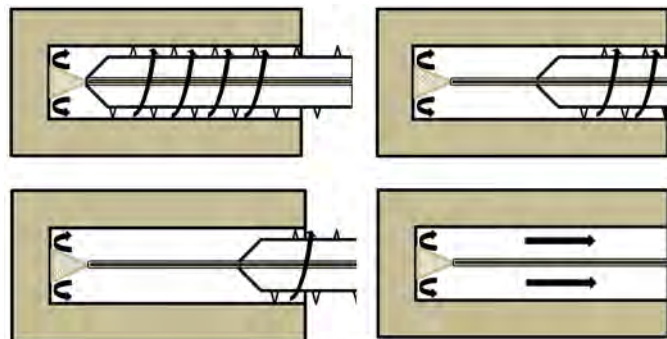
Figure 4.8.: Illustration of the variation of the engagement length

For the experiments performed in Group A, machined stainless steel Spax screws were

used. The outer diameter d_a is 4.5 mm and the core diameter d_i is 3.2 mm. The flank distance or pitch is 2.25 mm.

Table 4.5.: Screw lengths, windings and pitches

No.	Percentage engagement length in %	Engagement length in mm	Engagement windings	Pitch in mm
1.	100	33.75	15	2.25
2.	67	22.50	10	2.25
3.	40	13.50	6	2.25
4.	7	2.25	1	2.25
5	0	0	0	–

At full engagement length, the maximum engagement is 40 mm. This is reached at measurement No. 1. This results in a loss of 6.25 mm through the tip for each screw, so the effective engagement length is set to 33.75 mm for 100 % engagement length.

The "uncoiled" evaporator can be calculated according to [107] with

$$L = \sqrt{P^2 + 4\pi^2 r^2} \cdot \frac{S}{P}. \tag{4.10}$$

The used mean radius for the calculation was measured with 3.85 mm. Where P is the pitch, r the mean radius of the screw and S the engagement length as shown in Figure 4.9.
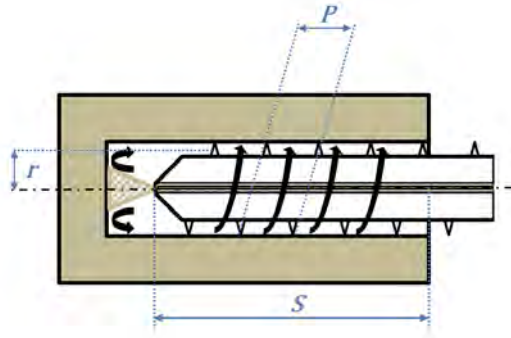
Figure 4.9.: Radius, pitch and engagement length of a swirl geometry

In Table 4.6 are the resulting uncoiled engagement lengths and hydraulic diameters listed. The hydraulic diameter is calculated [21] as

$$d_{hyd} = \frac{4 \cdot A}{U}. \tag{4.11}$$

Where A is the measured area in Figure 4.10 and U the perimeter of this area. The measured areas and perimeters are arithmetically averaged, the hydraulic diameter calculated and the deviation determined. Table 4.6 shows the relationship between the engagement of the screw length, windings and pitches.
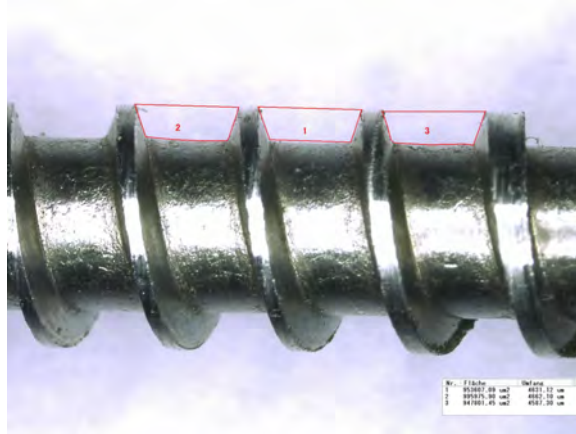
Figure 4.10.: Flow cross-sectional areas and wetted perimeters for a screw with 2.25 mm
pitch

Table 4.6.: Uncoiled engagement lengths and hydraulic diameter

No.	Uncoiled engagement length in mm	Hydraulic diameter in mm	Deviation in mm
1.	115.57	0.835	$+0.020$ -0.011
2.	77.05	0.835	$+0.020$ -0.011
3.	46.22	0.835	$+0.020$ -0.011
4.	7.70	0.835	$+0.020$ -0.011

4.5.2. Set of Experiments: Group B

In the second set of experiments or "Group B", the hydraulic diameter is varied by using
screws or helical evaporator geometries with different pitches. The screws have been
manufactured from an AlSi7Mg0.6 alloy using the micro-casting process. Due to the
constant installation space, the evaporator distance is also shortened by the increasing
pitch as indicated in Figure 4.11. However this can be accepted since the influence of
the evaporator length was already determined in the set of experiments in Group A. The
variations in Group B are shown in Figure 4.11.
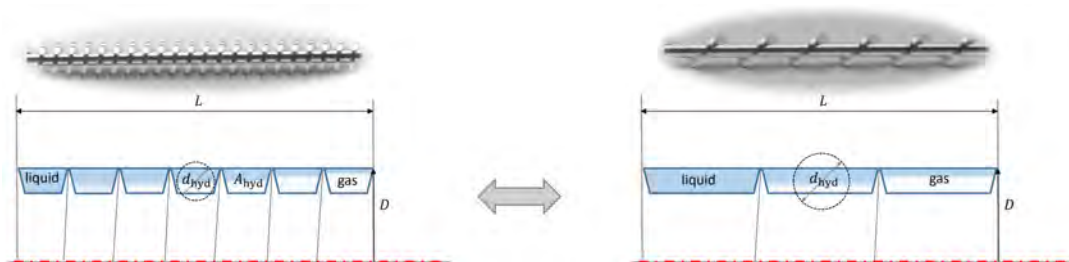
Figure 4.11.: Illustration of the variations in experimental Group B

Figure 4.11 also shows the micro-casted swirl inserts with a pitch of 2 mm on the left and 7 mm on the right. The pitch of these swirl inserts are constant over the entire length of the component.

The bore in which the swirl geometry is inserted has a depth of 40 mm and a diameter of 4.5 mm. This means that if no swirl geometry is inserted (spot evaporator), the evaporation distance is 40 mm and the hydraulic diameter is 3.7 mm, since the outer diameter of the capillary tube must be subtracted from the bore diameter to obtain the effective flow diameter/hydraulic diameter. This case is shown in Table 4.7 under number 7. If helical geometries or screws are inserted into this bore, the evaporator distance is extended because the refrigerant, due to the helix, covers a longer distance before it exits the bore. At the same time, however, the hydraulic diameter decreases. Helical geometries or screws with different pitches lead to different evaporator lengths for the same (full) engagement length and, consequently, to different hydraulic diameters. The relationship between pitch, hydraulic diameter and evaporator length (uncoiled engagement length) is shown in Table 4.7. A small pitch results in a smaller hydraulic diameter and a longer evaporator length, whereas a large pitch results in a larger hydraulic diameter and a shorter evaporator length. No. 6 of Table 4.7 refers to the swirl with the optimized geometry and a variable pitch as presented in section 3.7.

Table 4.7.: The measured screw lengths, windings and the resulting pitches

No.	Percentage engagement length in %	Uncoiled Engagement length in mm	Hydraulic diameter in mm	Pitch in mm
1.	100	180.720	0.835	2
2.	100	123.272	1.270	3
3.	100	79.086	1.488	5
4.	100	68.686	1.638	6
5.	100	61.572	1.807	7
6.	100	79.086	variable	$1-9.6$
7.	100	-	3.7	-

To keep the outlet point of the refrigerant constant, a capillary is used. The capillary is made of stainless steel 1.2343 and has a brass cap on the high pressure side to connect the test carrier with the remaining part of the refrigeration cycle. Figure 4.12 shows a picture of the capillary tube and the frontal view of the screw through which the capillary tube is guided. The capillary is held in place by the sealing ring and the swirl in the center of the bore, which ensures that the refrigerant is sprayed on the center of the blind bore. The swirl insert is placed in the capillary so that it comes out of the swirl to ensure correct spraying of the refrigerant.
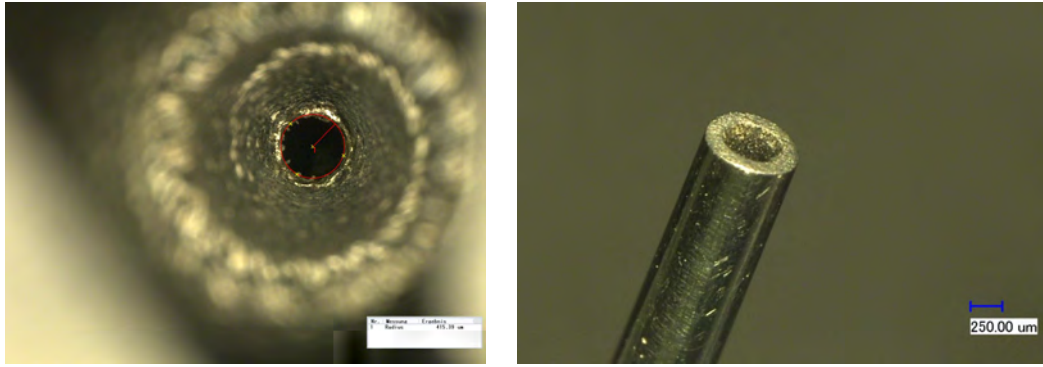
Figure 4.12.: Frontal view of the screw (left) and photo of the capillary tube (right)

4.6. Experimental Analysis

In the following, the entire analysis and simulation is analyzed and simulated on the basis of an area (swirl with a pitch of 6 mm) as an example. This procedure was carried out for all measurements. The experimental unit was left running at 200 W for about one hour after each start-up to ensure a stable state of temperatures and pressures. In the first step, the acquired raw data is converted into an Excel sheet for further processing. Then, from the available data, the evaporation pressure p_{o}, condensation pressure p_{c}, mass flow $\dot{m}$, electrical power P_{el} of the heating tape and temperatures of thermocouples T_1–T_5 are plotted in graphs. For a better overview, the electrical power is displayed together with the temperatures of the thermocouples T_1–T_5.

Figure 4.13 clearly shows the power jumps. The power starts at 190 W. In the following analysis, a range of values is sought at which mass flow, condensation pressure, evaporation pressure, temperatures and power are constant. In this example it would be in the range between measuring points 3600 and 5200. This range has been illustrated with a red box. As described in Section 4.4, the mean values (in this case temperatures) of the respective ranges (of constant power), as well as the standard deviation and upper and lower extreme values are determined.

The same procedure is done for mass flow, condensation and evaporation pressure. The diagram for mass flow is shown in Figure 4.14, the one for evaporation and condensation pressure is shown in Figure 4.15.
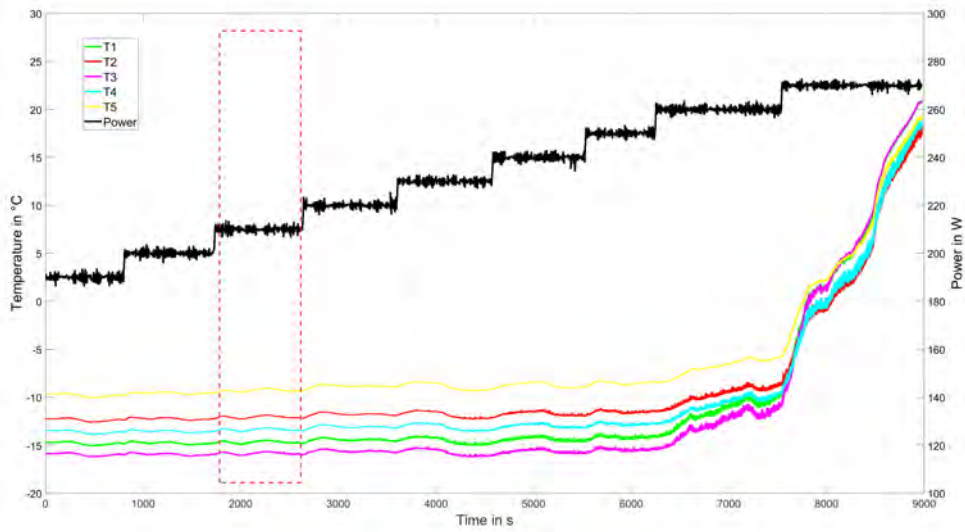
Figure 4.13.: Power and corresponding temperature curve in the swirl evaporator
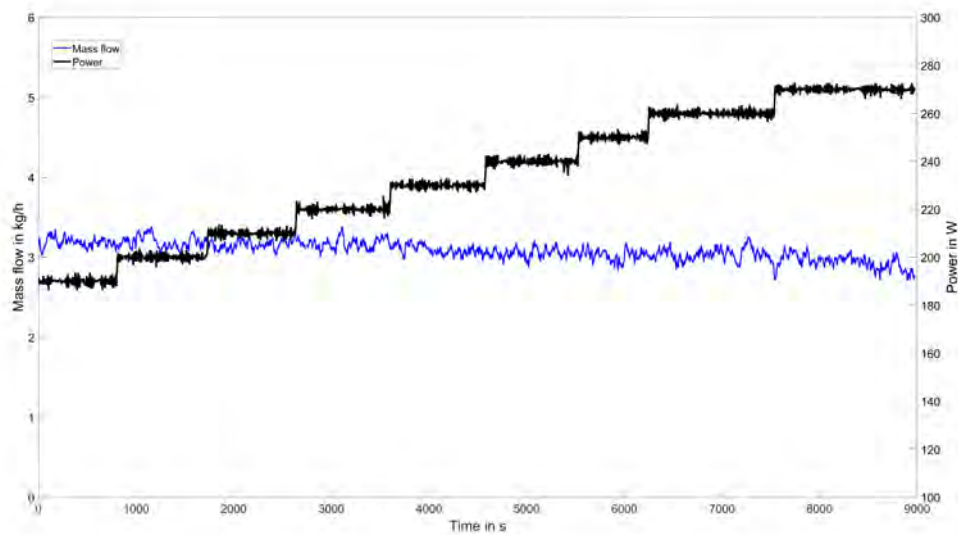
Figure 4.14.: Power and corresponding mass flow curve in the swirl evaporator
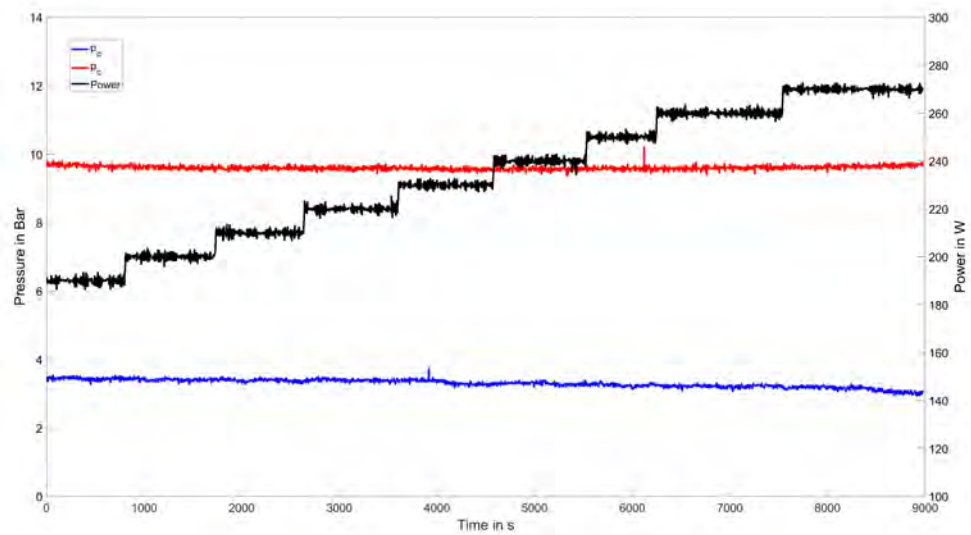
Figure 4.15.: Power and corresponding curves for p_o and p_c in the swirl evaporator

The experimentally determined pressure drop, which is compared in the following chapter with the simulated pressure drop, can be read directly from Figure 4.15, in which mean values of the condensation pressure are subtracted from the mean value of the evaporation pressure for a constant power range. The CHF can also be read from the graph. As long as the system is in the nucleate boiling range, an increase in power is only reflected in a small change in the measured temperature. As soon as the CHF is exceeded, however, the temperature rises abruptly from one power increase to the next, as visualized in Figure 4.16.
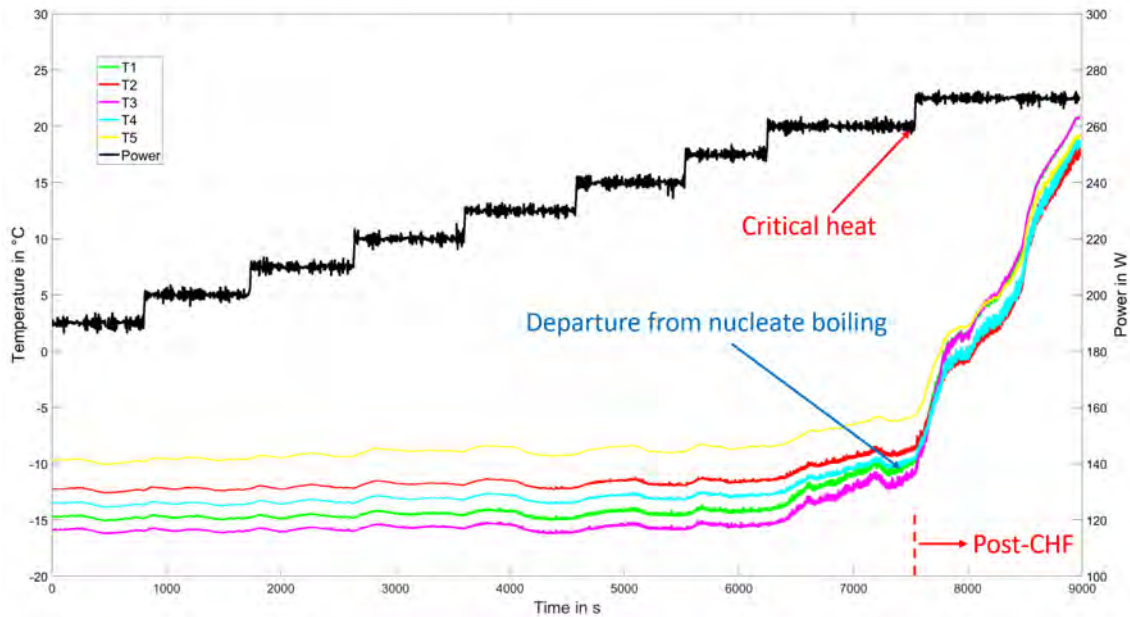
Figure 4.16.: Determining the CHF through the course of the temperature curves

4.7. Screening Experiments

A design of experiments (DoE) was performed to find the statistically significant influencing parameters and to identify interaction between influencing factors and target variables. In order to find these, a series of experiments were carried out with different swirl inserts presented in Section 4.5. Another reason for choosing this method is the possibility to realize an efficient planning and evaluation of test series. To determine the total number of trials $N_{V,total}$ the approach

$$N_{V,total} = N_{levels}^{N_{factors}} \tag{4.12}$$

is used. The number of factors $N_{factors}$ is the number of parameters that can be set. The number of levels N_{levels} indicates how many settings can be made on a factor [74].To create a statistical experimental design, the program Minitab is used, to design the experiments, plot graphs and carry out the statistical analysis. Due to the already integrated DoE function it offers a simple and fast evaluation of the experiments. The experimental plan is shown in Table 4.8. The results of the measurements are shown in Table 4.9

Table 4.8.: Experimental plan

Test No.	d_{hyd} in mm	Engagement length in %	Subcooling in K
1	0.8	40	7
2	0.8	60	7
3	0.8	90	7
4	0.97	40	7
5	0.97	20	7
6	0.97	20	7
7	0.97	40	7
8	0.97	0.0	7
9	0.95	10	7
10	0.95	90	7
11	0.95	90	0
12	0.95	80	7
13	0.95	80	7
14	0.95	70	7
15	0.95	70	7
16	0.95	60	7
17	0.95	60	7
18	0.95	60	3
19	0.95	60	0
20	0.95	50	7
21	0.95	50	7
22	0.95	40	7
23	0.95	40	0
24	0.95	40	7

Table 4.9.: Experimental results

Test No.	d_{hyd} in mm	Engagement length in %	Subcooling in K	Heat power in W	Mass flow in kg/h
1	0.8	0.4	7	220	1.74
2	0.8	0.6	7	255	1.77
3	0.8	0.9	7	240	2.01
4	0.97	0.4	7	270	2.21
5	0.97	0.2	7	255	2.29
6	0.97	0.2	7	255	2.12
7	0.97	0.4	7	260	2.45
8	0.97	0	7	240	2.21
9	0.95	0.1	7	210	1.93
10	0.95	0.9	7	260	2.02
11	0.95	0.9	0	220	1.95
12	0.95	0.8	7	240	1.88
13	0.95	0.8	7	250	1.08
14	0.95	0.7	7	250	2.22
15	0.95	0.7	7	270	1.38
16	0.95	0.6	7	290	2.25
17	0.95	0.6	7	320	1.55
18	0.95	0.6	3	210	1.82
19	0.95	0.6	0	210	1.85
20	0.95	0.5	7	240	1.83
21	0.95	0.5	7	250	1.97
22	0.95	0.4	7	210	1.79
23	0.95	0.4	0	190	1.59
24	0.95	0.4	7	160	1.44

In Figure 4.17 the main effect diagram for the mass flow is shown. It shows the effect intensity on the mass flow of each individual parameter, independently of each other. The y-axis shows the mean values of the mass flow. The dashed line is a reference line and corresponds to the total mean value of the mass flow, in this case $\dot{m} = 1.9\,\text{kg/h}$ On the x-axis the levels of the respective parameters are listed. There is a main effect if the connecting lines are not parallel to the x-axis. The greater the gradient of the connecting lines, the greater the effect. If the slope is positive or negative, the main effect is positive or negative for the target variable.
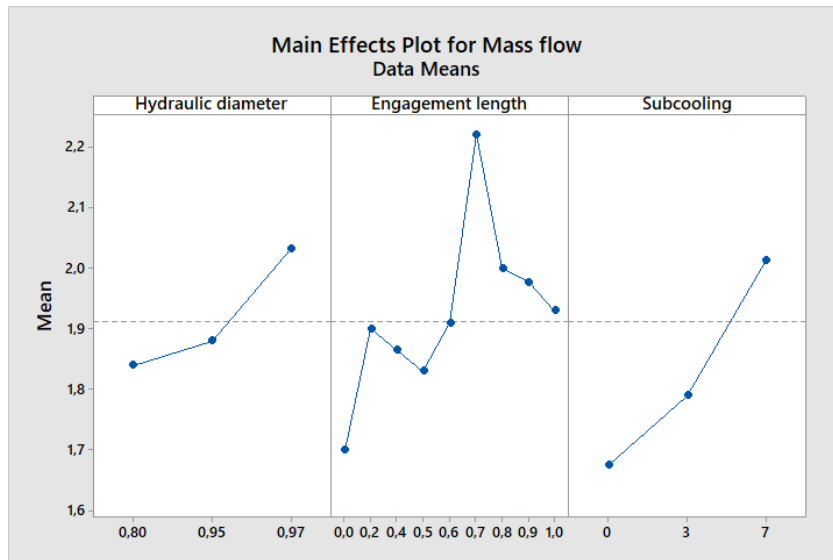
Figure 4.17.: Mass flow main effect diagram

In Figure 4.18, the main effects of the parameters concerning the heating power are shown. The total mean value of the heating power in this example is $P_{\text{el}} = 238\,\text{W}$.
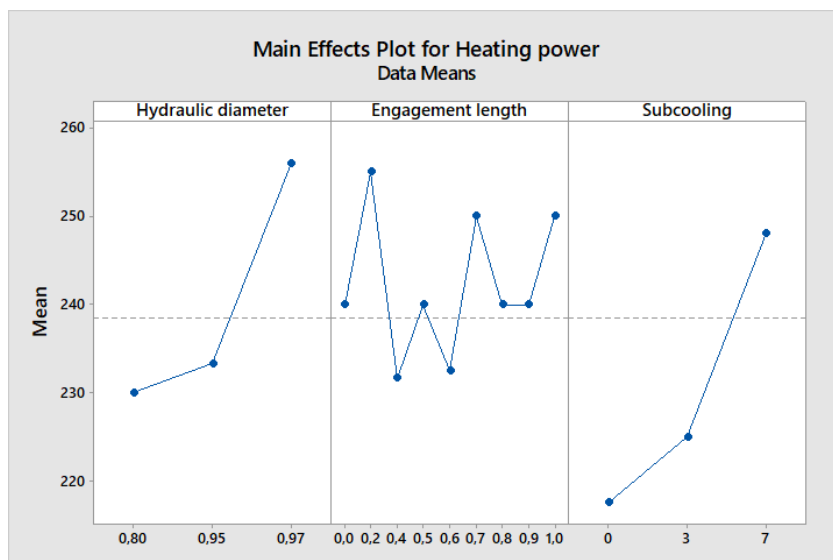
Figure 4.18.: Main effect diagram of the heating power

In a measuring range from 0.8 mm to 0.97 mm, the effect of the hydraulic diameter increases positively throughout. From 0.95 mm, the main effect is greater. This can be seen from the

steeper course of the connecting line. This means that the larger the hydraulic diameter, the higher the mass flow. Increasing the hydraulic diameter from 0.8 mm to 0.97 mm favors an almost linear increase in heating power.

Up to a proportion of 20 % of the intervention length, almost no major effect is detectable. This means that with 0 to 20 % engagement, the value of the mass flow remains almost constant. If a screw is engaged up to halfway (50 %), the mass flow increases. At 50 to 80 % engagement, the main effect is negative due to the slope direction of the connecting lines and the mass flow decreases. At 90 % engagement, the mass flow increases sharply and decreases when the screw is fully engaged. The cooling capacity increases in an engagement length range of 0 to 60 %. The strongest increase in cooling capacity occurs when the screw is engaged 50 to 60 %. The heating power decreases again when the screw is almost to completely (90 to 100 %) engaged. Subcooling up to 3 K increases the mass flow slightly. If subcooling is applied at 7 K, the mass flow increases more strongly. Subcooling up to 7 K leads to an increase in cooling capacity.

The Pareto diagram in Figure 4.19 lists all parameters to be set manually. It shows the influence on the mass flow. The dashed line is a reference line. Depending on a significance level or alpha level $\alpha = 0.05$, the reference line is placed at an effect value of 2.365. (So only in this subsection α has the meaning of significance level and not HTC.) Based on the bar length, it seems that the hydraulic diameter has the largest effect on the mass flow. The engagement length, on the other hand, seems to have the least influence on the mass flow. Only the hydraulic diameter exceed the dashed reference line, which indicates that only this parameter seems to be statistically significant.
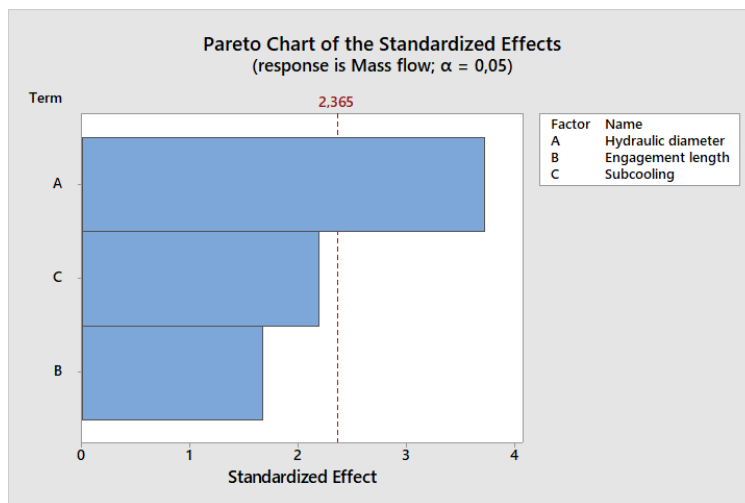
Figure 4.19.: Pareto diagram for the mass flow rate

Here, depending on the significance level or alpha level $\alpha = 0.05$, a reference line is placed at an effect value of 2.365. Regarding the heating power (or cooling capacity, depending on the point of view), which is shown in Figure 4.20, the influence of subcooling is the largest. The screw engagement length influences the heating power the least. None of the listed parameters seem to be statistically significant, as all of them are below the reference line.
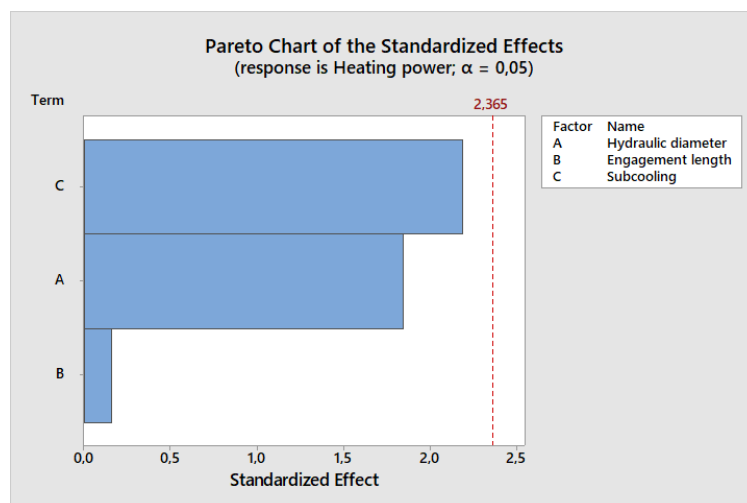
Figure 4.20.: Pareto diagram for the heating power

4.8. Inverse Calculation Method for Determination of Heat Transfer Coefficient

In the Inverse Thermal Analysis, a number of different HTCs are simulated in the FEM model at corresponding evaporation pressure and the simulated temperature fields are compared with the temperature field measured in the test carrier. The simulated temperature field which corresponds most closely to the measured one, thus reflects the conditions prevailing in the test. In this way, HTCs can be determined inversely.

Due to the complexity of the geometry and boundary conditions, a numerical method is used for analysing the heat transfer phenomena. In the past, a variety of numerical methods have been used to solve heat transfer problems [139]. Some of these methods date back to the time before computers were powerful and available to everyone and have therefore become obsolete. The two numerical methods that have the greatest use since the advent of computers are the finite difference method (FDM) and the finite element method (FEM). The use of FD methods has many advantages, mainly in conceptual simplicity and ease of implementation [139]. FDM can be directly applied to the differential equation by approximating differentials by suitable differential expressions. However, the key drawback of FDM is that the domain under study is partitioned into rectilinear cells. Thus, for many geometries, the boundary conditions must be approximated by a step-like pattern. FEM, on the other hand, does not suffer from such a limitation. With FEM it is possible to model the domain boundaries accurately. The geometry under investigation is divided into a number of simple, non-intersecting elements of variable size. Interesting regions are scaled finer whereas less interesting regions can be resolved coarser to save computation time. Boundaries of these elements can have different shapes and geometries, this allows a very high flexibility. By perpetuating fewer elements, the computation time is reduced, but at a certain point to the detriment of accuracy of results. Therefore, a mesh independence study is essential to estimate the numerical errors in the FEM and, if necessary, to minimize them or to find a trade-off between computation time and numerical accuracy. Due to these advantages, the FEM is used as the method of choice for the analysis of the swirl evaporator.

Since HTCs are to be determined in the steady state, a stationary, i.e. not time-dependent, simulation approach was chosen. From a simulation point of view, this means that no ini-

tial conditions have to be set.

Since HTCs cannot be measured directly, an FEM model of the test carrier was created. In the model, the temperature probes are determined at the same position as the thermocouples in the swirl evaporator housing itself.

With its help, an inverse thermal analysis is performed and the HTCs are determined iteratively. Inverse problems are generally considered as problems of determining a system, for example its structure or its parameters, in terms of its correspondence "input $\rightarrow$ output" [16]. The first publication on inverse heat conduction problems is by Stolz [131] in 1960. In order to trace the heat source or sink in partial differential equations (PDEs) of parabolic type, research has been done on inverse heat source problems since the 1970s [90]. To solve the inverse heat source problem, an ideal situation is usually assumed where the initial condition and boundary conditions are exactly given and an additional set of measured data is added to support the identification work [34, 35, 36, 82, 118]. However, in practice, the above conditions may not all be known because the device is in a hostile environment, so one cannot measure the initial temperature or measurement of boundary data is not possible because it is in an inaccessible part of the boundary. Some researchers also controlled the heat source function for a particular purpose that they wanted to achieve. In this sense, the resulting control problem is an inverse heat source problem to control the heat source to achieve the desired purpose [96, 123].

So in this case the inverse method is used to determine the unknown boundary conditions specified by the HTC α. HTCs are boundary conditions of the 3rd type,

$$-\lambda \frac{\partial T}{\partial n}(x) = \alpha(T(x) - T_\mathrm{f}), \tag{4.13}$$

so called Cauchy boundary conditions [111]. It should be noted that Cauchy boundary conditions merely a correlation between the value and the derivative of the solution and don't specify either one of them for themselves.

To quantify the thermal interaction between the wall temperature of the evaporator housing T and the temperature of the evaporating refrigerant T_f as shown in Figure 4.21, the boundary is used as an control "volume" for energy balance. Since the system is in steady state condition, no energy can be stored in this volume. From this, it can be concluded that all the heat that that enters the surface element (control "volume") from the inside through conduction, has to dissipate outwards through convection.
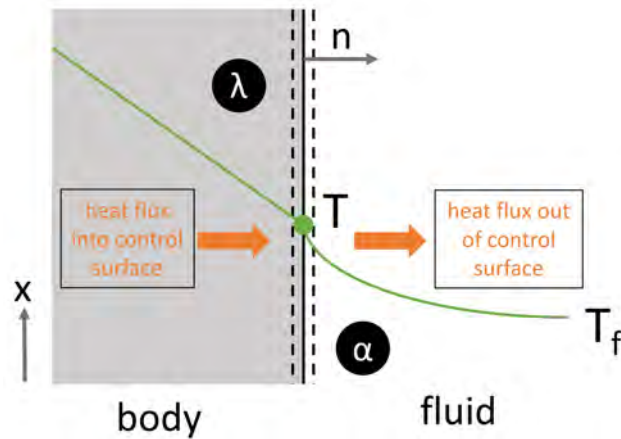
Figure 4.21.: Boundary conditions of the 3rd type (mod. from [111])

In the swirl evaporator body the temperature curve is known hence is measured by the thermocouples $1-5$. Also the evaporation temperature T_f of the fluid can be easily estimated, hence it correlates with the measured evaporation pressure p_o. Also known is the thermal conductivity and the heat input into the system via the heating collar. Figure 4.22 shows the FEM model, which is reduced to the thermally relevant components for computer performance reasons. The model consist of the evaporator housing (copper-colored cylinder) and the heating collar (gray ring). The values obtained and discussed in chapter 4.6 are used as input parameters for the simulation.
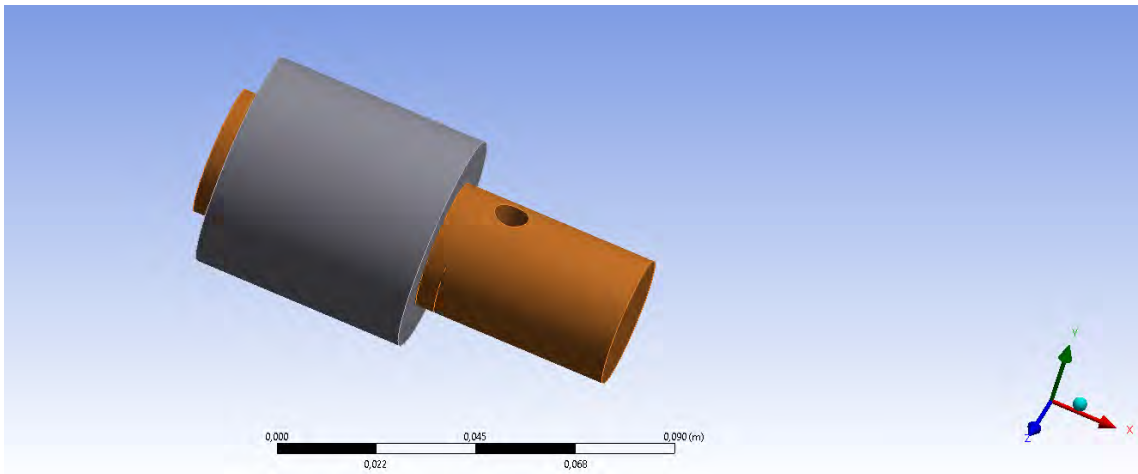
Figure 4.22.: Reduced FEM Model

The heat source is the electrical heater tape with a thermal conductivity of $\lambda_{col} = 30 \, \text{W/m}$ with internal heat generation per unit volume in W/m^3, because an electric current with the power P flowing through the rod. Thermal conductivity of the copper housing is according to DIN 4108 [2] $\lambda_{cop} = 380 \, \text{W/(m K)}$. All outward facing walls are considered as heat sinks to the environment and are assumed to have a HTC for free convection of $\alpha = 7 \, \text{W/(m}^2 \, \text{K)}$ and an air temperature of $22 \, °\text{C}$ (this is also a Cauchy boundary condition). Another constant boundary condition is the part located in the rear part of the housing in which the refrigerant is extracted from the evaporator. The assumption is that the HTC in the extraction region is $\alpha = 6000 \, \text{W/(m}^2 \, \text{K)}$ and the fluid temperature

is a function of the evaporation pressure $T_f = f(p_o)$, which is measured with a pressure sensor. Figure 4.23 shows the top view of the swirl evaporator housing with the position of different temperature probes (or thermocouples) and the inward boundary conditions represented by the extraction region, the swirl region, the pre-swirl region and the region for spray cooling. The swirl region, the pre-swirl region and the region for spray cooling (i.e., all regions except the extraction region), can be combined to a lumped HTC region represented by α_{avg}.
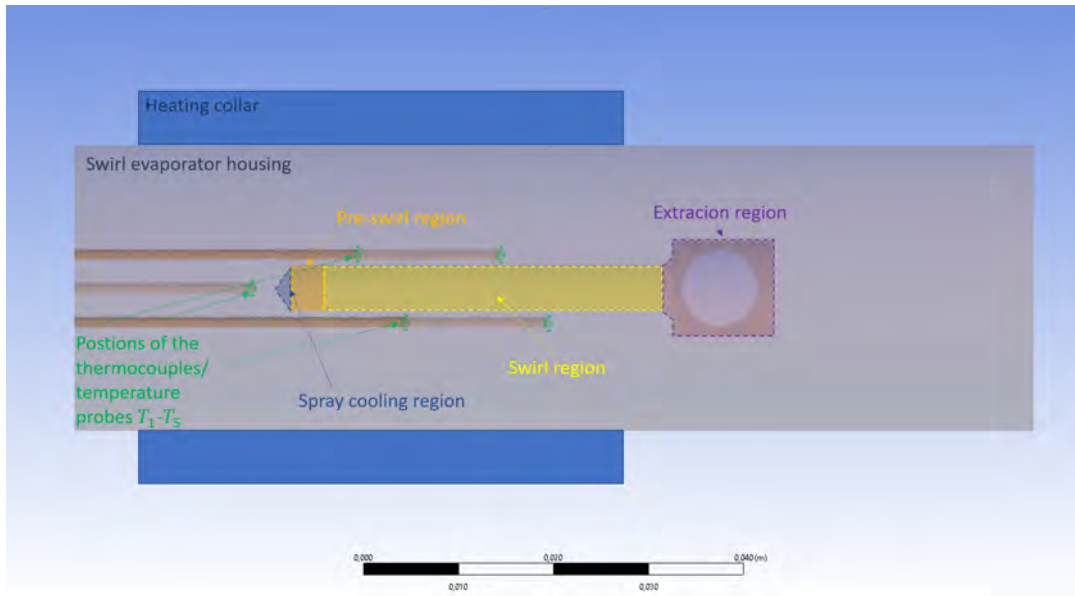
Figure 4.23.: Top view of the semi-transparent swirl evaporator housing

An important factor influencing quality of the FEM calculation is the mesh. If it is too fine, the calculation will take a long time and if it is too coarse, numerical errors will occur. Therefore, a mesh independence study was performed. The mesh consists of 124.723 nodes and 36.930 elements. The diagonal of the space is 0.12329 m, the average area is 6.9587e-004 m² and the minimum edge length is 0.377 mm. The orthogonal quality is a measure of how straight a cell is in relation to the surrounding cells. Or more precisely; how perpendicular the 3 vectors,

- normal vector of the surface

- vector from the center of gravity of the cell to the center of gravity of the surface

- vector between the center of gravity of the cell and the center of gravity of the neighboring cell

are to each other. The orthogonal quality of the mesh has a mean value of 0.654 and a standard deviation of 0.34. This is considered good according to the mesh quality recommendations of Ansys [11].

Skewness is another quality measure of a cell. It is formed by the ratio of the optimal cell size to the actual cell size,

$$\text{Skewness} = \frac{\text{optimal cell size} - \text{cell size}}{\text{optimal cell size}}. \tag{4.14}$$

Skewness of the mesh has a mean value of 0.44151 and a standard deviation of 0.29 which is also considered good according to the Ansys mesh quality recommendations.
Different perspectives of the mesh are shown in Figure 4.24.
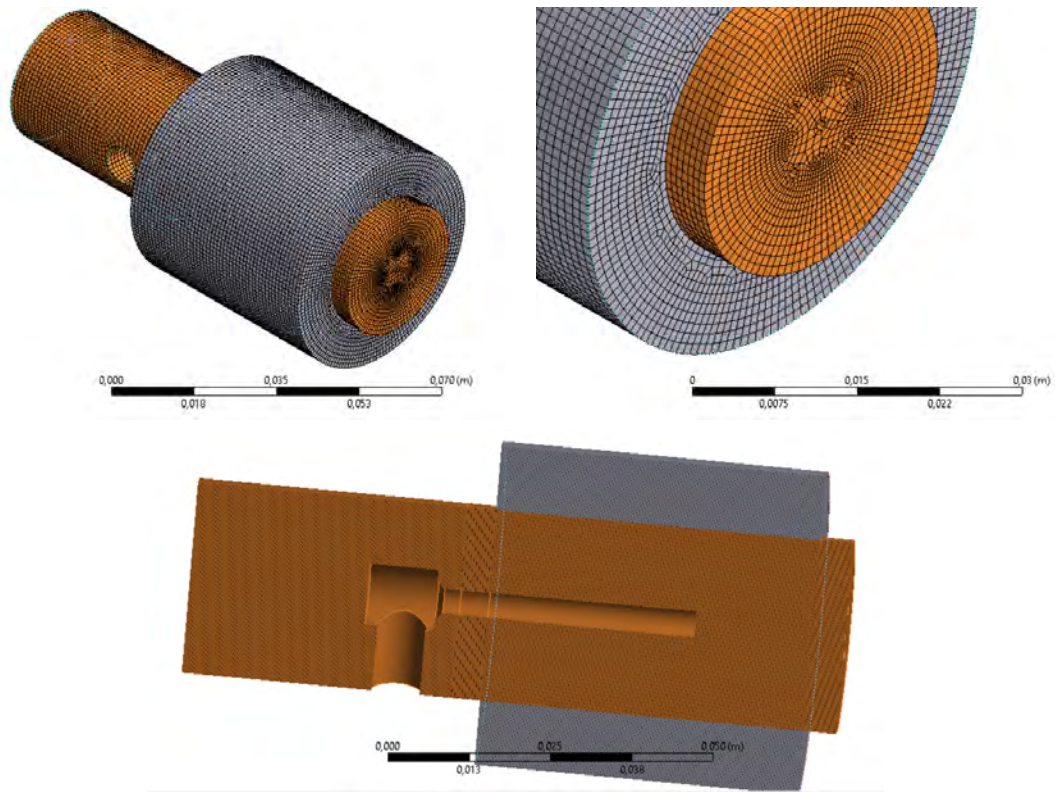
Figure 4.24.: Different perspectives of the mesh

Figure 4.25 shows results of the grid or mesh dependency study. On the abscissa the grid size is given in m. On the ordinate the resulting simulated temperatures are given. A series of simulations were performed in which the only parameter changed was the grid size. The relatively straight temperature lines show that the result almost does not depend on the grid size. Even a very coarse mesh of 2 cm average mesh size gives usable results. Finally, a mesh of 2 mm was used as it gives a good compromise between computation time and accuracy. Looking at the grid in Figure 4.25, the results are only 2.6 % more accurate in case the grid is 4 times finer. However, the calculation time also increases by the Factor of 8^4 (the number of elements to be calculated would be about 4000x as large).
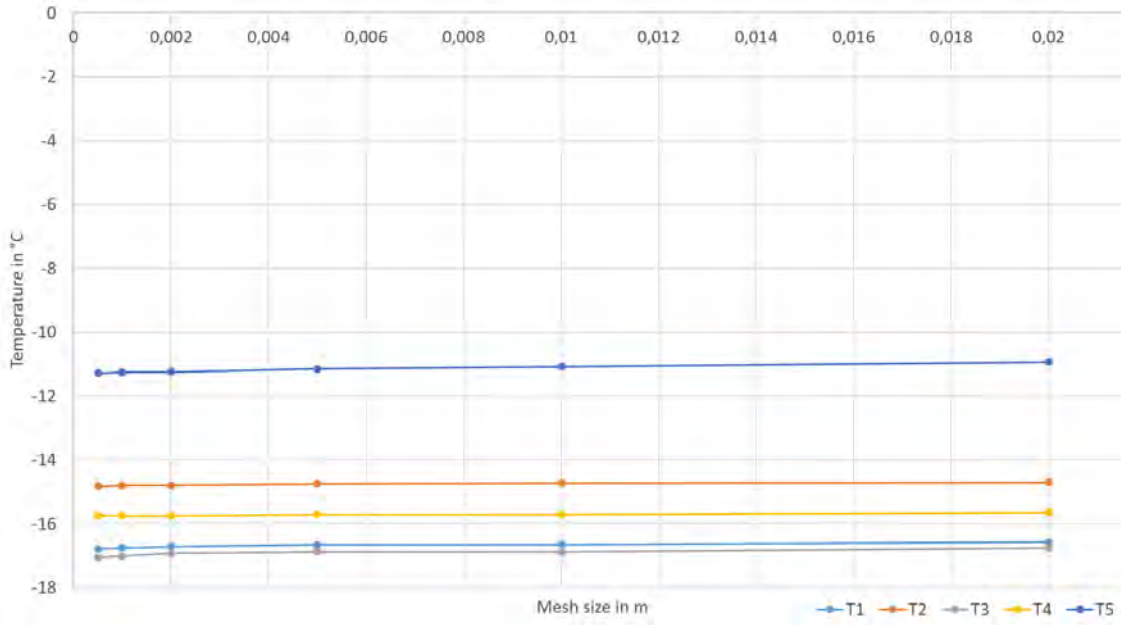
Figure 4.25.: Mesh dependency study

With the help of Richardson extrapolation it is possible to calculate how much more accurate a simulation becomes, i.e. by how much percent the numerical error is reduced if the mesh is further refined. This is interesting because it gives a measure of how much the simulation result depends on the grid size and how much better the numerical computation would be if there were no constraints on computation time and power. The Richardson extrapolation as shown in Equation 4.15 can be applied, given two different discretizations with step sizes h_u and h_g, the numerical solution of a problem involves approximations U_u and U_g for a problem, and these approximations have been computed with a pth-order method [121]. To extrapolate what numerical imprecision could be eliminated if the mesh were resolved twice as finely, one would use $p = 2$. Using Richardson's extrapolation,

$$U_\mathrm{R} = \frac{U_\mathrm{u} - U_\mathrm{g} \left(\frac{h_\mathrm{u}}{h_\mathrm{g}}\right)^p}{1 - \left(\frac{h_\mathrm{u}}{h_\mathrm{g}}\right)^p} = U_\mathrm{g} + \frac{U_\mathrm{u} - U_\mathrm{g}}{1 - \left(\frac{h_\mathrm{u}}{h_\mathrm{g}}\right)^p} \tag{4.15}$$

as shown in Figure 4.26, it can be seen that an infinitely fine mesh would only lead to an improvement of $3.2\,\%$.

Since Cauchy boundary conditions contain neither the value nor the derivative of the value, but only the relationship between the two, Cauchy boundary conditions cannot be rearranged to obtain the value. Therefore, as usual in an inverse approach, the ratios of input to output are determined. To determine a HTC for one measurement and one thermal load (or electrical power), a set of different HTCs α_avg are simulated as input parameters while keeping all other boundary conditions constant. The determined output parameters would be the resulting temperature field shown in Figure 4.27 or the simulated temperatures $T_{1;\,\mathrm{sim}}$–$T_{5;\,\mathrm{sim}}$ at the green marked locations in Figure 4.23.

Input: $\alpha_\mathrm{avg} \Longrightarrow$ Output: $T_{1;\,\mathrm{sim}}$–$T_{5;\,\mathrm{sim}}$.

In the example shown in Table 4.10, α_avg is increased in steps of $2000\,\mathrm{W/(m^2\,K)}$ from
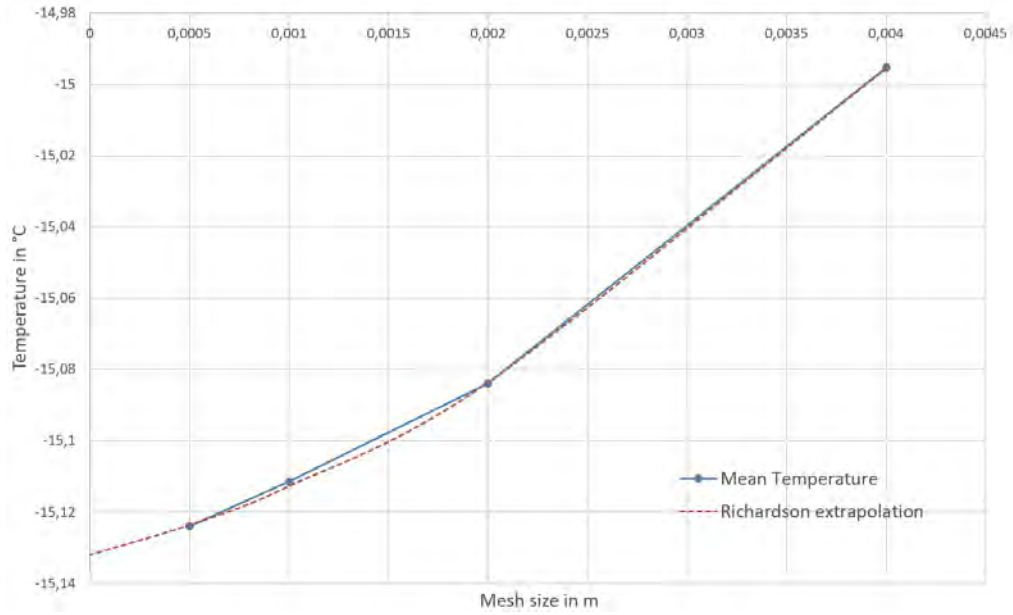
Figure 4.26.: Richardson extrapolation
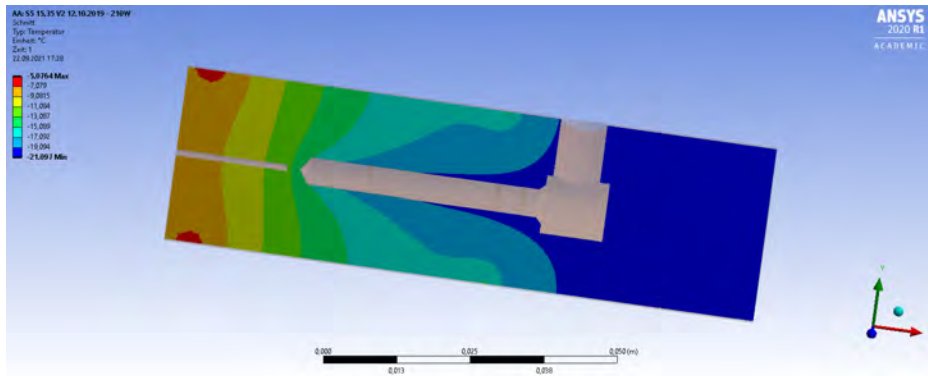
Figure 4.27.: Cross-section of the reduced FEM Ansys model with isotherms

$2000\,\mathrm{W/(m^2\,K)}$ to $40000\,\mathrm{W/(m^2\,K)}$. This results in the corresponding temperatures $T_{1;\,\mathrm{sim}}$–$T_{5;\,\mathrm{sim}}$.

In order to determine the HTC α_{avg} in the system, the simulated temperatures are now compared with the measured temperatures $T_{1;\,\mathrm{mea}}$–$T_{5;\,\mathrm{mea}}$ from the experiment. In this example the measured temperatures are:

$T_{1;\,\mathrm{mea}}{=}{-}14.43\,\mathrm{°C}$ $\quad T_{2;\,\mathrm{mea}}{=}{-}11.75\,\mathrm{°C}$ $\quad T_{3;\,\mathrm{mea}}{=}{-}15.62\,\mathrm{°C}$
$T_{4;\,\mathrm{mea}}{=}{-}13.07\,\mathrm{°C}$ $\quad T_{5;\,\mathrm{mea}}{=}{-}8.83\,\mathrm{°C}$

The next step is to determine the deviation between simulated and measured results. This deviation is also referred to as error e and is the deviation between the previous total and the measured value. This is squared and then the root is taken to balance the influence of positive and negative results,

$$e = \sqrt{(\mathrm{Measurement} - \mathrm{Prediction})^2}. \tag{4.16}$$

Table 4.10.: Simulated temperatures for a set of different α_{avg} and $P = 220\,\text{W}$

Input	Output				
α_{avg} in $\text{W}/(\text{m}^2\,\text{K})$	$T_{1;\,\text{sim}}$ in °C	$T_{2;\,\text{sim}}$ in °C	$T_{3;\,\text{sim}}$ in °C	$T_{4;\,\text{sim}}$ in °C	$T_{5;\,\text{sim}}$ in °C
2000	23.26	27.95	21.51	26.34	31.83
4000	12.89	16.81	11.59	15.37	20.63
8000	1.65	4.72	0.84	3.48	8.45
12000	−4.32	−1.72	−4.88	−2.85	1.94
16000	−8.02	−5.73	−8.42	−6.78	−2.11
20000	−10.54	−8.46	−10.83	−9.45	−4.89
24000	−12.36	−10.45	−12.58	−11.39	−6.91
28000	−13.74	−11.96	−13.90	−12.86	−8.46
32000	−14.82	−13.14	−14.93	−14.02	−9.67
36000	−15.69	−14.10	−15.76	−14.94	−10.66
40000	−16.40	−14.88	−16.45	−15.71	−11.47

The total error e_{total} is then determined by adding up the individual errors e_i,

$$e_{\text{total}} := \sum_{i=1}^{n=5} \sqrt{(T_{i;\,\text{mea}} - T_{i;\,\text{sim}})^2} = \sqrt{(T_{\text{mea};\,1} - T_{\text{sim};\,1})^2} + ... + \sqrt{(T_{\text{mea};\,5} - T_{\text{sim};\,5})^2}. \quad (4.17)$$

Table 4.11 shows the temperatures determined for a range of different HTCs. It can be seen, that the error sum for a certain HTC assumes a minimum value. This value is marked red in this table. This value represents the HTC prevailing in the system.

Table 4.11.: Residuals of the temperatures for a set of different α_{avg} and $P = 220\,\text{W}$

Input	Output					
α_{avg} in $\text{W}/(\text{m}^2\,\text{K})$	e_1 in K	e_2 in K	e_3 in K	e_4 in K	e_5 in K	e_{total} in K
2000	37.69	39.70	37.13	39.41	40.66	194.59
4000	27.32	28.56	27.21	28.44	29.45	140.98
8000	16.08	16.47	16.45	16.55	17.28	82.83
12000	10.11	10.03	10.74	10.22	10.77	51.87
16000	6.41	6.02	7.19	6.30	6.71	32.63
20000	3.89	3.29	4.78	3.62	3.94	19.52
24000	2.07	1.30	3.04	1.68	1.91	10.00
28000	0.69	0.21	1.72	0.21	0.37	3.20
32000	0.39	1.39	0.68	0.94	0.84	4.26
36000	1.26	2.35	0.15	1.87	1.83	7.46
40000	1.97	3.14	0.83	2.64	2.64	11.22

It can be seen that the error for a certain HTC reaches a minimum. To illustrate this graphically, a finer resolution simulation was performed for the same measurement as shown in Figure 4.28. Instead of steps of $2000\,\text{W}/(\text{m}^2\,\text{K})$, α was increased in steps of 500 from 2000 to $85000\,\text{W}/(\text{m}^2\,\text{K})$. This makes the curve look smoother, the error is minimized even further and α can be determined more accurately.
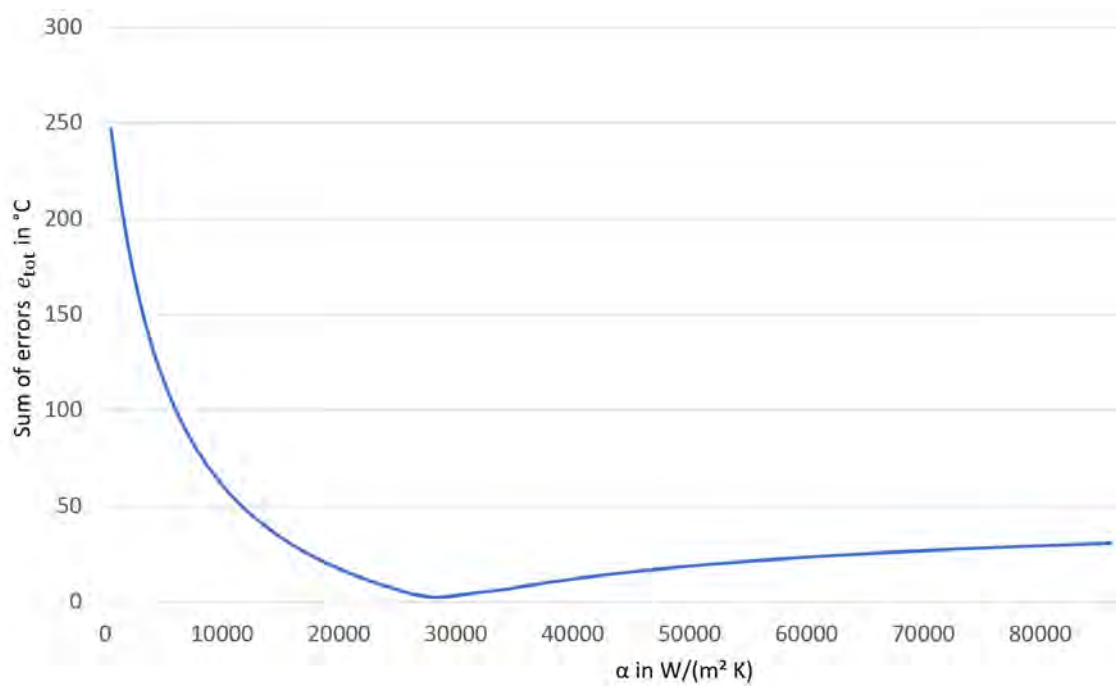
Figure 4.28.: Errors show a minimum at the specific heat transfer coefficient

5. Results and Discussion

In this Chapter, the experimentally determined results of Chapter 4 are compared with the simulated results of Chapter 3. In this way, the individual models for heat transfer, pressure loss and CHF can be verified. Since the CHF model is based on an experimental data look-up table, the model can be assumed to have a certain reliability even beyond limits of the parameters investigated in this thesis, which is why it was used here to gain insights that could not be investigated due to physical limitations of the experimental setup. At the end of the Chapter, the concept of an optimized swirl geometry is critically reviewed and discussed.

5.1. Verification of the HTC Model

In this section, the experimentally determined HTCs are compared with the HTCs from the correlations presented in Chapter 3. Table B.1 in the Appendix shows the tests performed to verify the HTC correlations.
Figures 5.1–5.5 show measurements and simulated values of the respective correlations. The measured HTCs are shown as orange dots and the simulated values as a black line. The gray band in this case represents the 30 % error band. The mean absolute error (MAE),

$$\text{MAE} = \frac{1}{N} \sum^{N} \frac{abs(\text{Pred} - \text{Meas})}{\text{Meas}} \cdot 100\% \tag{5.1}$$

mean error (ME)

$$\text{ME} = \frac{1}{N} \sum^{N} \frac{\text{Pred} - \text{Meas}}{\text{Meas}} \cdot 100\% \tag{5.2}$$

and deviation (Dev.),

$$\text{Dev.} = \sqrt{\frac{1}{N} \sum^{N} \left(\frac{\text{Pred} - \text{Meas}}{\text{Meas}} \right)^2} \cdot 100\,\%, \tag{5.3}$$

as defined in Equation 5.1–5.3, are used to measure the fitness of the HTC correlations.

Shah

The 1982 Shah correlation has an MAE of 34.19 and a Dev of 36.51. The ME is -25.31 which means that the correlation predicts on average a too small HTC. 66.97 % of the predicted values are outside the 30 % error band. It is noticeable that starting from a pitch of ≥ 5 the correlation only under-predicts the experimentally measured value. The rather sudden change is due to the nature of Equation 3.48 described in Chapter 3. Due to its comparatively large deviations, the Shah correlation, which is displayed in Figure 5.1, is considered rather unsuitable for a determination of the heat transfer in the swirl.
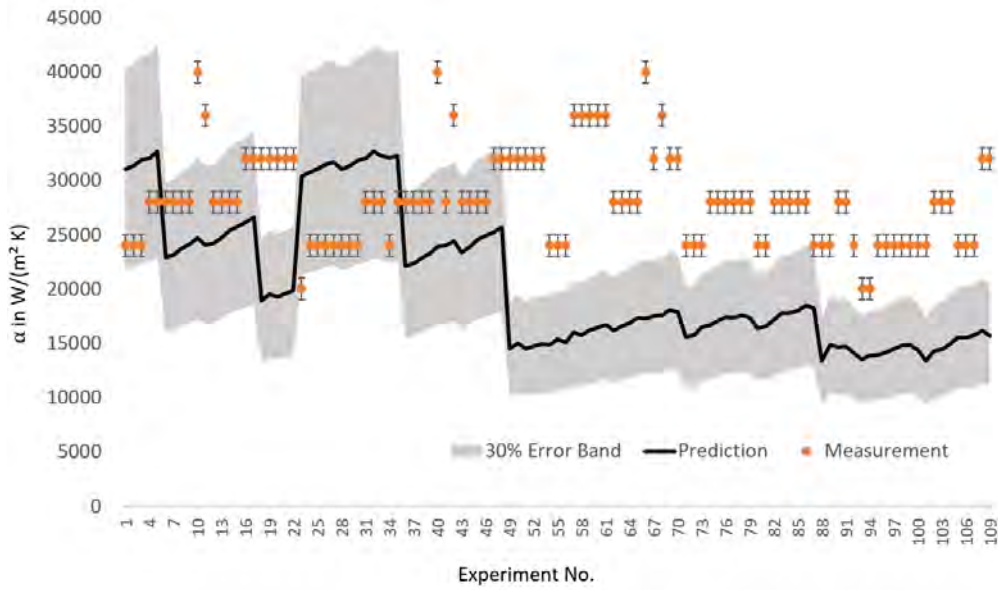
Figure 5.1.: Predicted and measured HTC using the Shah correlation

Kew-Cornwall

The correlation developed by Kew and Cornwell has a MAE of 26.87 and a ME of 25.48. It's deviation is 30.16 and 7.34 % of the predicted values are outside of the 30 % error bar. The predicted and measured HTCs are shown in Figure 5.2.
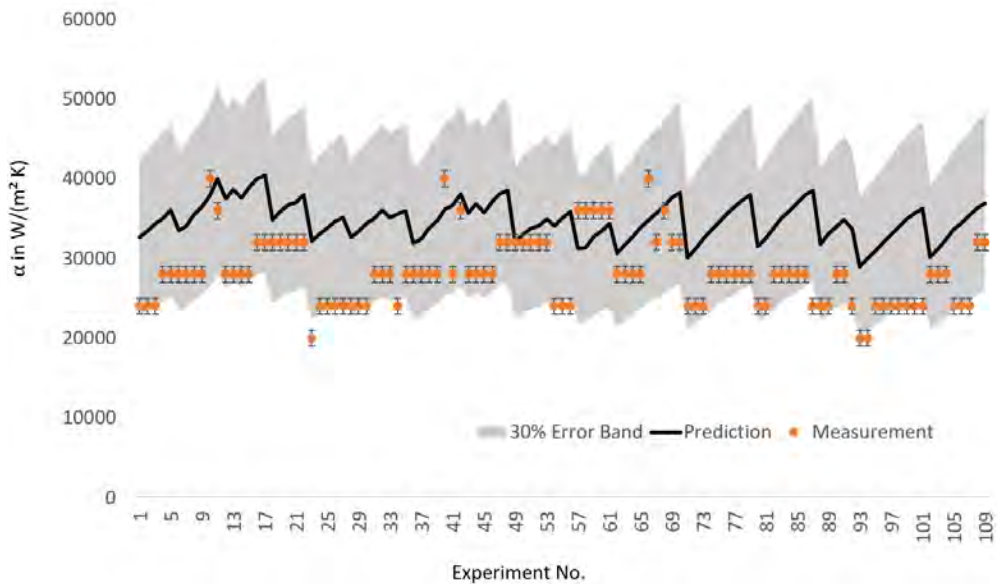
Figure 5.2.: Predicted and measured HTC using the Kew-Cornwall correlation

Gungor-Winterton

As it can be seen in Figure 5.3, the Gungor-Winterton correlation over-predicts the simulated values with an ME of 60.96. Since all simulated values are above the measured

values, the MAE is equal to the ME. The deviation is 68.41. 66.97 % of the values are outside of the 30 % error band.
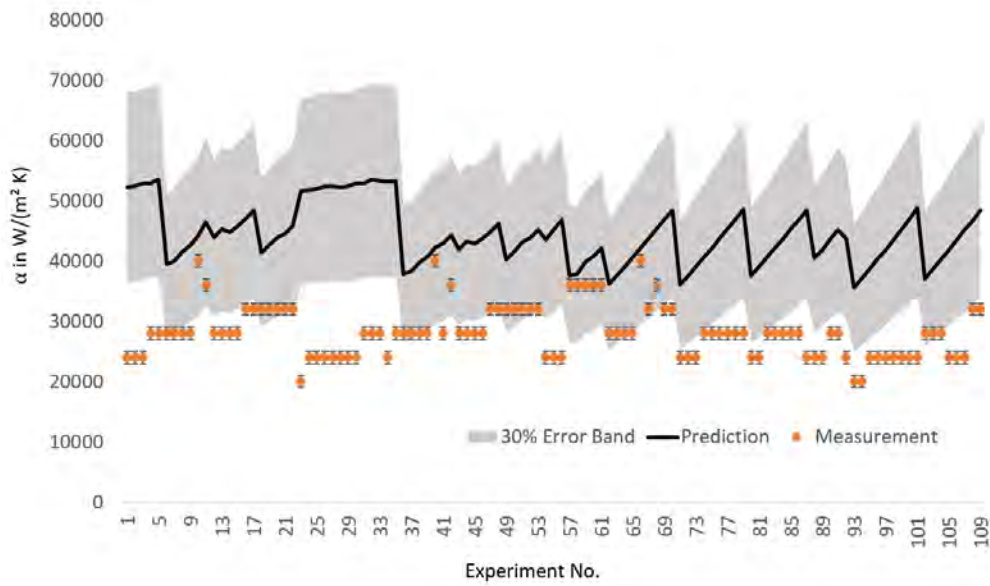
Figure 5.3.: Predicted and measured HTCs using the Gungor-Winterton correlation

Lazarek-Black

With a MAE of 23.44, a ME of 21.54 and a Dev. of 26.61 the Lazarek-Black correlation, which is displayed in Figure 5.4, seems to be one of the more appropriate correlations for predicting the heat transfer in the swirl. Only 0.92 % of the predicted values are outside the 30 % error bar.
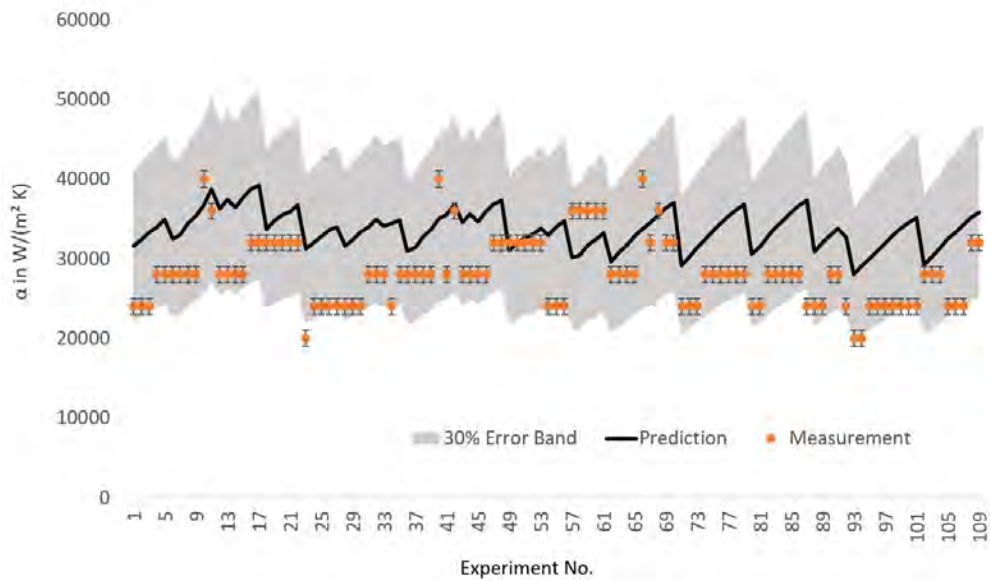
Figure 5.4.: Predicted and measured HTCs using the Lazarek-Black correlation

Sun-Mishima

The best fit between the measured and simulated values is obtained with the Sun model. The MAE is 12.62, the ME is 5.56 and the Dev is 15.32. 5.50 % of the simulated values are outside the 30 % error bar. The predicted and measured HTCs using the Sun-Mishima correlation are shown in Figure 5.5. To a similar conclusion came Li and Hrnjak [87] when they where evaluating HTCs for micro-channel heat exchangers and of course Sun and Mishima themselves when they evaluated prediction methods for HTCs in mini-channels [132].
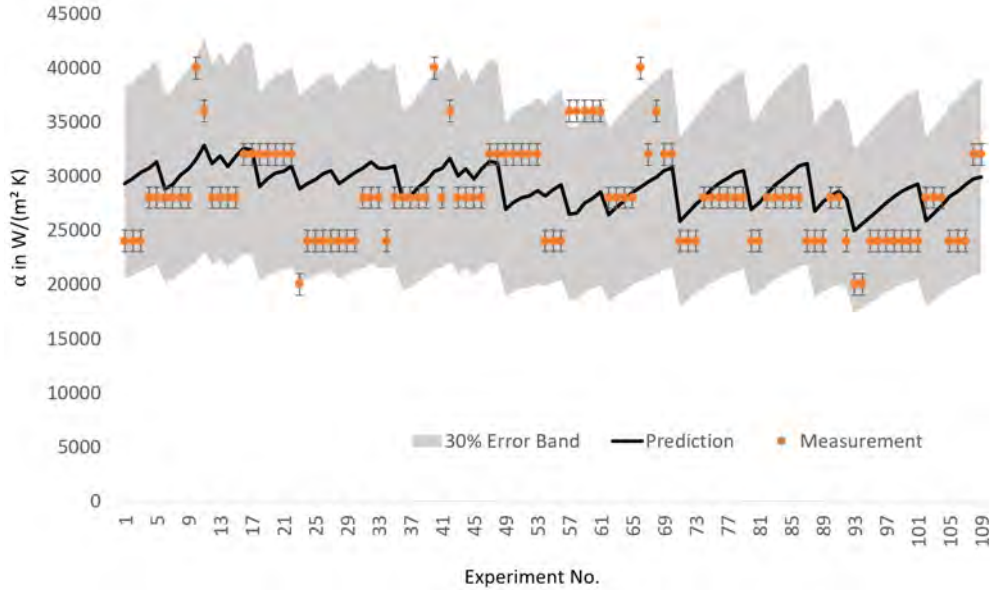
Figure 5.5.: Predicted and measured HTCs using the Sun-Mishima correlation

For a better overview the MAE, ME, Dev. and values outside the 30 % error band of all investigated HTC-correlations are shown in Table 5.1.

Table 5.1.: Summary of HTC-correlation results

Correlation	MAE	ME	Dev.	Outside 30 %-band
Shah	34.19	−25.31	36.51	66.97 %
Kew-Cornwall	26.87	25.48	30.16	7.34 %
Gungor-Winterton	60.96	60.96	68.41	66.97 %
Lazarek-Black	23.44	21.54	26.61	0.92 %
Sun-Mishima	12.62	5.56	15.32	5.50 %

5.2. Experimental Validation of Pressure Drop/Mass Flow Model

To validate the simulation model presented in Chapter 3, the group A experiments presented in Chapter 4 were conducted. Tests were carried out with different screw engagement lengths as shown in Figure 5.6. A screw engagement length of 40 mm means that the screw is in full engagement (Figure 5.6 a). A screw engagement length of 0, which is shown in Figure 5.6 c, means that there is no screw in the evaporator.

Figure 5.6.: Various penetration depths of the screw [47]

This corresponds to a spot evaporator. Since the mass flow and the pressure drop are connected via Bernoulli's principle and the continuity equation (as described in Chapter 2), the model can calculate either the pressure drop with a given mass flow **or** the mass flow with a given pressure drop. Bernoulli's equation is shown here as a pressure equation by multiplication with ϱ [21],

$$\frac{c_1^2 \cdot \varrho_1}{2} + \varrho_1 \cdot g \cdot z_1 + p_1 = \frac{c_2^2 \cdot \varrho_2}{2} + \varrho_2 \cdot g \cdot z_2 + p_2 \tag{5.4}$$

and the continuity equation,

$$\dot{m} = \varrho \cdot c \cdot A = \text{const.}. \tag{5.5}$$

To verify simulation results of the pressure loss model described in Chapter 3, a series of measurements were performed on the test stand described in Chapter 4. The tests were performed with different screw engagement lengths under steady-state conditions in a controlled and air-conditioned environment. Each test was repeated at least 3 times. The point corresponds to the arithmetic mean of the series of measurements of one screw engagement length and the error bar corresponds to one standard deviation. Since the screw engagement lengths in the experiment are subject to a certain measurement uncertainty, which does not occur in the simulation, error bars are entered on the abscissa only for the experimental results. Overall, results obtained in the test show satisfactory agreement with the calculated values. For penetration depths below 25 mm, the simulation underestimates the actual pressure drop, and for a penetration depth of 40 mm, the simulation overestimates the measured pressure drop, as can be seen in Figure 5.7.
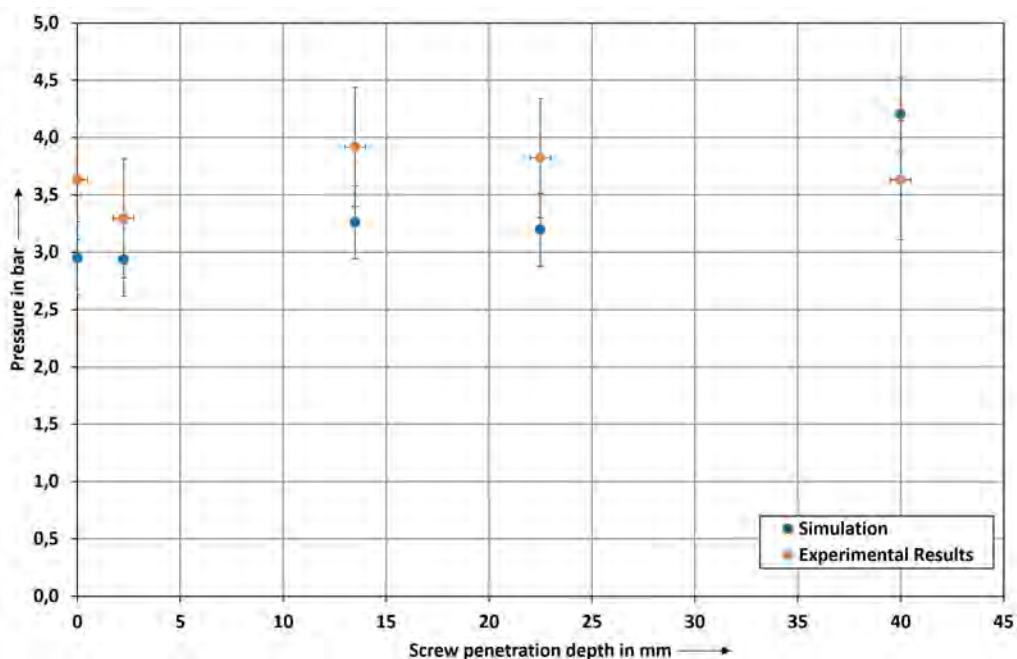
Figure 5.7.: Measured and predicted pressure loss for various screw engagement lengths

For the mass flow, it is consequently the other way round. For penetration depths smaller than 25 mm, the simulation seems to overestimate the mass flow, and for a penetration depth of 40 mm, the simulation underestimates the measured values. This relationship is shown in Figure 5.8. This reversal could be caused by a change in flow pattern caused by the longer swirl length.
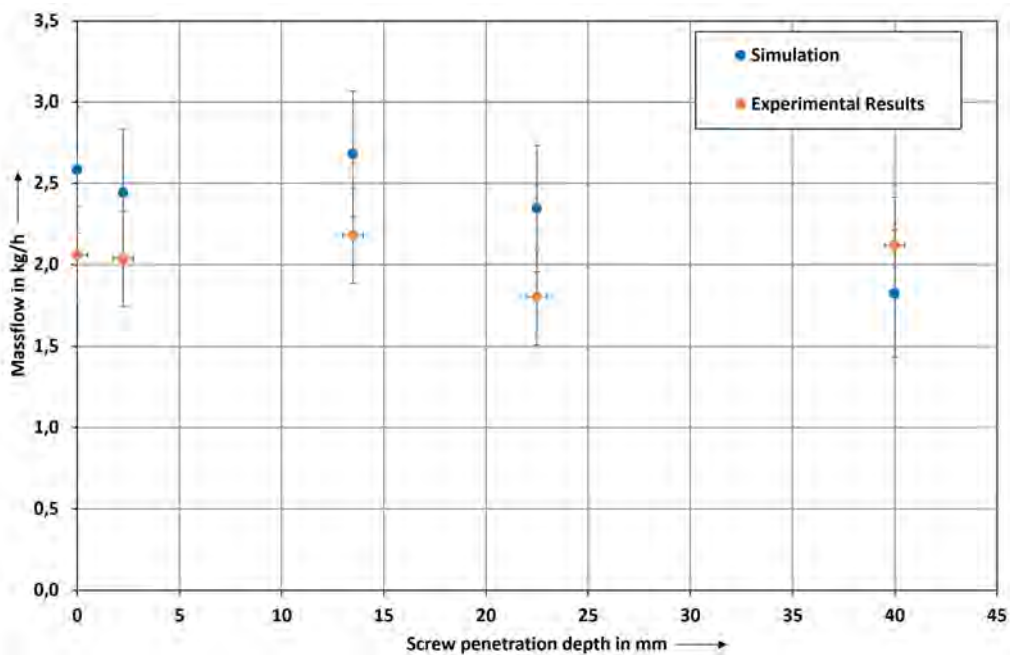
Figure 5.8.: Measured and predicted mass flow for various screw engagement lengths

5.3. Verification of the CHF Model

Table 5.2 lists the tests for which the simulation was compared with the measured values. As can be seen in Figure 5.9, the measured values correlate reasonably well with an MAE of 8.51, a ME of -4.71 and a Dev of 8.77. 96.8 % of the simulated values are located within an error band of 15 %.

Table 5.2.: Test runs for CHF

Test run No.	d_{hyd} in mm	$\dot{m}$ in kg/h	p_{o} in bar	$\dot{Q}_{\mathrm{crit;\,mea}}$ in W	$\mathrm{CHF}_{\mathrm{sim}}$ in kW/m^2	$\mathrm{CHF}_{\mathrm{mea}}$ in kW/m^2
1	0.84	3.12	3.37	260	335.16	368.01
2	0.84	2.99	3.25	254	327.16	360.76
3	0.84	3.12	3.37	260	335.17	368.01
4	0.84	2.98	3.18	265	327.10	375.09
5	1.00	3.20	2.00	265	372.10	375.09
6	1.00	3.25	2.00	272	375.43	384.99
7	1.00	2.85	1.90	270	348.13	382.17
8	1.00	2.67	1.80	263	341.74	372.26
9	1.00	2.97	1.80	265	357.74	375.09
10	1.27	3.05	3.26	249	387.18	352.44
11	1.27	3.22	3.17	259	405.71	367.65
12	1.27	3.13	3.35	240	395.09	339.70
13	1.27	3.05	3.28	237	387.20	336.69
14	1.27	3.22	3.17	259	405.71	367.65
15	1.49	3.01	3.22	241	387.06	341.47
16	1.59	3.00	2.00	263	402.39	372.25
17	1.59	2.99	2.00	253	402.39	358.11
18	1.64	3.04	3.21	260	394.36	368.01
19	1.64	2.96	3.17	260	385.35	368.01
20	1.64	3.12	3.33	260	401.87	368.01
21	1.69	3.00	1.95	265	403.99	375.08
22	1.69	3.02	1.95	257	403.99	363.76
23	1.69	2.98	1.95	250	403.99	353.85
24	1.78	3.02	1.95	280	404.57	396.32
25	1.78	3.00	1.95	263	404.57	372.25
26	1.81	2.99	3.20	250	391.04	353.85
27	1.81	3.03	3.23	250	395.35	354.03
28	1.81	2.98	3.19	250	389.98	353.85
29	1.81	3.11	3.33	260	403.24	368.01
30	4.50	3.20	1.90	263	393.11	372.25
31	4.50	2.92	1.90	250	359.76	353.85
32	4.50	2.88	1.87	245	354.91	346.78

Figure 5.9.: Comparison of the measured and simulated CHF

5.4. Interpretation of the CHF Model

Since the CHF model developed in this work is based on an experimental data lookup table, it can be assumed that the model has some reliability beyond the limits of the parameters studied in this work. Therefore, the model was u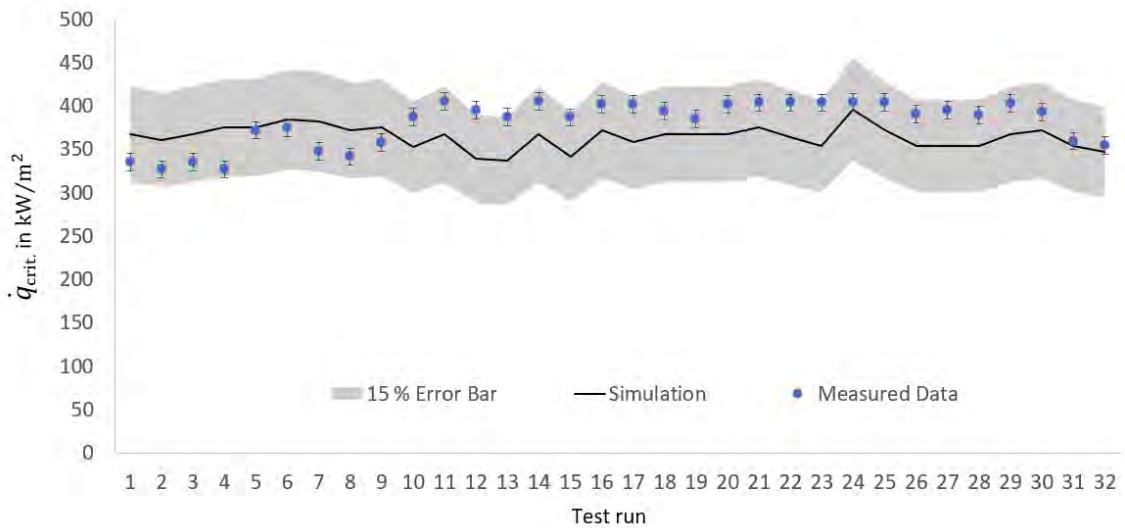sed here to gain insights that could not be investigated due to the physical limitations of the experimental setup. In this way, new insights into the system behavior are to be gained. To conclude, the simulated results are compared to experimental investigations on CHF during flow boiling of other researchers. All 3 Figures 5.10–5.12 show that the CHF increases with mass flow (and also mass flux), a phenomenon which is also well known in the literature [95, 115, 116, 5, 6].

Figure 5.10 shows the influence of d_{hyd} on CHF for various mass flows. At higher mass flows there seems to be a clear optimum of the hydraulic diameter whereas at lower mass flows the curve is rather flat. At the mass flow curve of $6\,\mathrm{kg/h}$ a clear optimum is visible for a d_{hyd} of $2.6\,\mathrm{mm}$. This also means that at higher mass flows, the correct design of the proper hydraulic diameter becomes more and more important.

Among the various geometrical parameters, the hydraulic diameter and the length/diameter ratio have a great influence on CHF. In subcooled boiling, CHF increases as the channel diameter decreases. This tendency has been consistently observed by a number of researchers [137, 17]. On the other hand, for $x_{\mathrm{eq}} > 0$, CHF also decreases with the decrease in diameter. Bergles [17] postulated that as the channel diameter decreases, the exit diameter of the vapor bubbles also decreases. In addition, the condensation at the tip of the bubble increases and the bubble velocity relative to the liquid decreases. A combination of these effects results in the curve visible in Figure 5.10.

The influence of inlet vapor quality x_{in} on CHF, as displayed in Figure 5.11, is of a more trivial nature. The higher x_{in}, the less the difference up to the critical vapor content x_{crit}. As soon as the liquid film thickness reaches a minimum, CHF occurs [61, 84].

Figure 5.12 shows the influence of the evaporation pressure on CHF. It can be seen that with increasing evaporation pressure, the CHF achievable in the swirl evaporator decreases. The course of the curves is the result of two opposite effects. By increasing the pressure, the CHF is increased [54]. However, increasing the pressure also decreases the enthalpy of evaporation. Since the enthalpy of evaporation decreases in a larger ratio than the CHF
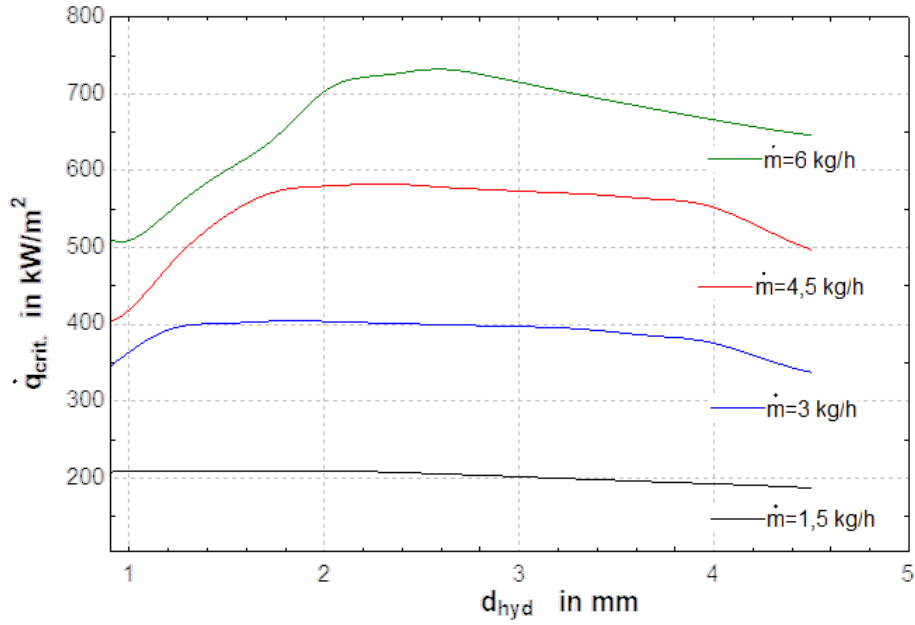
Figure 5.10.: Influence of d_{hyd} on CHF
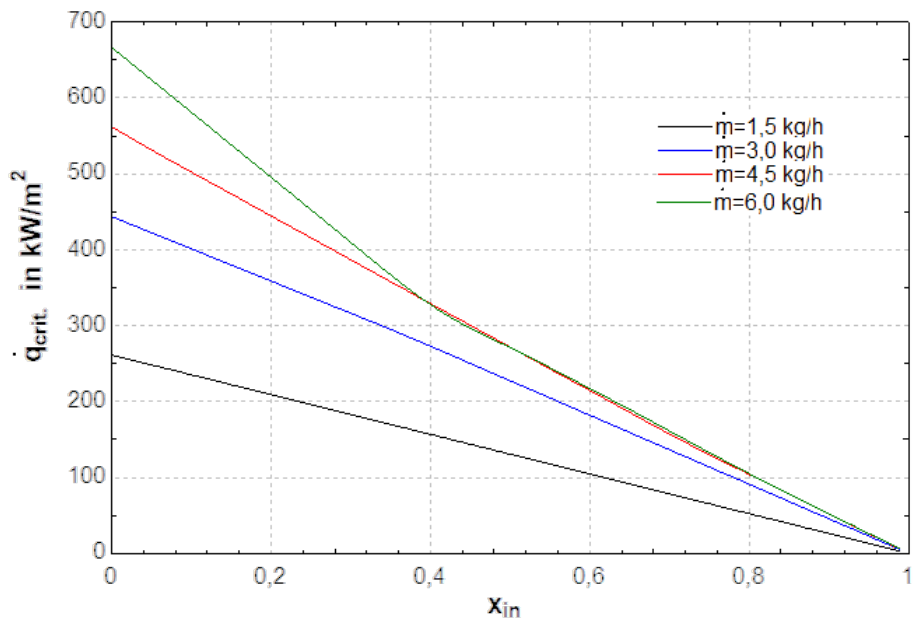
Figure 5.11.: Influence of inlet vapor content on CHF

increases, the critical vapor content is achieved by lower power absorption. Mauro et al. were able to observe a similar effect [95].
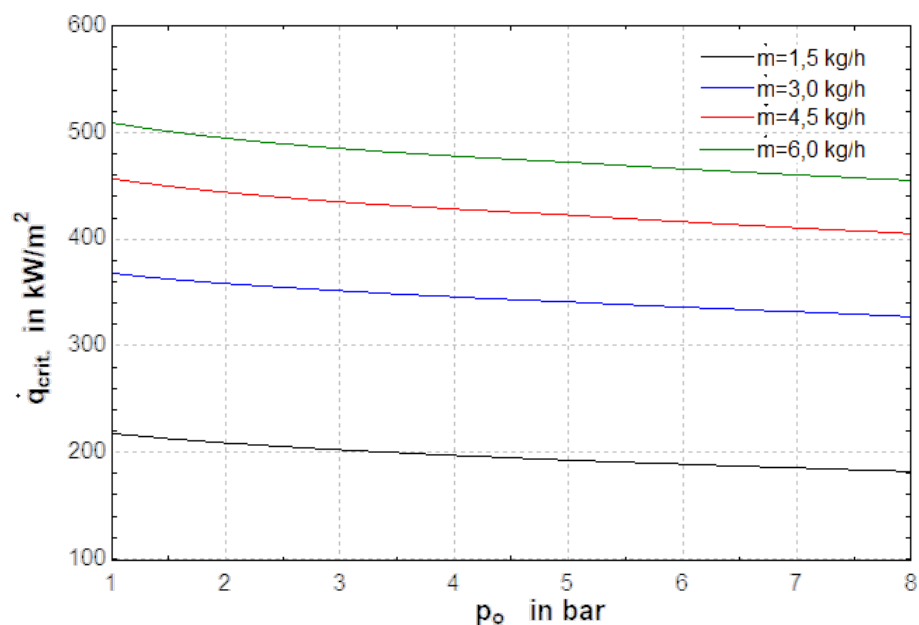
Figure 5.12.: Influence of the evaporation pressure on CHF

5.5. Experimental Investigation of the Optimal Pitch

If the HTC is plotted against the pitch of the individual swirls, it is noticeable that there is a pitch at which the HTC assumes a maximum value. The respective mass flow is plotted on the second ordinate. For 220 W to 250 W, a pitch of 5 mm appears to have the highest HTC. These are shown in Figure 5.13 to 5.16. Above a heat load of 260 W the optimum value shifts to a pitch of 3 mm.
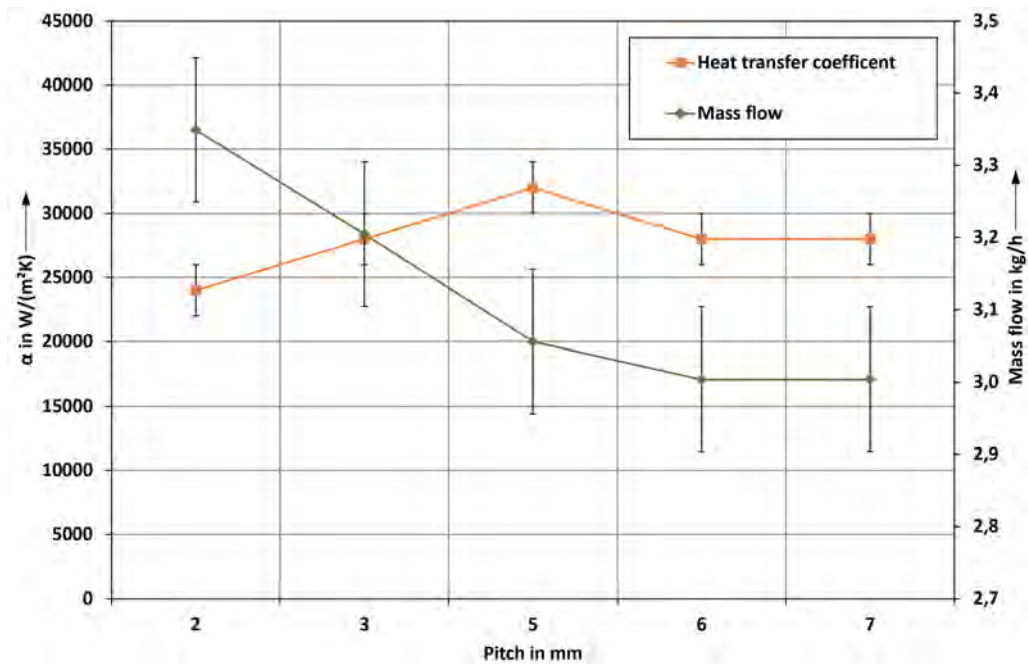
Figure 5.13.: Heat transfer coefficient and mass flow as a function of the pitch at 220 W
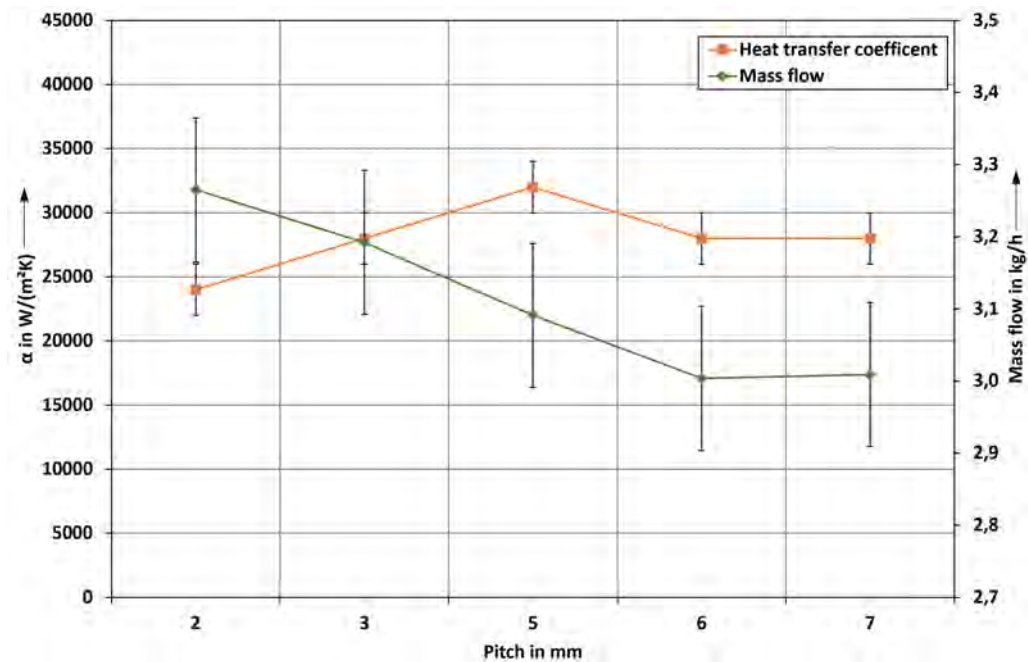
Figure 5.14.: Heat transfer coefficient and mass flow as a function of the pitch at 230 W
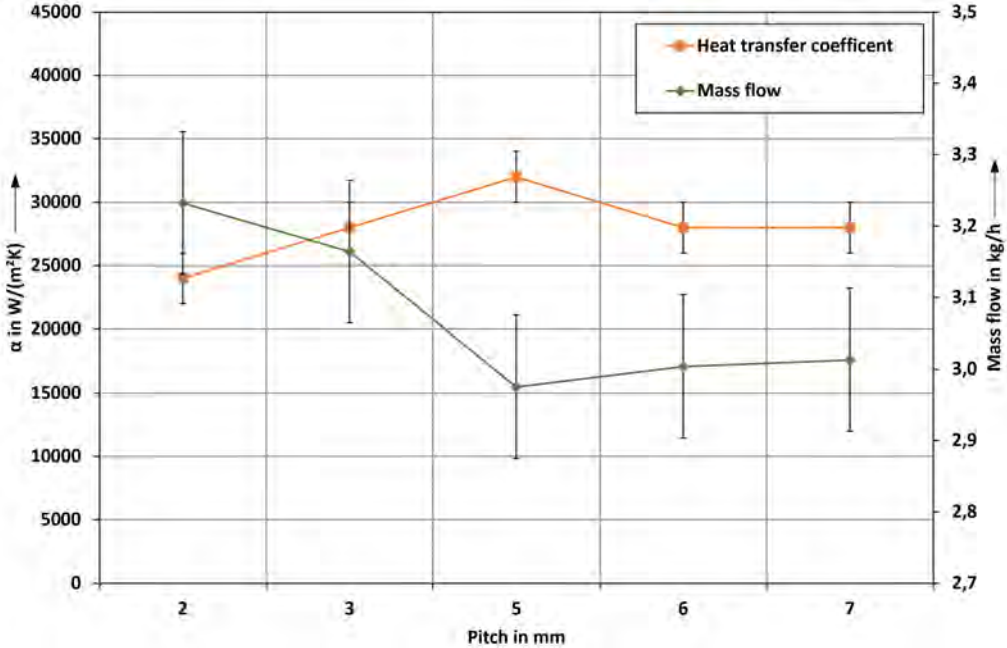
Figure 5.15.: Heat transfer coefficient and mass flow as a function of the pitch at 240 W
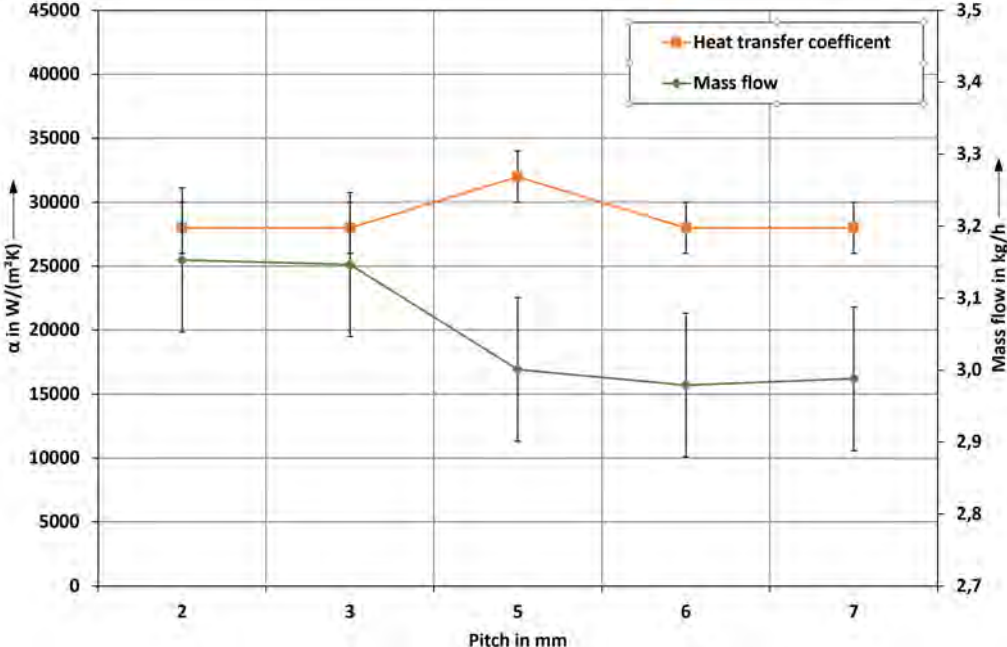
Figure 5.16.: Heat transfer coefficient and mass flow as a function of the pitch at 250 W
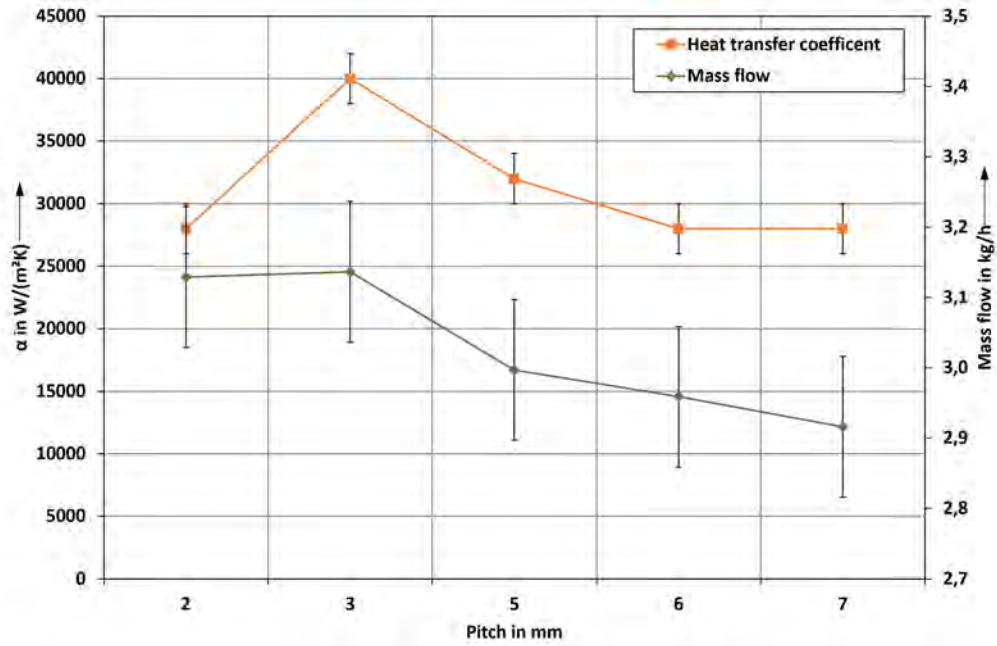
Figure 5.17.: Heat transfer coefficient and mass flow as a function of the pitch at 260 W

Mass flow appears to decrease slightly with increasing power. In addition, the mass flow seems to decrease with increasing pitch. The pressure drop shown in Figure 5.18 to Figure 5.22 behaves inversely to the mass flow. As the gradient increases, the pressure drop also increases. In addition, the pressure drop increases with increasing gradient.
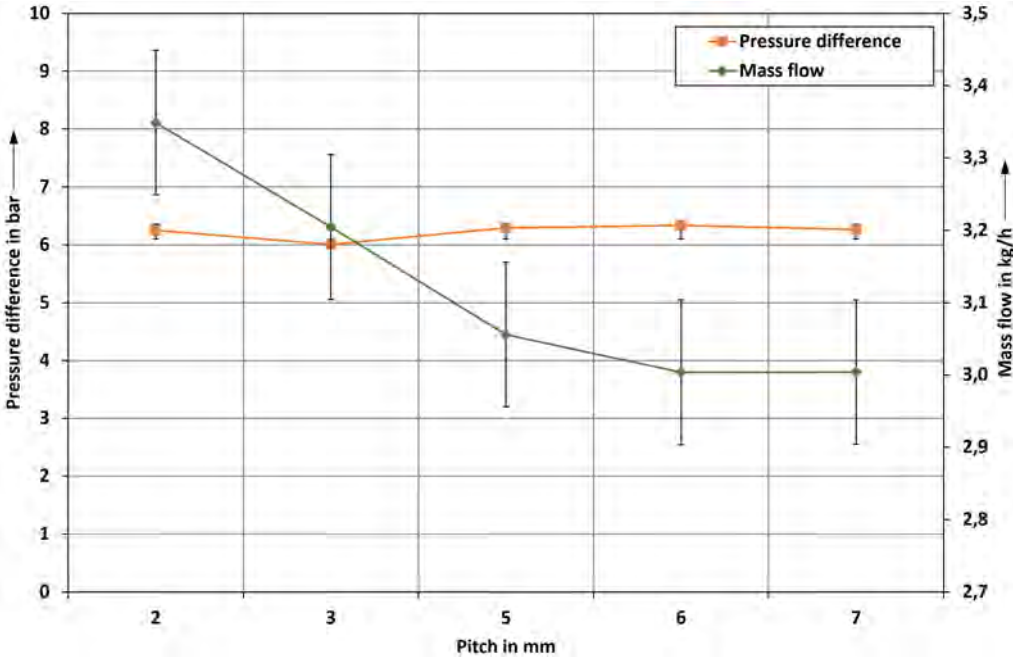
Figure 5.18.: Pressure difference and mass flow as a function of the pitch at 220 W
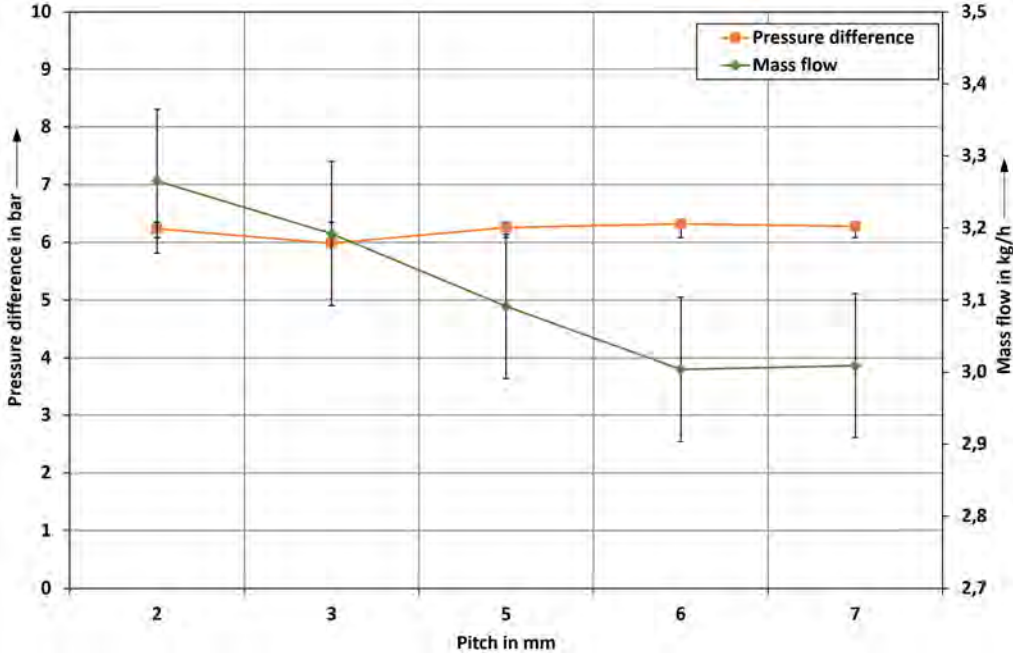
Figure 5.19.: Pressure difference and mass flow as a function of the pitch at 230 W
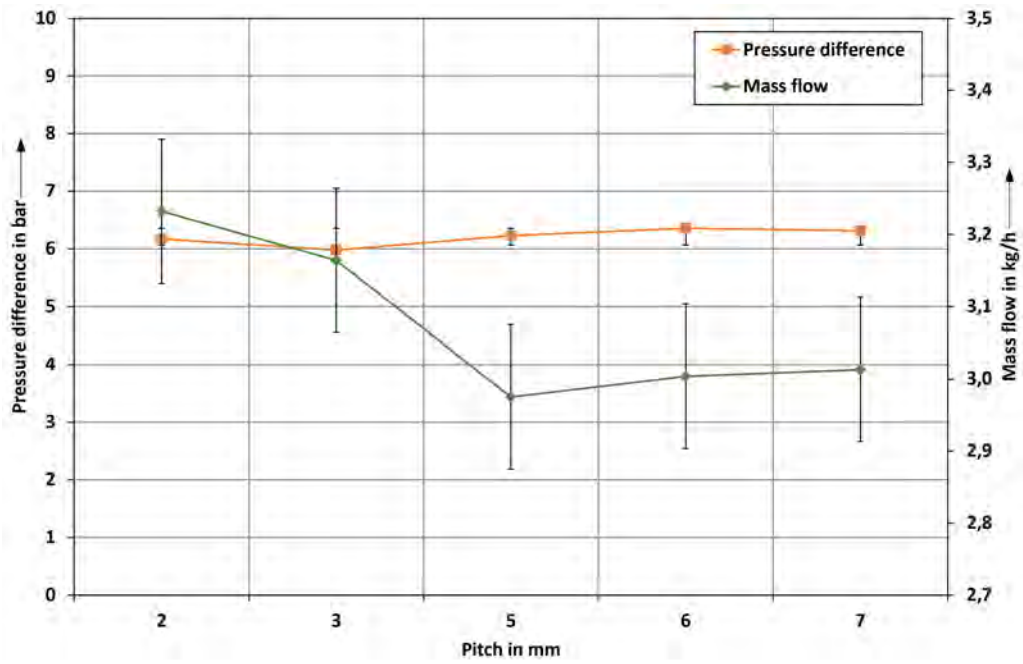
Figure 5.20.: Pressure difference and mass flow as a function of the pitch at 240 W
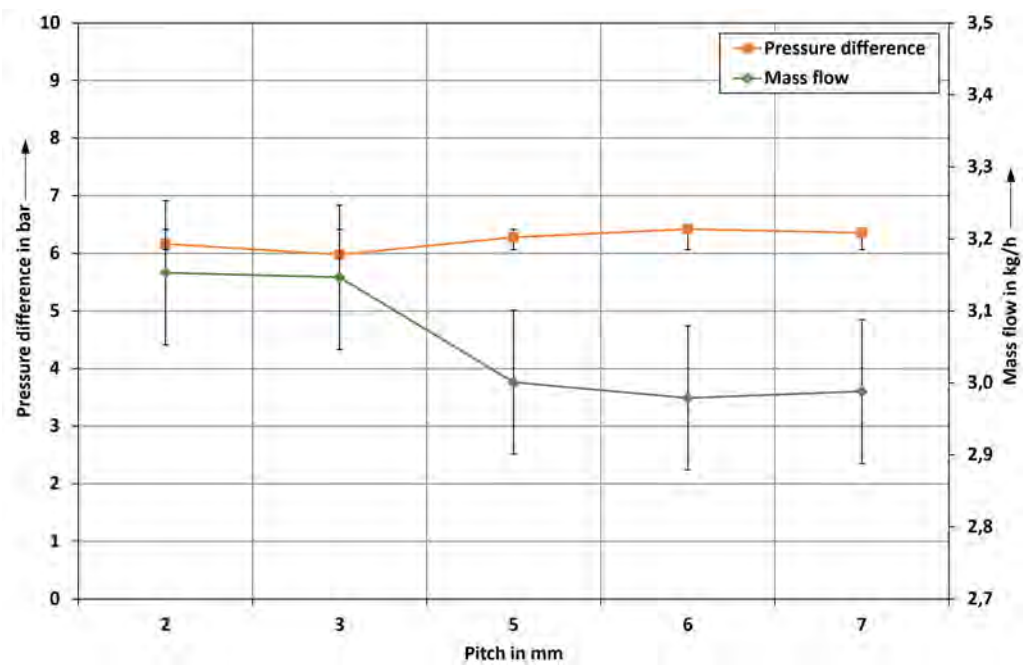
Figure 5.21.: Pressure difference and mass flow as a function of the pitch at 250 W
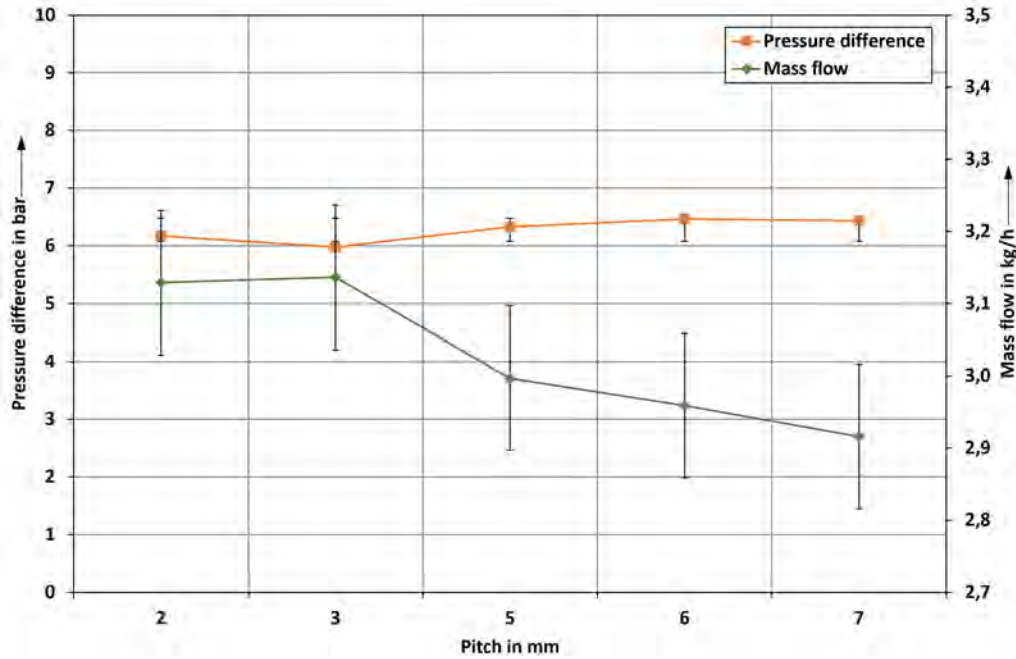
Figure 5.22.: Pressure difference and mass flow as a function of the pitch at 260 W

The results of this analysis show how important it is to choose the right swirl insert for the corresponding performance. For powers below 92.5 % of CHF, a pitch of 5 mm seems to be the optimal value. Above that, a pitch of 3 mm is optimal. Therefore, to operate a swirl evaporator with maximum efficiency, it should be operated at a power above 92.5 % of CHF. Then fully developed nucleate boiling prevails which is reflected in a high HTC of 40000 W/(m K).

5.6. Concept of the Optimized Swirl

At this point, it is critically to examined whether the concept of the "optimized swirl" described in Chapter 3, i.e. the swirl with a variable pitch, achieves the expected reduction in pressure drop without a reduction in the HTC or CHF. For this purpose, the swirl with the variable pitch is compared with a swirl insert that has the same number of threads in engagement and, on average, the same hydraulic diameter as shown in shown in Figure 5.23. First of all, it is noticeable that the characteristic increase in pressure

Figure 5.23.: Comparison of the different swirls

drop at higher heat loads is much lower with a variable pitch compared to a swirl insert with constant pitch. Consequently, the drop in mass flow is also lower with a variable pitch. Secondly, it is noticeable that the variable pitch generally causes a lower pressure loss. As can be seen from the graphs in Figure 5.24 and Figure 5.25, the heat transfer coefficient remains the same value at 28000 W/m² K) with constant and variable pitch. The CHF, which is not shown in graphs here, was also constant with both swirl inserts. The maximum transmissible power was 260±10 W in case of constant pitch swirl and
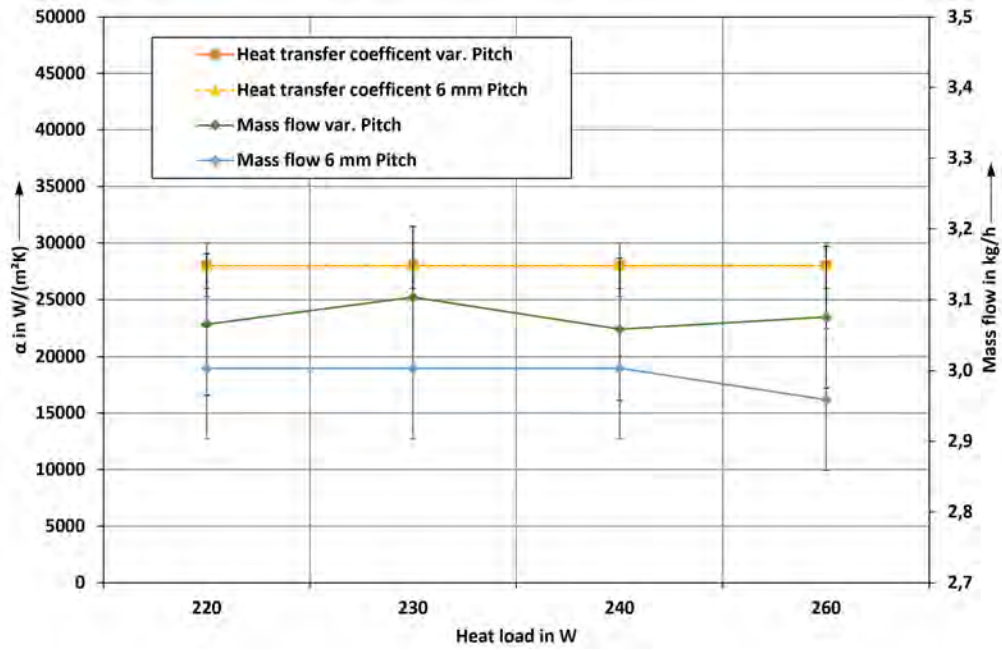
Figure 5.24.: Comparison of the mass flow variable and 6 mm pitch

260+10 W in case of variable pitch swirl. It can therefore be said that an optimization has been successfully achieved by varying the pitch.
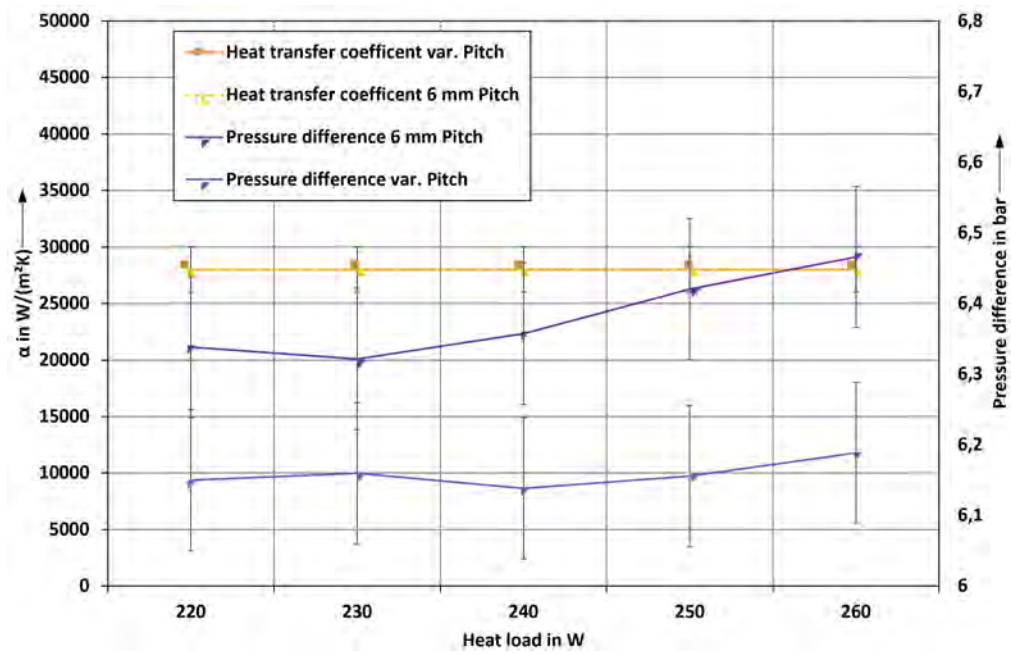
Figure 5.25.: Comparison of the pressure difference variable and 6 mm pitch

6. Transfer to Application Case

In order to prove the industrial applicability of the swirl evaporator, it was installed in the tool holder of a turning machine. In turning processes, the temperature results as a process variable from infeed, speed and feed. By cooling the cutting edge internally, cutting temperature can now be set as a controlled variable. This can reduce wear, which saves costs and benefits the environment. In addition, the cutting speed can be increased, which in turn increases productivity. (This novel technology was investigated within the framework of a cooperative research project together with the company MAS GmbH. Funding was provided under the project name Cool-Tool with the grant number ZF4102824TV8 from the Ministry for Economic Affairs and Climate Action of the Federal Republic of Germany.) The CAD drawing of the final product is shown in Figure 6.1.
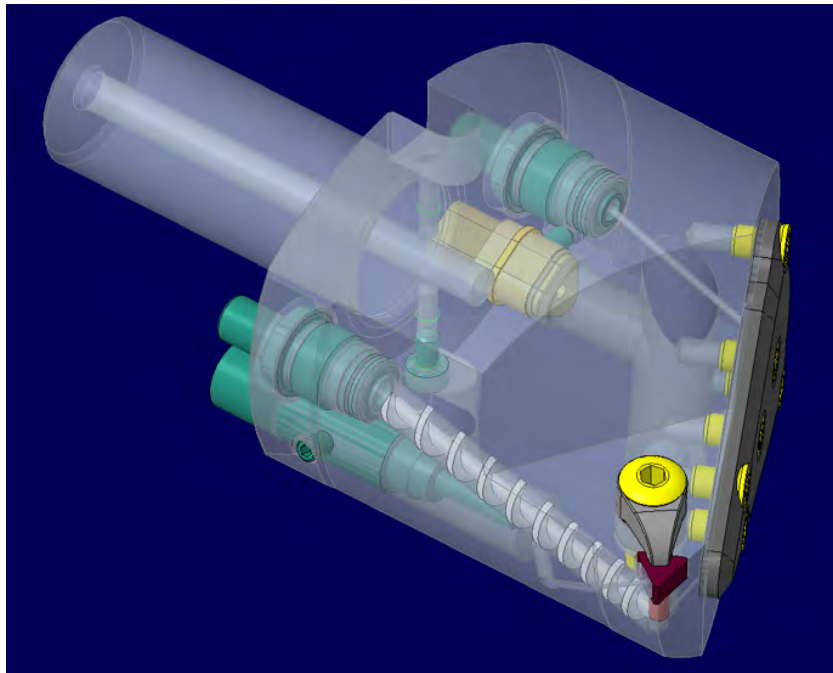
Figure 6.1.: Tool holder with evaporator [80]

6.1. Estimation of the Heat Load

In order to design the cooling process correctly, it is of fundamental importance to know the heat load. So not only how much heat is produced during the cutting process but also how the heat flows are distributed in between the tool, chip, work-piece, cutting fluid and environment. For this reason, heat generation and transportation during the cutting process will be briefly discussed here. Due to a different heat sink temperature, heat flows between chip, cutting edge and work piece will be distributed differently for a cutting process with or without internal cooling, but because of the novelty of this project no reference tests or literature is available. For this reason an FEM-based inverse thermal

analysis was performed. To simulate the thermal behavior, an equation-based model was developed in the EES software as well as an FEM model in the software Ansys. Almost all of the mechanical power supplied to the spindle drive is converted into heat in the cutting zone [102]. Figure 6.2 shows all relevant heat and enthalpy flows.
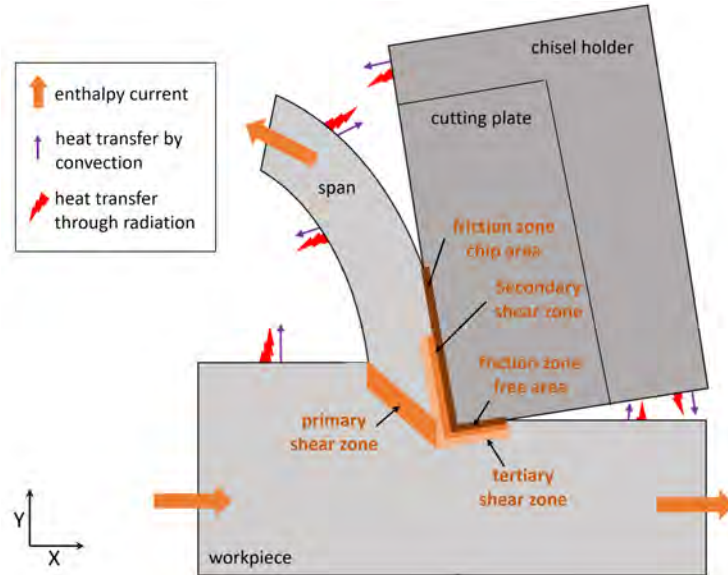
Figure 6.2.: Heat flows during the machining process (acc. to [102])

According to Müller [102], the transformation takes place mainly in the primary shear zone. From here, the heat flows into the chip, the work piece, the tool cutting edge and to the environment or the cooling lubricant. The exact distribution of the heat flows is decisive for the temperature of the cutting edge and thus for the thermal wear. The qualitative relationships and influencing factors are described in Table 6.1.

Table 6.1.: Influencing factors on the cutting temperature

	Thermal conductivity workpiece	Density workpiece	Thermal capacity workpiece	Thermal conductivity cutting material	Density cutting material	Thermal capacity cutting material
Influence on the cutting temperature	↗	↘	↘	↗	↗	↗

The thermal properties of solids can usually be described in terms of density, specific heat capacity and thermal conductivity. The heat flow in a given direction is directly proportional to the thermal conductivity of the body and the temperature gradient that occurs. In a transient heat transfer process, temperature gradient is equalized over time by the heat flow. The lower the density and the specific heat capacity of the body, the faster the temperature equalization takes place. The density and the specific heat capacity are directly proportional to the heat capacity of a body. According to Altmüller [9], the relationship between the heat flows flowing into the cutting edge or chip can be expressed

as

$$\frac{\dot{Q}_{\text{cut}}}{\dot{Q}_{\text{chip}}} = \frac{1}{\sqrt{\frac{\lambda_{\text{w}} \cdot \varrho_{\text{w}} \cdot c_{\text{pw}}}{\lambda_{\text{s}} \cdot \varrho_{\text{s}} \cdot c_{\text{ps}}}}}. \tag{6.1}$$

With constant thermal properties, the temperature difference between the hot and cold side is responsible for the magnitude of the heat flow that occurs. A model developed by Astakhov [13] is used to calculate the quantity of heat generated during machining. Similarity ratios are used for model development. The heat flow flowing into the cutting edge can be calculated with

$$\dot{Q}_{\text{t}} = \frac{0.54 \cdot \tau_{\text{fa}} \cdot a_1 \cdot b_1 \cdot \nu \cdot F^{0,86} \cdot D^{0.26} \cdot M^{0.47} \cdot E^{0.27} \cdot \text{erf}^{0.35} \cdot \sqrt{\frac{Pe \cdot B_{\text{a}}}{4}}}{Pe^{0.615} \cdot (1 - \sin(\gamma))^{0.5} \cdot \sin(\alpha)^{0.15} \cdot B_{\text{a}}0.72}. \tag{6.2}$$

Table 6.2 shows the influencing variables on the quantity of heat and distribution of the heat flow flowing into the cutting edge of the tool.
variables influencing the heat flow in tabular form.

Table 6.2.: Variables influencing the heat flow

Formula symbol	Influencing variable
α	Rake angle
β	Edge angle
c_{pw}	Specific heat capacity of the work piece
d_{w}	Shaft diameter work piece
ϵ_{tn}	Cutting insert angle
f_{z}	pitch
γ	Clearance angle
λ_{t}	Thermal conductivity tool
λ_{w}	Thermal conductivity material
κ_{r}	Setting angle
r_{n}	Cutting edge radius
ϱ_{w}	Density material
σ	Tensile strength material
t	Plunging depth
v	Cutting speed

Zhao et al. [146] investigated the influence of surface roughness on thermal contact resistance. This is based on the consideration that the heat flow is transferred almost exclusively at the "peaks", since only there, as shown in Figure 6.3, a contact between tool and work piece takes place. The researchers concluded that the roughness has a negligible influence on the thermal contact resistance [146].
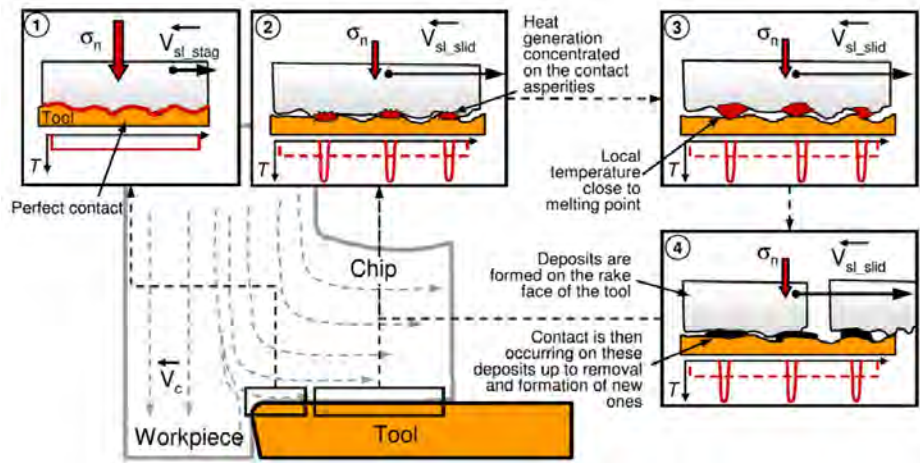
Figure 6.3.: Thermal contact resistance [146]

Table 6.3 shows the factors influencing the quantity of heat and distribution of the heat flow.

Table 6.3.: Factors influencing the heat flow

Influencing factor	Value	Gradient	Gradient value
Rake angle α	10	$\partial \dot{Q}/\partial \alpha$	-56.63
Wedge angle β	70	$\partial \dot{Q}/\partial \beta$	47.90
Specific heat capacity work piece c_{pw}	$671\,\mathrm{J/(kg\,K)}$	$\partial \dot{Q}/\partial c_{\mathrm{w}}$	-4.69
Shaft diameter $\mathrm{d_w}$	$20\,\mathrm{mm}$	$\partial \dot{Q}/\partial d_{\mathrm{w}}$	56091.00
Cutting insert angle ϵ_{tn}	80	$\partial \dot{Q}/\partial \epsilon_{\mathrm{tn}}$	41.91
pitch f_{z}	$0.01\,\mathrm{mm}$	$\partial \dot{Q}/\partial f_{\mathrm{z}}$	$1.45 \cdot 10^{8}$
Clearance angle γ	10	$\partial \dot{Q}/\partial \gamma$	30.99
Thermal conductivity tool λ_{t}	$50\,\mathrm{W/(m\,K)}$	$\partial \dot{Q}/\partial \lambda_{\mathrm{t}}$	22.81
Thermal conductivity work piece λ_{w}	$20\,\mathrm{W/(m \cdot K)}$	$\partial \dot{Q}/\partial \lambda_{\mathrm{w}}$	-33.73
Setting angle κ_{r}	90	$\partial \dot{Q}/\partial \kappa_{\mathrm{r}}$	$1.34 \cdot 10^{-6}$
Cutting edge radius r_{n}	$200\,\mu\mathrm{m}$	$\partial \dot{Q}/\partial r_{\mathrm{n}}$	$1.029 \cdot 10^{7}$
Density work piece ϱ_{w}	$8000\,\mathrm{kg/m^3}$	$\partial \dot{Q}/\partial \varrho_{\mathrm{w}}$	-0.29
Tensile Strength work piece σ	$800\,\mathrm{N/mm^2}$	$\partial \dot{Q}/\partial \sigma$	$4.762 \cdot 10^{-6}$
Plunging depth t_1	$1\,\mathrm{mm}$	$\partial \dot{Q}/\partial t_1$	$2.8 \cdot 10^{6}$
Cutting speed v	$1.67\,\mathrm{m/s}$	$\partial \dot{Q}/\partial v$	881.10

Figure 6.4 shows the gradients of the investigated influencing factors at the selected operating point logarithmically. The blue bars indicate negative effects. This means that the heat flow into the cutting edge decreases due to larger rake angle, higher heat capacity, thermal conductivity and density of the material. The strongest influence on the heat flow has feed, corner radius, diameter of the work piece, depth of cut and cutting speed. With the selected method of gradient determination, it must be noted that linearization takes place at the corresponding operating point. In principle, this means that only the effects of small changes can be recorded correctly. For this reason, individual influencing factors are examined more closely in order to show the dependence of the heat flow on these variables in a wider definition range. Here, cutting speed, feed rate and infeed depth

are used, which are determined by the machine operator and not by the tool geometry.
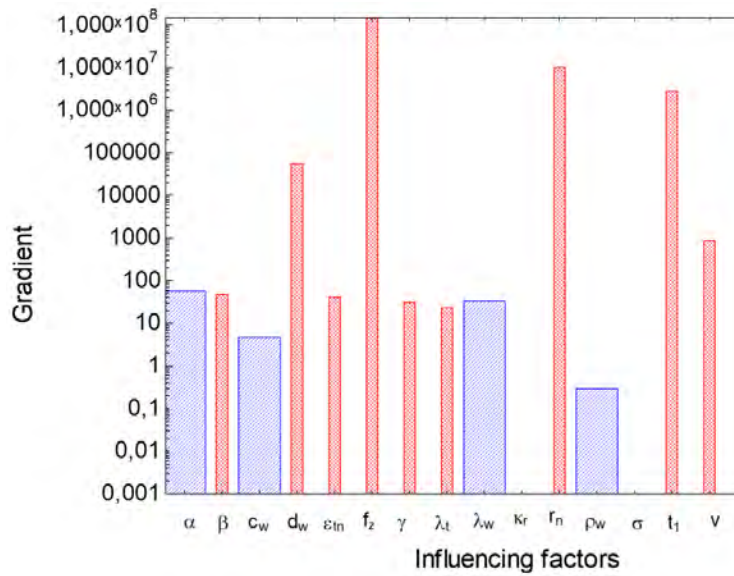
Figure 6.4.: Influencing factors on heat generation

The heat flow flowing into the cutting edge is shown for different feeds in Figure 6.5. This knowledge is crucial, as it is the basis for designing the swirl evaporator for the specific heat load. The course of the heat flow as a function of the cutting speed corresponds to a root function. The heat flow generated during cutting increases proportionally to the cutting speed. This means that the proportion of heat flow in the tool continues to decrease as the cutting speed increases. To verify Astakov's model, an inverse analysis was performed.
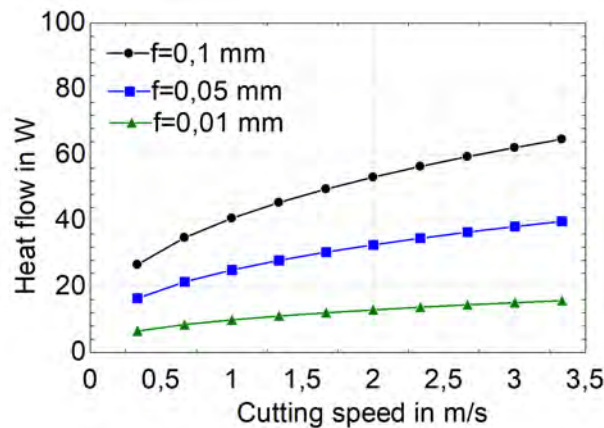
Figure 6.5.: Heat flow for different cutting speeds and depths

For this purpose, an FEM model of the complete tool-holder including the cutting edge was created, as showed in Figure 6.6. To determine the heat transfer surface, a CBN (cubic boron nitride) cutting edge was coated with metal and used in a test [43]. The abraded area was assumed to be the heat transfer surface.
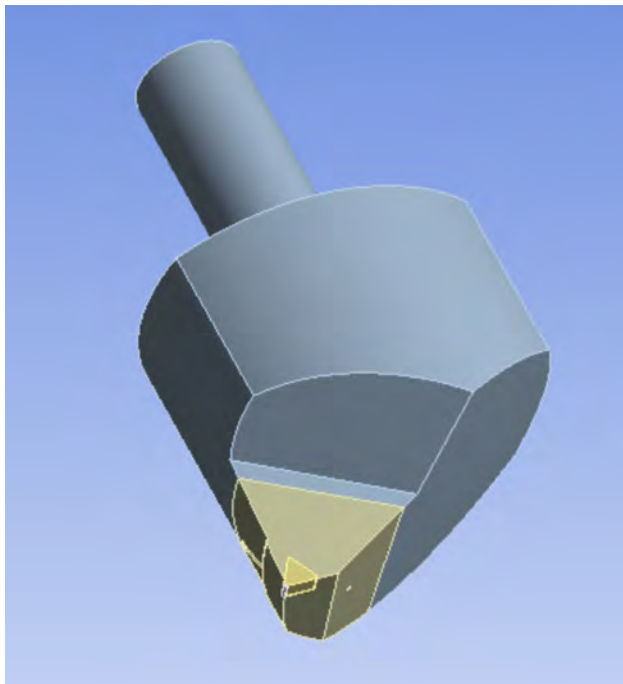
Figure 6.6.: Model of the tool holder

Figure 6.7 shows a photograph of the cutting edge with the area of the heat-transferring surface marked in red.
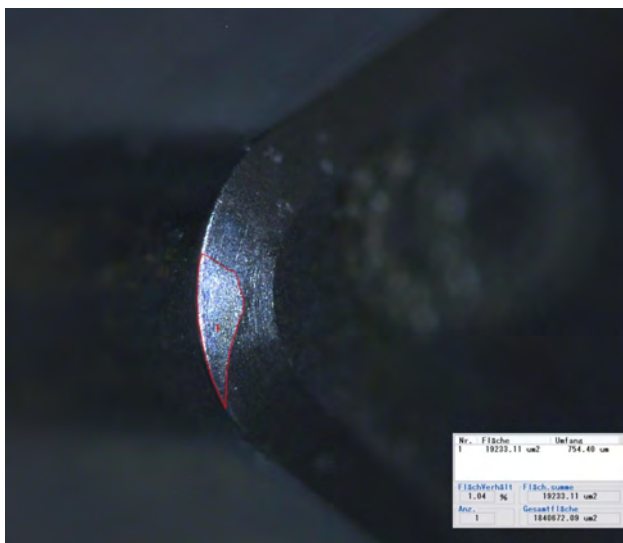
Figure 6.7.: Photography of the cutting edge [43]

Now that the size of the heat-transferring surface is known, the heat input into the cutting edge can be simulated. The FEM mesh of the cutting edge is shown in Figure 6.8 (l). The picture also shows the 3 thermocouple holes in which the temperatures are recorded. The simulated temperature field is shown in Figure 6.8 (r).
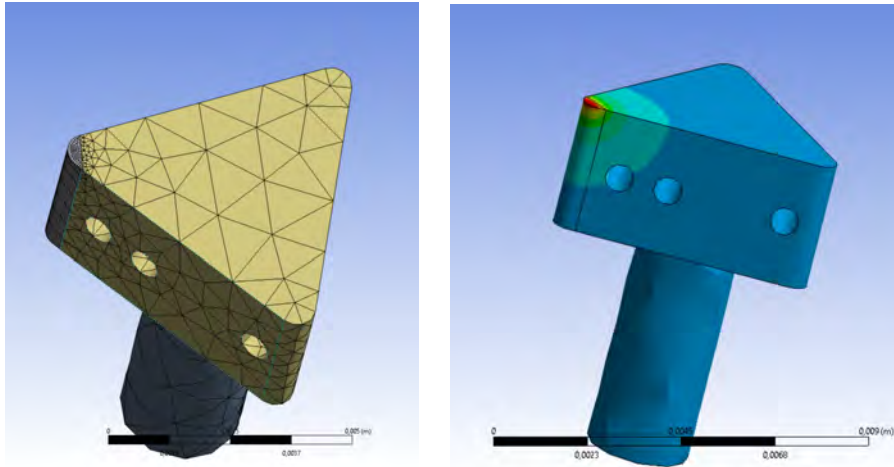
Figure 6.8.: FEM mesh of the cutting edge (l) and temperature field (r)

In order to check the simulated heat input and the resulting temperature fields, a soldering iron was modified so that its output can be precisely controlled. The soldering iron was insulated so that its power dissipation is minimal and brought into good thermal contact with the board using solder. The corresponding experimental setup is shown on the left side of Figure 6.9. With this knowledge, field test can now be started.

6.2. Test and Results

A swirl evaporator was installed in a tool holder. The corresponding test setup is shown in Figure 6.9 (r). Here the type J thermocouples are visible, which are placed at a distance of 1, 2 and 4 mm from the cutting edge.
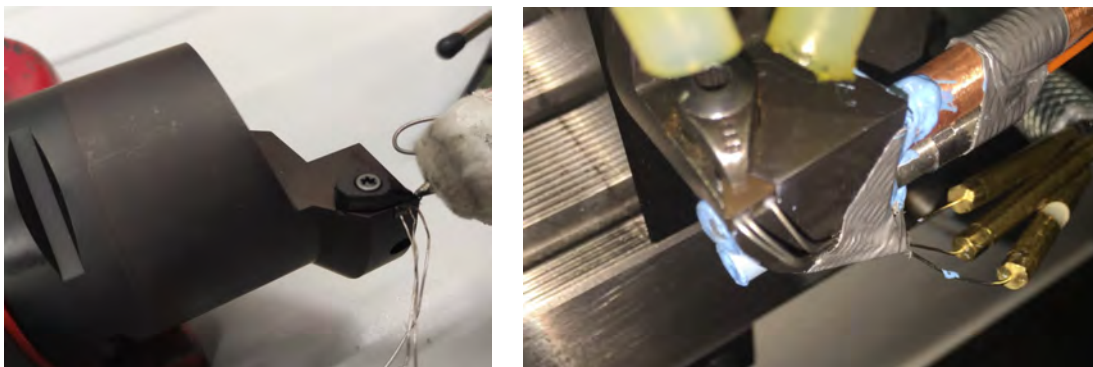
Figure 6.9.: Experimental setup for inverse analysis (l) and field experiment [81] (r)

Figure 6.10 shows the test results with a cooled cutting edge and Figure 6.11 with an uncooled cutting edge. The tests were generated at the project partner and evaluated by the author. Tests were carried out with a cutting speed of 1.67 m/s, a feed rate of 0.1 mm/rev and an infeed of 0.1 mm. In each case, 5 cuts were made with the same work piece. After each 3 measurements, the plate was rinsed. Figure 6.11 and Figure 6.10 show the 5 cuts made with the same work piece and the 3 successive work pieces. Figure 6.11 shows that the temperature in the first work piece rises continuously and from the 2nd

work piece and 3rd cut onwards it is in a steady state. Temperatures corresponding to the quasi-steady state were used to determine the thermal power flowing into the mold.
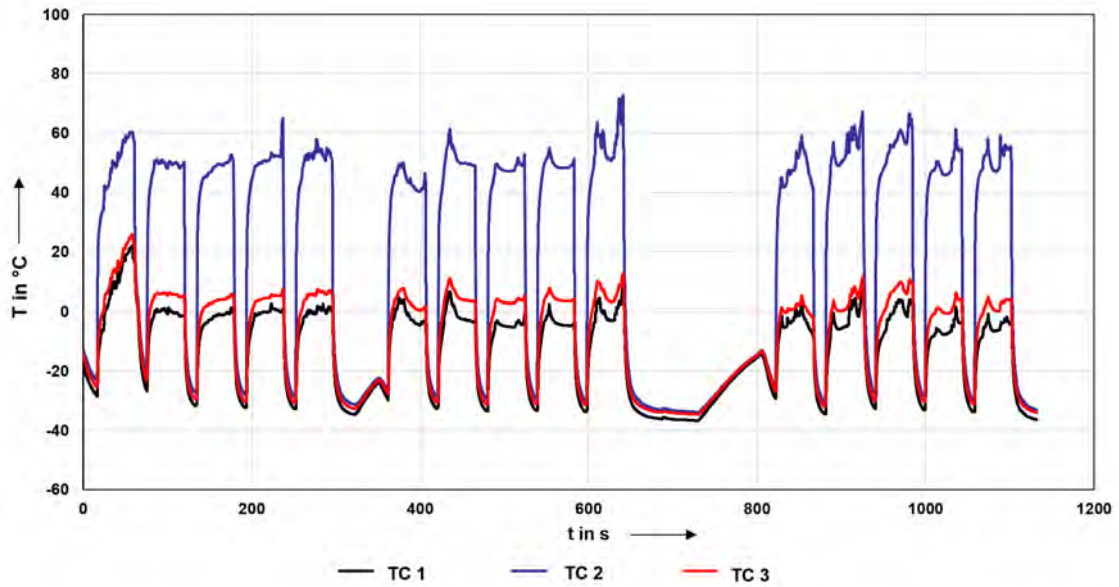
Figure 6.10.: Temperature curve with cooled cutting edge [81]

The evaporation temperature of the experiments with cooled cutting edge was $-40\,°C$. As can be seen from the comparison of the two figures, the average temperature of the uncooled cutting edge is about $50\,K$ above the cooled cutting edge. The inverse analysis shows that the heat flow into the tool increases by $> 14\,\%$ when the tool is cooled.
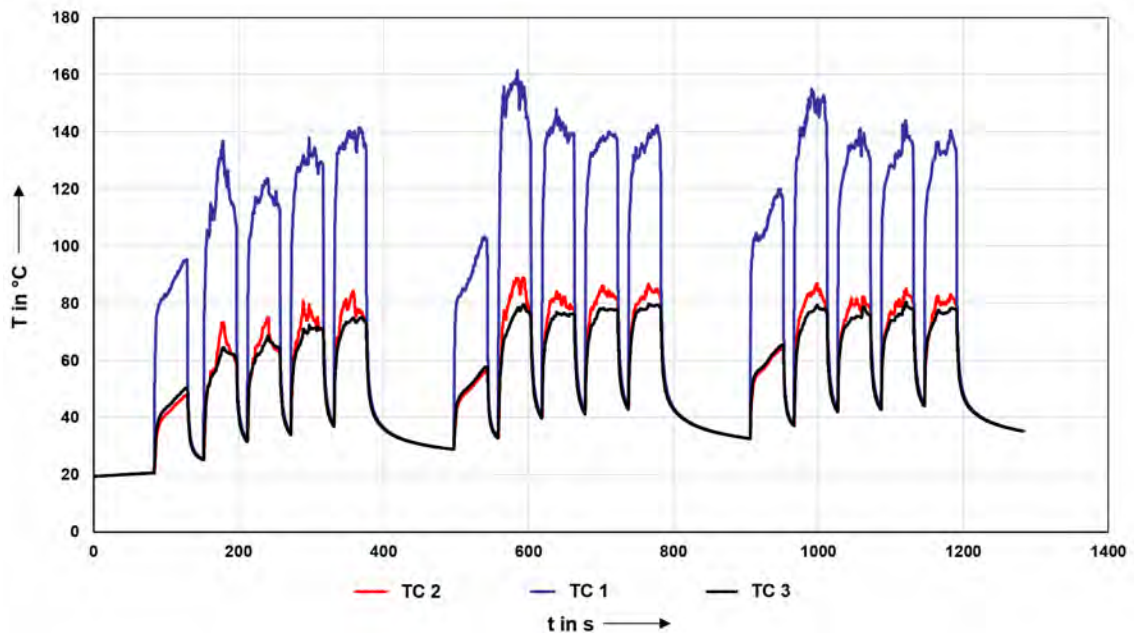
Figure 6.11.: Temperature curve with uncooled cutting edge [81]

The results of the test evaluation presented in Figure 6.12 show that the wear mark width could be reduced by 50 % by using a swil evaporator. The results for CBN69 are shown on the left and those for CBN492 on the right. A reduction of 50 % means that either the tool life or the cutting speed can be doubled. These results were demonstrated at the project partner MAS [81].
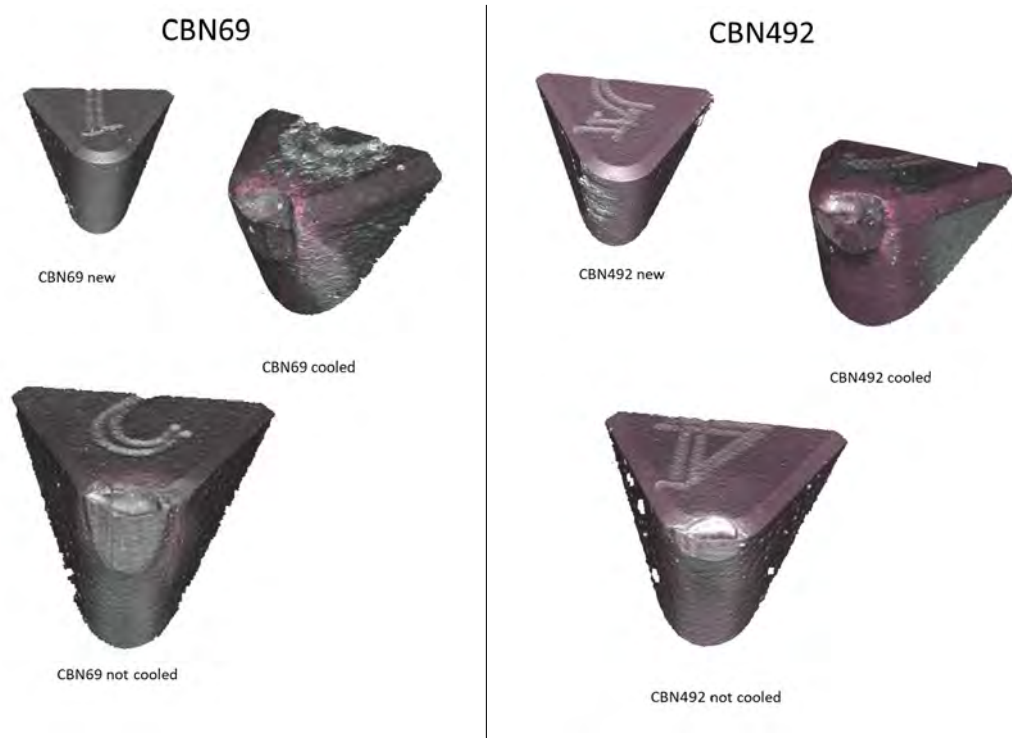
Figure 6.12.: CBN tools cooled vs. not cooled [81]

7. Conclusion and Future Work

The presented work founds a basis for calculating and designing swirl evaporators for a wide range of industrial applications. The formulas and procedures provided allow this in a time and cost efficient manner.

7.1. Conclusiones

En esta tesis se ha investigado el proceso de evaporación del R-32 en evaporadores helicoidales cortos con valores de paso bajos, altos y variables, radio de curva estrecho y diámetros hidráulicos pequeños a bajas presiones y con elevado flujo secundario. Los resultados indican que la caída de presión en una sección de evaporación helicoidal es menor que en un evaporador recto de la misma longitud y diámetro. Otros resultados muestran que el contenido de vapor x_{crit} cuando se alcanza el flujo de calor crítico es mayor para un diseño de evaporador helicoidal que para un de evaporador recto, lo que indica que se evapora más refrigerante antes de que se alcance el flujo de calor crítico. Esto indica una mayor eficiencia general del proceso ya que una canteiad menor de refrigerante sale del sistema sin evaporar.

Al insertar una geometría helicoidal, la trayectoria en el evaporador se extiende y el refrigerante líquido se presiona contra la pared debido a la aceleración centrífuga. Por estas razones, se puede evaporar más refrigerante antes de que se alcance el flujo de calor crítico. Por lo tanto, el evaporador funciona de manera más eficiente y se puede ahorrar energía primaria. Se ha demostrado que las trayectorias helicoidales cortas con bajo radio de curvatura se pueden calcular como trayectorias rectas. Sin embargo, este efecto parece cambiar a favor de una menor caída de presión a medida que aumenta la longitud de la sección del evaporador helicoidal.

Por lo tanto, la tesis de Hardik [59, 58] podría confirmarse con el conocimiento adicional de que sus leyes también son válidas si el flujo helicoidal está precedido por un enfriamiento por aspersión y el refrigerante ingresa a la sección del evaporador con flujo bifásico. Asimismo, la tesis de Groeneveld et al. [54] es compatible, ya que el conjunto de datos y el método de conversión que generaron se pueden usar más allá de su campo de aplicación original. Al menos para la determinación del CHF en el evaporador helicoidal, los resultados son bastante satisfactorios.

Para obtener estos resultados, se desarrollaron y verificaron experimentalmente modelos físicos y de correlación para calcular la caída de presión y la transferencia de calor. Con la ayuda de este trabajo es posible diseñar evaporadores helicoidales para diferentes aplicaciones, espacios y cargas de enfriamiento. Además, el modelo permite predecir el CHF con una precisión de $< 9\,\%$, lo que posibilita una operación segura del proceso cercana al punto óptimo de operación. Con la ayuda del modelo basado en correlación, fue posible diseñar una geometría con paso variable y así optimizar el sistema en términos de caída de presión. Se creó un modelo de voúmenes finitos para la determinación inversa del coeficiente de transferencia de calor en el evaporador. Este modelo es adecuado para

determinar los coeficientes de transferencia de calor local y promedio.

Desde el punto de vista técnicó, la transferencia de calor por debajo del calor crítico y el propio flujo de calor crítico son más importantes que la transferencia de calor en la ebullición en película. Por lo tanto, la atención se centró en la ebullición nucleada y no se desarrollaron modelos para describir la transferencia de calor en la ebullición en película. El modelo de volúmenes finitos para el cálculo de coeficientes de transferencia de calor promediados funciona con alta precisión en el rango de ebullición nucleada y por debajo del flujo crítico, pero pierde precisión en el rango de ebullición de transición y no es válido en el rango de ebullición en película. Esta validez se puede recuperar dividiendo las regiones en diferentes regímenes y coeficientes de transferencia locales, lo que funciona razonablemente bien y se analizará en el futuro.

Al implementar un evaporador helicoidal en un proceso de mecanización, el desgaste de la herramienta podría reducirse significativamente, lo que tiene una influencia positiva en la productividad del proceso. Sin embargo, los evaporadores rotatorios no solo son adecuados para el enfriamiento interno de una herramienta de torneado, sino también donde sea necesario refrigerar un alto flujo de calor en un espacio cilíndrico limitado, como la refrigeración de puntos calientes en el moldeo por inyección, sonotrodos o de estatores en motores eléctricos.

Como resumen, se puede señalar que en este trabajo se desarrolló un método y el modelo asociado para hacer que una tecnología de refrigeración se pueda utilizar para varios campos de aplicación de una manera segura para el proceso. El modelo se verificó experimentalmente y es adecuado para determinar todas las variables relevantes para el diseño, realizar optimizaciones específicas de la aplicación y garantizar un funcionamiento seguro del proceso.

7.2. Conclusion

The thesis is focused on investigating the evaporation process of R-32 in short helical evaporators with low, high and variable pitches, a narrow curve radius and small hydraulic diameters at low pressures and a strong secondary flow. The results indicate that pressure drop in a helical evaporation section is lower than in a straight evaporator of the same length and diameter. Further results show that the vapor content x_{crit} prevailing when the critical heat flux is reached is higher for a helical evaporator structure than for a straight evaporator structure, indicating that more refrigerant evaporates before the critical heat flux is reached. This indicates an overall higher efficiency of the process as less refrigerant leaves the system unevaporated.

By inserting a helical geometry the evaporator path is extended and liquid refrigerant is pressed against the wall due to centrifugal acceleration. For these reasons, more refrigerant can evaporate before CHF is reached. The evaporator therefore works more efficiently and primary energy can be saved. It has been shown that short helical paths with a tight radius of curvature can be calculated as straight paths. However, this effect seems to shift in favor of a lower pressure drop with increasing length of the helical evaporator section. Thus, the thesis of Hardik [59, 58] could be confirmed with the additional knowledge that his laws are also valid if the helical flow is preceded by a spray cooling and the refrigerant already enters the evaporator section two-phased. Likewise, the thesis of

Groeneveld et al. [54] is supported, as the data set and conversion method they generated can be used beyond its original field of application. At least for the determination of CHF in the swirl evaporator, the results are quite satisfactory.

To obtain these results, physical and correlation based models were developed and experimentally verified to calculate pressure drop and heat transfer. With the help of this work it is possible to design swirl evaporators for different applications, spaces and cooling loads. In addition, the model allows to predict the CHF with an accuracy of $< 9\,\%$, which enables a process safe operation close to the optimal operating point. With the help of the correlation-based model, it was possible to design a swirl with a variable pitch and thus optimize the system in terms of pressure drop. An FEM model of the swirl evaporator test carrier was created for inverse determination of HTCs in the swirl evaporator. This model is suitable for determining both, averaged and local heat transfer coefficients in the swirl evaporator.

From a technical perspective, heat transfer below the critical heat and CHF itself are more important than heat transfer in film boiling. Therefore, the focus was set on nucleate boiling and no models were developed to describe heat transfer in film boiling. The heat transfer model of the FEM calculation with the averaged (lumped) HTCs works with high accuracy in the nucleate boiling range and below the CHF, but loses accuracy in the transition boiling range and is no longer valid in the film boiling range. This validity can be restored by dividing the regions into different local HTCs, which works reasonably well and will be analyzed in the future.

By implementing a swirl evaporator in a cutting process, the wear of the insert could be significantly reduced, which has a positive influence on productivity of the cutting process. However, swirl evaporators are not only suitable for internal cooling of a turning tool, but also wherever high heat flux has to be cooled in a limited cylindrical space, like the cooling of hot spots in injection molding, the cooling of sonotrodes or the cooling of stators in electric motors.

As summary can be noted that a method and the associated model were developed in this work to make a cooling technology usable for various fields of application in a process-safe manner. The model was verified experimentally and is suitable for determining all design-relevant variables, performing application-specific optimizations and ensuring process-safe operation.

7.3. Challenges for Further Investigations

Relationships in the swirl evaporator could be clarified within the scope of this work to the extent that it can be designed and calculated for industrial applications. Nevertheless, a Computational Fluid Dynamics (CFD) simulation of the process would be interesting. However, the state of knowledge at the time of the thesis was only so far that, with the resources available at time, only a large-eddy simulation could satisfactorily represent the prevailing conditions (one- and two-phase pressure loss in the capillary tube, one- or two-phase spray on hot wall, deflection by 180° with further evaporation and then two-phase flow simulation in the helical evaporator geometry). However, the research field

of two-phase CFD simulation is currently making enormous progress every year. Furthermore, with the knowledge of the initial and boundary conditions, simpler equation (e.g. the Spalart-Allmaras) or two-equation turbulence models (e.g. k-ε or other RANS (Reynolds Averaged Navier Stokes) turbulence models[1] can be used for a CFD simulation.

In the course of this work, considerations were made regarding to use some kind of swirl evaporator to cool flat surfaces. To be able to cool cylindrical geometries with high efficiency has its benefits, but a flat cooling surface would be suitable for a much wider rage of applications, such as processor cooling and could be an alternative to micro- and mini-channel evaporators. Therefore, considerations were made about how to design a swirl evaporator "flat". One possibility to achieve this is a spiral evaporator geometry as shown in Figure 7.1. In this evaporator/heat exchanger the liquid refrigerant is fed through the supply line (Figure 7.1, Label 12) and then sprayed centrally onto the heat transferring surface, as displayed in as Label 16 in Figure 7.1–7.3. After that it is led to the outside in a spiral evaporator channel (Label 20). The channel is structured like an archimedean spiral and has an increasing cross-sectional area. This keeps the flow velocity of the evaporating fluid constant and minimizes the pressure drop. The lateral evaporator wall (Label 30) is at a 45° angle (shown as α in Figure 7.3). When the refrigerant flows out, centrifugal forces create a cross flow and the liquid refrigerant is directed to the heat transfer surface (Label 28). This theoretical consideration should be explored in a future work. Since the spiral geometry is reminiscent of a scroll compressor screw, this type of evaporator is called a scroll evaporator. The scroll evaporator can be built flat so that flat surfaces, such as aforementioned CPUs or GPUs are cooled and hence represent an alternative to mini- or micro-channel evaporators. The scroll evaporator could also have a hemispherical shape to cool spherical elements or free-form surfaces such as those found in an injection mold. Other possible applications would include cooling various areas of electric vehicles such as batteries, converters or motors.
Due to the increasing possibilities offered by additive manufacturing, cooling can be carried out close to the contour and in different geometries/free-form surfaces. The scroll evaporator was filed as German Patent Application No. 102021204547.2 with the German Patent and Trademark Office in Munich on May 5, 2021 [45]. Table 7.1 references the numbers and symbols used in Figures 7.1, 7.2 and 7.3.

---

[1]RANS is initially not a turbulence model, but a different representation of the Navier-Stokes equations, namely the equations time-averaged. This gives rise, assuming the Reynolds rules are applicable, to an additional term, namely the Reynolds stresses. The turbulence model then comes into play to estimate the Reynolds stresses, since they are not closed-form solvable (i.e. there are more unknowns than equations).
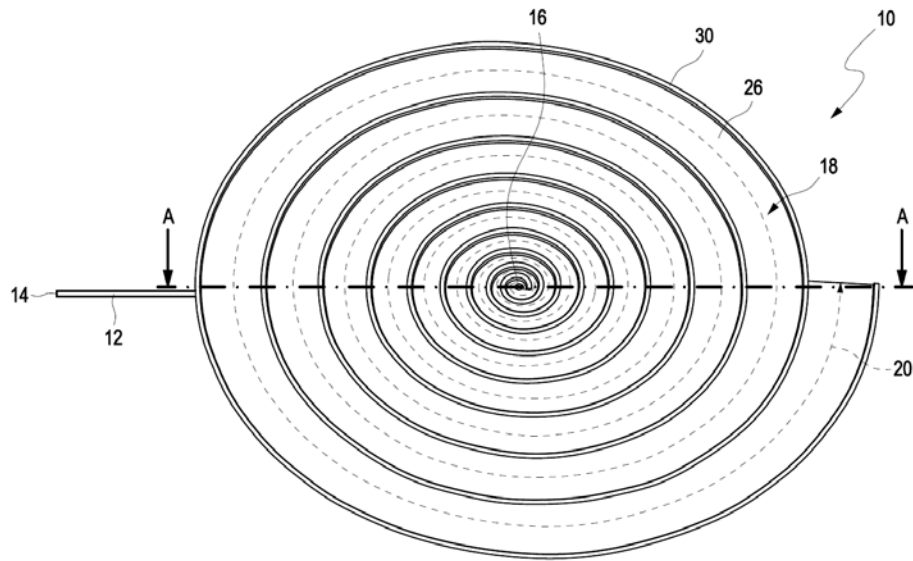
Figure 7.1.: Top view scroll evaporator [45]
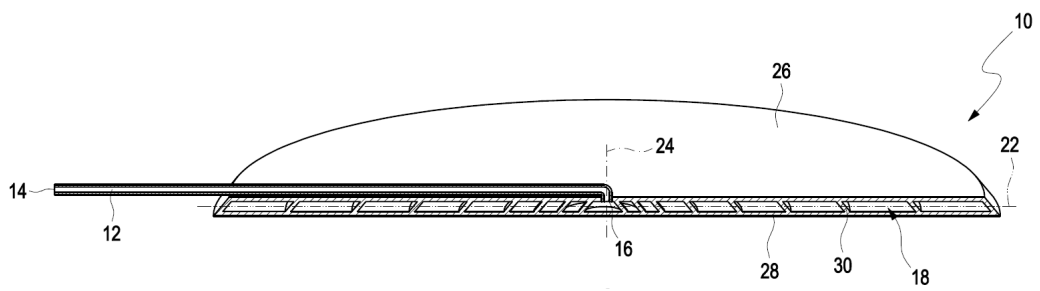
Figure 7.2.: Cut view of the scroll evaporator [45]
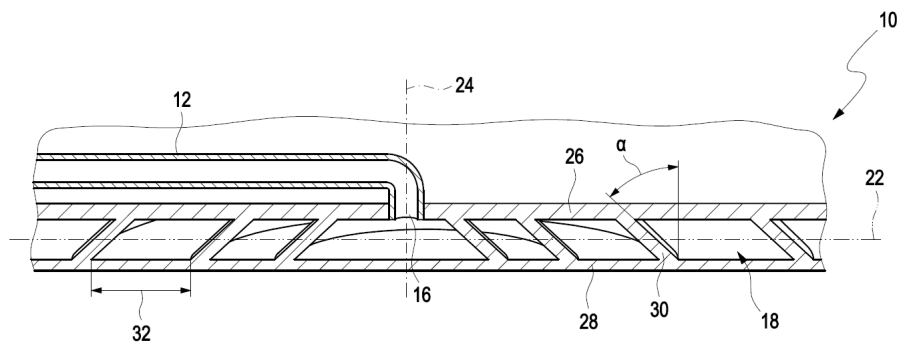
Figure 7.3.: Detail view of the scroll evaporator [45]

Table 7.1.: Reference list

10	Evaporator
12	Supply line
14	Refrigerant channel
16	Inlet port
18	Outlet port
20	Evaporator path length
22	Horizontal section plane
24	Center axis
26	Upper duct wall
28	Lower duct wall
30	Lateral duct wall
32	Cross-sectional area
α	Angle

Bibliography

[1] DIN 1319-1:1995-01, Grundlagen der Meßtechnik - Teil 1: Grundbegriffe.

[2] DIN 4108-4:2020-11, Wärmeschutz und Energie-Einsparung in Gebäuden - Teil 4: Wärme- und feuchteschutztechnische Bemessungswerte.

[3] Abbasi, B., Kim, J., and Marshall, A. Dynamic pressure based prediction of spray cooling heat transfer coefficients. *International Journal of Multiphase Flow 36*, 6 (2010), 491–502.

[4] Abishek, S., Narayanaswamy, R., and Narayanan, V. Effect of heater size and reynolds number on the partitioning of surface heat flux in subcooled jet impingement boiling. *International Journal of Heat and Mass Transfer 59* (2013), 247–261.

[5] Agostini, B., Fabbri, M., Park, J. E., Wojtan, L., Thome, J. R., and Michel, B. State of the art of high heat flux cooling technologies. *Heat Transfer Engineering 28*, 4 (2007), 258–281.

[6] Agostini, B., Revellin, R., Thome, J. R., Fabbri, M., Michel, B., Calmi, D., and Kloter, U. High heat flux flow boiling in silicon multi-microchannels–Part III: Saturated critical heat flux of R236fa and two-phase pressure drops. *International Journal of Heat and Mass Transfer 51*, 21-22 (2008), 5426–5442.

[7] Akers, W. W., Deans, H. A., and Crosser, O. K. Condensing heat transfer within horizontal tubes. *Chem. Eng. Progr.*.

[8] AlleBerechnungen.com. Helix. URL: `https://www.alleberechnungen.com/geometrie/evoluten-helix.php`, accessed on 12. 11. 2020.

[9] Altmüller, S. *Simultanes fünfachsiges Fräsen von freiformflächen aus Titan*. Shaker, 2001.

[10] Anowar Hossain, M., Onaka, Y., Afroz, H. M., and Miyara, A. Heat transfer during evaporation of r1234ze(e), R32, R410a and a mixture of R1234ze(E) and R32 inside a horizontal smooth tube. *International Journal of Refrigeration 36*, 2 (2013), 465–477.

[11] Ansys Inc. Lecture 7: Mesh quality advanced topics. In *Introduction to ANSYS Meshingt*. 2015, pp. 1–37.

[12] Assael, M., Dalaouti, N., Griva, A., and Dymond, J. Viscosity and thermal conductivity of halogenated methane and ethane refrigerants. *International journal of refrigeration 22*, 7 (1999), 525–535.

[13] Astakhov, V. P. *Metal cutting mechanics*. CRC press, 1998.

[14] Baehr, H. D., and Kabelac, S. *Thermodynamik*. Springer Berlin Heidelberg, Berlin, Heidelberg, 2016.

[15] BARRAU, J., CHEMISANA, D., ROSELL, J., TADRIST, L., AND IBÁÑEZ, M. An experimental study of a new hybrid jet impingement/micro-channel cooling scheme. *Applied Thermal Engineering 30*, 14-15 (2010), 2058–2066.

[16] BELISHEV, M. Boundary control method and inverse problems of wave propagation. In *Encyclopedia of Mathematical Physics: Five-Volume Set*. 2004, pp. 340–345.

[17] BERGLES, A. E. *Forced-convection surface-boiling heat transfer and burnout in tubes of small diameter*. PhD thesis, Massachusetts Institute of Technology, 1962.

[18] BERGLES, A. E., COLLIER, J., DELHAYE, J. M., HEWITT, G., AND MAYINGER, F. *Two-phase flow and heat transfer in the power and process industries*. Hemisphere New York, 1981.

[19] BLASIUS, H. Das Ähnlichkeitsgesetz bei Reibungsvorgängen in Flüssigkeiten. In *Mitteilungen über Forschungsarbeiten auf dem Gebiete des Ingenieurwesens*. Springer, 1913, pp. 1–41.

[20] BÖCKH, P., AND WETZEL, T. *Wärmeübertragung: Grundlagen und Praxis*, 7. Aufl. 2017 ed. Springer Berlin Heidelberg, Berlin, Heidelberg, 2018.

[21] BOHL, W., AND ELMENDORF, W. *Technische Strömungslehre: Stoffeigenschaften von Flüssigkeiten und Gasen, Hydrostatik, Aerostatik, inkompressible Strömungen, kompressible Strömungen, Strömungsmesstechnik*. Vogel-Fachbuch Kamprath-Reihe. Vogel, Würzburg, 2005.

[22] BROWN, G. O. The History of the Darcy-Weisbach Equation for Pipe Flow Resistance. In *Environmental and Water Resources History* (Reston, VA, 10172002), J. R. Rogers and A. J. Fredrich, Eds., American Society of Civil Engineers, pp. 34–43.

[23] CARLSON, K. RELAP5/MOD3 code manual. *NUREG/CR-5535* (1990).

[24] CHEN, J. C. Correlation for boiling heat transfer to saturated fluids in convective flow. *Industrial & Engineering Chemistry Process Design and Development 5*, 3 (1966), 322–329.

[25] CHEN, R.-H., CHOW, L. C., AND NAVEDO, J. E. Effects of spray characteristics on critical heat flux in subcooled water spray cooling. *Journal of Heat Transfer 45*, 19 (2002), 4033–4043.

[26] CHENG, L., RIBATSKI, G., AND THOME, J. R. Two-phase flow patterns and flow-pattern maps: fundamentals and applications. *Applied Mechanics Reviews 61*, 5 (2008).

[27] CHISHOLM, D. Pressure gradients due to friction during the flow of evaporating two-phase mixtures in smooth tubes and channels. *International Journal of Heat and Mass Transfer 16*, 2 (1973), 347–358.

[28] CHISHOLM, D. Two-phase flow in pipelines and heat exchangers.

[29] CHOWDHURY, S. *Study of Condensation of Refrigerants in Micro-channels for Development of Future Compact Micro-channel Condensers*. PhD thesis, 2008.

[30] CHURCHILL, S. W. Friction-factor equation spans all fluid-flow regimes.

[31] CICCHITTI, A., LOMBARDI, C., SILVESTRI, M., SOLDAINI, G., AND ZA-VATTARELLI, R. Two-phase cooling experiments: Pressure drop, heat transfer and burnout measurements. 407–425.

[32] COLEBROOK, C. F., BLENCH, T., CHATLEY, H., ESSEX, E., FINNIECOME, J., LACEY, G., WILLIAMSON, J., AND MACDONALD, G. Correspondence. turbulent flow in pipes, with particular reference to the transition region between the smooth and rough pipe laws.(includes plates). *Journal of the Institution of Civil engineers 12*, 8 (1939), 393–422.

[33] COOPER, M. G. Heat flow rates in saturated nucleate pool boiling-a wide-ranging examination using reduced properties. vol. 16 of *Advances in Heat Transfer*. Elsevier, 1984, pp. 157–239.

[34] DEHGHAN, M. Identification of a time-dependent coefficient in a partial differential equation subject to an extra measurement. *Numerical Methods for Partial Differential Equations: An International Journal 21*, 3 (2005), 611–622.

[35] DEHGHAN, M. Parameter determination in a partial differential equation from the overspecified data. *Mathematical and computer modelling 41*, 2-3 (2005), 196–213.

[36] DEHGHAN, M., AND TATARI, M. The radial basis functions method for identifying an unknown parameter in a parabolic equation with overspecified data. *Numerical Methods for Partial Differential Equations: An International Journal 23*, 5 (2007), 984–997.

[37] DIDI, M. O., KATTAN, N., AND THOME, J. Prediction of two-phase pressure gradients of refrigerants in horizontal tubes. *International Journal of refrigeration 25*, 7 (2002), 935–947.

[38] DIN-EN. 378-1: 2018-04. *Kälteanlagen und Wärmepumpen_-Sicherheitstechnische und umweltrelevante Anforderungen_-Teil_1: Grundlegende Anforderungen, Begriffe, Klassifikationen und Auswahlkriterien.*

[39] DITTUS, F., AND BOELTER, L. Heat transfer in automobile radiators of tubular type. *CA: University of California Press* (1930).

[40] ELSAYED, A. M. *Heat transfer in helically coiled small diameter tubes for miniature cooling systems.* PhD thesis, University of Birmingham, 2011.

[41] EUROPÄISCHE UNION. Verordnung (EU) Nr. 517/2014 des Europäischen Parlaments und des Rates vom 16. April 2014 über fluorierte Treibhausgase und zur Aufhebung der Verordnung (EG) Nr. 842/2006.

[42] FAN, W., JI, W., WANG, L., ZHENG, L., AND WANG, Y. A review on cutting tool technology in machining of Ni-based superalloys. *The International Journal of Advanced Manufacturing Technology 110*, 11-12 (2020), 2863–2879.

[43] FAUTH, M. Projekt Cool Tool-Abschlussbericht, Part of Mathias Fauth. *Verwertugnsnachweis der ZIM-Projekte* (2021).

[44] FEINER, M., ARNEMANN, M., AND KIPFMÜLLER, M. Development of an adjustable spiral-shaped evaporator. *Proceedings of the International Refrigeration and Air Conditioning Conference* (2018).

[45] FEINER, M., FAUTH, M., PEREZ, E., AND FAEHNDRICH, P. German Patent Application No. 102021204547.2 with the German Patent and Trademark Office in Munich on May 5, 2021, 2021.

[46] FEINER, M., FERNÁNDEZ GARCÍA, F. J., ARNEMANN, M., AND KIPFMÜLLER, M. Hydraulic characterization of a adjustable spiral-shaped evaporator. *Proceedings of the International Refrigeration and Air Conditioning Conference* (2021).

[47] FEINER, M., FERNÁNDEZ GARCÍA, F. J., ARNEMANN, M., AND KIPFMÜLLER, M. Hydraulic optimization of an adjustable spiral-shaped evaporator. *International Journal of Mechanical and Mechatronics Engineering 15*, 2 (2021), 113 – 119.

[48] FOSTER, H., AND ZUBER, N. Dynamics of vapor bubbles and boiling heat transfer. *AIChE J 1*, 4 (1955), 531–535.

[49] FRANK, A. Helical Coil Calculator. URL: `https://www.changpuak.ch/electronics/calc_21.php`, accessed on 14. 11. 2020.

[50] FRIEDEL, L. Improved friction pressure drop correlation for horizontal and vertical two-phase pipe flow. *Proc. of European Two-Phase Flow Group Meet., Ispra, Italy, 1979* (1979).

[51] GAMMACK, D., AND HYDON, P. Flow in pipes with non-uniform curvature and torsion. *Mathematics 433* (04 2001).

[52] GARCIA, F., GARCIA, R., PADRINO, J., MATA, C., TRALLERO, J., AND JOSEPH, D. Power law and composite power law friction factor correlations for laminar and turbulent gas–liquid flow in horizontal pipelines. *International Journal of Multiphase Flow 29*, 10 (2003), 1605–1624.

[53] GORENFLO, D. H2 Behältersieden reiner Stoffe und von Gemischen. In *VDI-Wärmeatlas*, P. Stephan, S. Kabelac, M. Kind, D. Mewes, K. Schaber, and T. Wetzel, Eds., vol. 17 of *VDI Springer Reference*. Springer Berlin Heidelberg, Berlin, Heidelberg, 2019, pp. 909–958.

[54] GROENEVELD, D. C., SHAN, J. Q., VASIĆ, A. Z., LEUNG, L., DURMAYAZ, A., YANG, J., CHENG, S. C., AND TANASE, A. The 2006 CHF look-up table. *Nuclear Engineering and Design 237*, 15-17 (2007), 1909–1922.

[55] GRÖNNERUD, R. Investigation of liquid hold-up, flow-resistance and heat transfer in circulation type evaporators, part IV: two-phase flow resistance in boiling refrigerants. *Bull. De l'Inst. Du Froid, Annexe 1* (1972).

[56] GUNGOR, K. E., AND WINTERTON, R. A general correlation for flow boiling in tubes and annuli. *International Journal of Heat and Mass Transfer 29*, 3 (1986), 351–358.

[57] HARDIK, B., AND PRABHU, S. Boiling pressure drop, local heat transfer distribution and critical heat flux in helical coils with R123. *International Journal of Thermal Sciences 125* (2018), 149–165.

[58] HARDIK, B., AND PRABHU, S. Heat transfer distribution in helical coil flow boiling system. *International Journal of Heat and Mass Transfer 117* (2018), 710–728.

[59] HARDIK, B. K., AND PRABHU, S. V. Two-phase pressure drop in a helical coil flow boiling system. *Heat and Mass Transfer 54*, 11 (2018), 3231–3251.

[60] HERBST, O. H3.6 Strömungssieden – Kritische Siedezustände. In *VDI-Wärmeatlas*, P. Stephan, S. Kabelac, M. Kind, D. Mewes, K. Schaber, and T. Wetzel, Eds., vol. 33 of *VDI Springer Reference*. Springer Berlin Heidelberg, Berlin, Heidelberg, 2019, pp. 1015–1060.

[61] HETSRONI, G., MOSYAK, A., POGREBNYAK, E., AND SEGAL, Z. Periodic boiling in parallel micro-channels at low vapor quality. *International Journal of Multiphase Flow 32*, 10-11 (2006), 1141–1159.

[62] HEWITT, G. F., AND ROBERTS, D. Studies of two-phase flow patterns by simultaneous x-ray and flast photography. Tech. rep., Atomic Energy Research Establishment, Harwell, England (United Kingdom), 1969.

[63] HUMPFER, F. *Erhöhen des Kühlvermögens von Spot-Verdampfern bei hohen Wärmestromdichten durch Erzeugung einer Drallströmung (Unpublished master's thesis)*. 2013.

[64] HUMPFER, F., KNIPPING, T., AND HAAS, R. Energieeffizienz durch Kühlung von Hot-Spots in Spritzgießwerkzeugen. *Fachkongress Feinwerktechnik* (2012).

[65] ISHIDA, K. *Two-phase flow with heat transfer in helically-coiled tubes.* PhD thesis, Imperial College London (University of London), 1981.

[66] JUNGNICKEL, H., AGSTEN, R., AND KRAUS, E. *Grundlagen der Kältetechnik*, 3., stark bearb. aufl. ed. Verl. Technik GmbH, Berlin, 1990.

[67] KATSAOUNIS, A. H3.7 Strömungssieden – Wärmeübergang nach der Siedekrise. In *VDI-Wärmeatlas*, P. Stephan, S. Kabelac, M. Kind, D. Mewes, K. Schaber, and T. Wetzel, Eds., vol. 225 of *VDI Springer Reference*. Springer Berlin Heidelberg, Berlin, Heidelberg, 2019, pp. 1061–1083.

[68] KATTO, Y., AND KUNIHIRO, M. Study of the mechanism of burn-out in boiling system of high burn-out heat flux. *Bulletin of JSME 16*, 99 (1973), 1357–1366.

[69] KEW, P. A., AND CORNWELL, K. Correlations for the prediction of boiling heat transfer in small-diameter channels. *Applied thermal engineering 17*, 8-10 (1997), 705–715.

[70] KIM, J.-W., IM, Y.-B., AND KIM, J.-S. A study on performance analysis of the helically coiled evaporator with circular minichannels. *Journal of mechanical science and technology 20*, 7 (2006), 1059–1067.

[71] KIM, J.-W., KIM, J.-H., AND KIM, J.-S. A study on the helically coiled heat exchanger of small diameter tubes. *Transactions of the Korean Society of Mechanical Engineers B 25*, 11 (2001), 1492–1499.

[72] KIM, J.-W., KIM, J.-H., SEO, S.-K., KIM, J.-H., AND KIM, J.-S. Characteristics of heat transfer and pressure drop of r-22 inside an evaporating tube with small diameter helical coil. *Transactions of the Korean Society of Mechanical Engineers B 24*, 5 (2000), 699–708.

[73] KIND, M., AND WETZEL, T. H3.2 Strömungssieden – Strömungsformen in Verdampferrohren. In *VDI-Wärmeatlas*, P. Stephan, S. Kabelac, M. Kind, D. Mewes, K. Schaber, and T. Wetzel, Eds., vol. 26 of *VDI Springer Reference*. Springer Berlin Heidelberg, Berlin, Heidelberg, 2019, pp. 965–971.

[74] KLEPPMANN, W. *Versuchsplanung: Produkte und Prozesse optimieren.* Carl Hanser Verlag GmbH Co KG, 2020.

[75] KNIPPING, T. *Kühlen kleiner Kavitäten mit verdampfenden Fluiden.* DKV Deutscher Kälte-und Klimatechnischer Verein e.V., 2017.

[76] KNIPPING, T., ARNEMANN, M., HESSE, U., AND HUMPFER, F. Experimental analysis of twisted shaped spot evaporators at high heat fluxes.

[77] KNIPPING, T., ARNEMANN, M., HUMPFER, F., AND HANSEL, S. Interne Dokumentation der Projektergebnisse Spritzgusskülung.

[78] KNIPPING, T., ARNEMANN, M., HUMPFER, F., AND MÜLLER, T. Interne Dokumentation der Projektergebnisse im Projekt Cool Move.

[79] KNIPPING, T., ARNEMANN, M., HUMPFER, F., AND MÜLLER, T. Spot-Verdampfer-Verbund zur Kühlung von Elektromotoren. *KI Kälte · Luft · Klimatechnik 185*, 4 (2017), 51–55.

[80] KNIPPING, T., AND FEINER, M. Projekt Cool Tool-Abschlussbericht. *Verwertugnsnachweis der ZIM-Projekte 2*, 1 (2021), 15.

[81] KNIPPING, T., AND MOERK, T. Projekt Cool Tool-Abschlussbericht, Part of MAS. *Verwertugnsnachweis der ZIM-Projekte*.

[82] LAKESTANI, M., AND DEHGHAN, M. The use of chebyshev cardinal functions for the solution of a partial differential equation with an unknown time-dependent coefficient subject to an extra measurement. *Journal of Computational and Applied Mathematics 235*, 3 (2010), 669–678.

[83] LAZAREK, G. M., AND BLACK, S. H. Evaporative heat transfer, pressure drop and critical heat flux in a small vertical tube with R-113. *International Journal of Heat and Mass Transfer 25*, 7 (1982), 945–960.

[84] LEE, J., AND MUDAWAR, I. Two-phase flow in high-heat-flux micro-channel heat sink for refrigeration cooling applications: Part II—heat transfer characteristics. *International Journal of Heat and Mass Transfer 48*, 5 (2005), 941–955.

[85] LEIDENFROST, J. G. De aquæ communis nonnullis qualitatibus tractatus. *Hermann Ovenius, Duisburg 1756, Nachdruck H. W. Cramer, Duisburg 1796* (1756).

[86] LI, H., AND HRNJAK, P. Measurement of heat transfer coefficient and pressure drop during evaporation of R134a in new type facility with one pass flow through microchannel tube. *International Journal of Heat and Mass Transfer 115*, 8 (2017), 502–512.

[87] LI, H., AND HRNJAK, P. Heat transfer and pressure drop of R32 evaporating in one pass microchannel tube with parallel channels. *International Journal of Heat and Mass Transfer 127* (2018), 526–540.

[88] Li, M., Dang, C., and Hihara, E. Flow boiling heat transfer of HFO1234yf and R32 refrigerant mixtures in a smooth horizontal tube: Part I. experimental investigation. *International Journal of Heat and Mass Transfer 55*, 13-14 (2012), 3437–3446.

[89] Lindeman, B. A., Anderson, J. M., and Shedd, T. A. Predictive model for heat transfer performance of oblique and normally impinging jet arrays. *International Journal of Heat and Mass Transfer 62* (2013), 612–619.

[90] Liu, C.-S. Finding unknown heat source in a nonlinear cauchy problem by the lie-group differential algebraic equations method. *Engineering Analysis with Boundary Elements 50* (2015), 148–156.

[91] Lockhalt, R., and Martinelli, R. Proposed correlation of data for isothermal two-phase, two-component flow in pipes, Chent Eng. In *Proc* (1949), vol. 58, pp. 62–65.

[92] Macian, R., Cebull, P., Coddington, P., and Paulsen, M. Implementation of an improved interfacial mass and energy transfer model in retran-3d. *Nuclear technology 128*, 2 (1999), 139–152.

[93] Manno, M., Yang, B., Khanna, S., McCluskey, P., and Bar-Cohen, A. Microcontact-enhanced thermoelectric cooling of ultrahigh heat flux hotspots. *IEEE Transactions on Components, Packaging and Manufacturing Technology 5*, 12 (2015), 1775–1783.

[94] Martinelli, R. Prediction of pressure drop during forced-circulation boiling of water. *Trans. of the ASME 70* (1948), 695–702.

[95] Mauro, A., Thome, J., Toto, D., and Vanoli, G. P. Saturated critical heat flux in a multi-microchannel heat sink fed by a split flow system. *Experimental Thermal and Fluid Science 34*, 1 (2010), 81–92.

[96] Mohebbi, A., and Dehghan, M. High-order scheme for determination of a control parameter in an inverse problem from the over-specified data. *Computer Physics Communications 181*, 12 (2010), 1947–1954.

[97] Monde, M., and Katto, Y. Burnout in a high heat-flux boiling system with an impinging jet. *International Journal of Heat and Mass Transfer 21*, 3 (1978), 295–305.

[98] Moody, L. F. Friction factors for pipe flow. *Trans. Asme 66* (1944), 671–684.

[99] Moore, G. E. Cramming more components onto integrated circuits. *Proceedings of the IEEE 86*, 1 (1998), 82–85.

[100] Mudawar, I., and Estes, K. Optimizing and predicting CHF in spray cooling of a square surface. 672–679.

[101] Mulero, A., Cachadiña, I., and Bautista, D. Recommended correlations for the surface tension of n-alkanes. *Journal of Physical and Chemical Reference Data 50*, 2 (2021), 023104.

[102] Müller, B. *Thermische analyse des Zerspanens metallischer Werkstoffe bei hohen Schnittgeschwindigkeiten.* PhD thesis, Bibliothek der RWTH Aachen, 2004.

[103] MÜLLER-STEINHAGEN, H., AND HECK, K. A simple friction pressure drop correlation for two-phase flow in pipes. *Chemical Engineering and Processing: Process Intensification 20*, 6 (1986), 297–308.

[104] MUMM, J. Heat transfer to boiling water forced through a uniformly heated tube. Tech. rep., Argonne National Lab., 1954.

[105] NGUYEN, T.-B., LIU, D., KAYES, M. I., WANG, B., RASHIN, N., LEU, P. W., AND TRAN, T. Critical heat flux enhancement in pool boiling through increased rewetting on nanopillar array surfaces. *Scientific reports 8*, 1 (2018), 4815.

[106] NIRSCHL, H. L1.3 Druckverlust in durchströmten Leitungen mit Querschnittsänderungen. In *VDI-Wärmeatlas*, P. Stephan, S. Kabelac, M. Kind, D. Mewes, K. Schaber, and T. Wetzel, Eds., vol. 72 of *VDI Springer Reference*. Springer Berlin Heidelberg, Berlin, Heidelberg, 2019, pp. 1363–1373.

[107] NOACK, K. Wie berechne ich die gestreckte Drahtlänge einer Feder. URL: `https://www.mathelounge.de/44112/wie-berechne-ich-die-gestreckte-drahtlange-einer-feder`, accessed on 12.11.2020.

[108] NUKIYAMA, S. Film boiling water on thin wires. *Soc. Mech. Engng., Japan. 37.* (1934).

[109] PAUL HORN GMBH. Technologievorsprung für die Skills CNC-Fräsen und CNC-Drehen. URL: `https://euroskills2021.com/technologievorsprung-fuer-cnc-fraesen-und-drehen/`, accessed on 17.11.2020.

[110] PAUTSCH, A. G., AND SHEDD, T. A. Spray impingement cooling with single-and multiple-nozzle arrays. part I: Heat transfer data using FC-72. *International Journal of Heat and Mass Transfer 48*, 15 (2005), 3167–3175.

[111] PENTENRIEDER, B. Finite element solutions of heat conduction problems in complicated 3D geometries using the multigrid method. *Fakultat fur Informatik, TU Munchen, Munich, Germany 8* (2005).

[112] POLIFKE, W., AND KOPITZ, J. *Wärmeübertragung: Grundlagen, analytische und numerische Methoden*, 2., aktualisierte Auflage ed. Ing - Maschinenbau. Pearson Studium, München, 2009.

[113] QI, S., ZHANG, P., WANG, R., AND XU, L. Flow boiling of liquid nitrogen in micro-tubes: Part ii–heat transfer characteristics and critical heat flux. *International journal of heat and mass transfer 50*, 25-26 (2007), 5017–5030.

[114] R.J. GOLDSTEIN, AND M.E. FRANCHETT. Heat transfer from a flat surface to an oblique impinging jet.

[115] RODAY, A., AND JENSEN, M. Study of the critical heat flux condition with water and R-123 during flow boiling in microtubes. Part I: Experimental results and discussion of parametric effects. *International Journal of Heat and Mass Transfer 52*, 13-14 (2009), 3235–3249.

[116] RODAY, A., AND JENSEN, M. Study of the critical heat flux condition with water and R-123 during flow boiling in microtubes. Part II–Comparison of data with correlations and establishment of a new subcooled CHF correlation. *International Journal of Heat and Mass Transfer 52*, 13-14 (2009), 3250–3256.

[117] ROUHANI, S. Z., AND AXELSSON, E. Calculation of void volume fraction in the sub-cooled and quality boiling regions. *International Journal of Heat and Mass Transfer 13*, 2 (1970), 383–393.

[118] SAADATMANDI, A., AND DEHGHAN, M. Computation of two time-dependent coefficients in a parabolic partial differential equation subject to additional specifications. *International Journal of Computer Mathematics 87*, 5 (2010), 997–1008.

[119] SAHA, S. K. *Microchannel Phase Change Transport Phenomena*. Butterworth-Heinemann, 2015.

[120] SCHMIDT, H., WELLENHOFER, A., MUSCHELKNAUTZ, S., SCHMIDT, J., SCHMIDT, J., MEWES, D., MERSMANN, A., AND STICHLMAIR, J. *L2 Zweiphasige Gas-Flüssigkeitsströmungen*. Springer Berlin Heidelberg, Berlin, Heidelberg, 2013, pp. 1285–1358.

[121] SCHWARZ, H. R., AND KÖCKLER, N. *Partielle Differenzialgleichungen*. Vieweg+Teubner, Wiesbaden, 2009, pp. 427–486.

[122] SHAH, M. M. Chart correlation for saturated boiling heat transfer: equations and further study. *ASHRAE transactions 88* (1982).

[123] SHAMSI, M., AND DEHGHAN, M. Determination of a control function in three-dimensional parabolic equations by legendre pseudospectral method. *Numerical Methods for Partial Differential Equations 28*, 1 (2012), 74–93.

[124] SHANNON, C. E. Communication in the presence of noise. *Proceedings of the IRE 37*, 1 (1949), 10–21.

[125] SHEDD, T. A. Next generation spray cooling: high heat flux management in compact spaces. *Heat Transfer Engineering 28*, 2 (2007), 87–92.

[126] SONG, H. *Engineering Fluid Mechanics*. Springer Singapore, Singapore, 2018.

[127] SPURK, J., AND AKSEL, N. *Strömungslehre*. Springer Berlin Heidelberg, Berlin, Heidelberg, 2019.

[128] STEIN, M. *Systematische Untersuchung der kritischen Wärmestromdichte beim Strömungssieden von Wasser in lotrechten Kreisrohren mit und ohne poröser Beschichtung*. PhD thesis, 2004.

[129] STEMKE GMBH. Stemke-Kühlung. URL: https://www.plastverarbeiter.de/verarbeitungsverfahren/spritzgiessen/stemke-kuehlung.html, accessed on 16.11.2020.

[130] STEPHAN, P., KABELAC, S., KIND, M., MEWES, D., SCHABER, K., AND WETZEL, T., Eds. *VDI-Wärmeatlas: Fachlicher Träger VDI-Gesellschaft Verfahrenstechnik und Chemieingenieurwesen*, 12. aufl. 2019 ed. VDI Springer Reference. Springer Berlin Heidelberg, Berlin, Heidelberg, 2019.

[131] STOLZ JR, G. Numerical solutions to an inverse problem of heat conduction for simple shapes.

[132] SUN, L., AND MISHIMA, K. An evaluation of prediction methods for saturated flow boiling heat transfer in mini-channels. *International Journal of Heat and Mass Transfer 52*, 23-24 (2009), 5323–5329.

[133] TAITEL, Y., AND DUKLER, A. E. A model for predicting flow regime transitions in horizontal and near horizontal gas-liquid flow. *AIChE journal 22*, 1 (1976), 47–55.

[134] TILLNER-ROTH, R., AND YOKOZEKI, A. An international standard equation of state for difluoromethane (R-32) for temperatures from the triple point at 136.34 K to 435 K and pressures up to 70 MPa. *Journal of Physical and Chemical Reference Data 26*, 6 (1997), 1273–1328.

[135] TRAN, T., WAMBSGANSS, M., AND FRANCE, D. Small circular-and rectangular-channel boiling with two refrigerants. *International Journal of Multiphase Flow 22*, 3 (1996), 485–498.

[136] TRÄNKLER, H.-R., AND FISCHERAUER, G., Eds. *Das Ingenieurwissen: Messtechnik.* Springer Berlin Heidelberg, Berlin, Heidelberg, 2014.

[137] VANDERVORT, C., BERGLES, A., AND JENSEN, M. An experimental study of critical heat flux in very high heat flux subcooled boiling. *International Journal of Heat and Mass Transfer 37* (1994), 161–173.

[138] WESTKÄMPER, E., AND LÖFFLER, C. *Visionen und strategische Konzepte für das System Produktion.* Vieweg+Teubner Verlag, 2016.

[139] W.J. MINKOWYCZ, E.M.SPARROW, G., AND R.H.PLETCHER. *Handbook. of Numerical Heat Transfer.* John Wiley and Sons, New York, 1988.

[140] YAGOV, V. The mechanism of the pool boiling crisis. *Thermal Engineering 50*, 3 (2003), 175–183.

[141] YAGOV, V. Critical heat flux prediction for pool boiling of binary mixtures. *Chemical Engineering Research and Design 82*, 4 (2004), 457–461.

[142] YAGOV, V. V. Heat transfer and crisis in swirl flow boiling. *Experimental Thermal and Fluid Science 29*, 7 (2005), 871–883.

[143] YI, J., LIU, Z.-H., AND WANG, J. Heat transfer characteristics of the evaporator section using small helical coiled pipes in a looped heat pipe. *Applied thermal engineering 23*, 1 (2003), 89–99.

[144] YOUNG, M. A., AND BELL, K. J. Review of two-phase flow and heat transfer phenomena in helically coiled tubes. In *AIP Conference Proceedings* (1991), vol. 217, American Institute of Physics, pp. 1214–1223.

[145] YU, W., FRANCE, D., WAMBSGANSS, M., AND HULL, J. Two-phase pressure drop, boiling heat transfer, and critical heat flux to water in a small-diameter horizontal tube. *International Journal of Multiphase Flow 28*, 6 (2002), 927–941.

[146] ZHAO, J.-F., WANG, A.-L., AND YANG, C.-X. Prediction of thermal contact conductance based on the statistics of the roughness profile characteristics. *International journal of heat and mass transfer 48*, 5 (2005), 974–985.

A. Appendix

A.1. Example of the two-phase Pressure Drop

The two-phase pressure drop consists of the static-, momentum- and the frictional pressure drop [37]

$$\Delta p_{\text{total}} = \Delta p_{\text{frict}} + \Delta p_{\text{mom}} + \Delta p_{\text{static}}. \tag{A.1}$$

For a horizontal tube the geodetic pressure drop has no change this results in

$$\Delta p_{\text{total}} = \Delta p_{\text{frict}} + \Delta p_{\text{mom}}. \tag{A.2}$$

The momentum pressure drop depends on the change in the kinematic energy of the fluid

$$\Delta p_{\text{mom}} = G_{\text{total}}^2 \cdot \left\{ \left[\frac{(1-x)^2}{\varrho_{\text{L}}(1-\varepsilon)} + \frac{x^2}{\varrho_{\text{G}} \cdot \varepsilon} \right]_{\text{out}} - \left[\frac{(1-x)^2}{\varrho_{\text{L}}(1-\varepsilon)} + \frac{x^2}{\varrho_{\text{G}} \cdot \varepsilon} \right]_{\text{in}} \right\}. \tag{A.3}$$

Where x is the vapor quality and G_{total} is the total mass flux of the two-phase fluid.

With the void fraction from Steiner [130] and the drift flux model from Rouhani and Axelsson [117] for horizontal tubes results to

$$\varepsilon = \frac{x}{\varrho_{\text{G}}} \cdot \left[(1 + 0.12 \cdot (1-x)) \left(\frac{x}{\varrho_{\text{G}}} + \frac{1-x}{\varrho_{\text{L}}} \right) + \frac{1.18 \cdot (1-x)[g \cdot \sigma(\varrho_{\text{L}} - \varrho_{\text{G}})]}{0.25 G^2 \cdot \varrho_{\text{L}}^{0.5}} \right]^{-1}. \tag{A.4}$$

The momentum pressure drop is calculable if the experimental values for the vapour quality of inlet and outlet are used. The frictional pressure drop can be calculated by subtracting the measured total pressure drop minus the momentum pressure drop using Equation A.2

$$\Delta p_{\text{frict}} = \Delta p_{\text{total}} - \Delta p_{\text{mom}}. \tag{A.5}$$

To calculate the frictional two-phase pressure drop there are several correlation available. A few proven correlations are described below.
The method from Friedel [50] is used for vapor qualities from $0 \leq x < 1$ and using a two-phase factor Φ_{L},

$$\Delta p_{\text{frict}} = \Delta p_{\text{L}} \cdot \Phi_{\text{L}}^2. \tag{A.6}$$

where Δp_{L} is calculated for the liquid-phase. G is the mass flux. It is determined by

dividing the mass flow $\dot{m}$ by the hydraulic cross-section A_{hyd}

$$\Delta p_{\text{L}} = 4 \cdot f_{\text{L}} \cdot (L/d_{\text{hyd}}) \cdot G^2 \cdot (1 - x)^2 \cdot \left(\frac{1}{2 \cdot \varrho_{\text{L}}} \right), \tag{A.7}$$

with the liquid friction factor

$$f_{\text{L}} = \frac{0.079}{Re^{0.25}} \tag{A.8}$$

and the Reynolds number using the liquid dynamic viscosity η_{L},

$$Re = \frac{G \cdot d_{\text{hyd}}}{\eta_{\text{L}}}. \tag{A.9}$$

The two-phase factor is calculated as

$$\Phi_{\text{L}}^2 = E + \frac{3.24 \cdot F \cdot H}{Fr_{\text{h}}^{0.045} \cdot We_{\text{L}}^{0.035}}, \tag{A.10}$$

where E, F, H and Fr are specified with the following equations,

$$E = (1 - x)^2 + x^2 \cdot \frac{\varrho_{\text{L}} \cdot f_{\text{G}}}{\varrho_{\text{G}} \cdot f_{\text{L}}}, \tag{A.11}$$

$$F = x^{0.078} \cdot (1 - x)^{0.224}, \tag{A.12}$$

$$H = \left(\frac{\varrho_{\text{L}}}{\varrho_{\text{G}}} \right)^{0.91} \cdot \left(\frac{\eta_{\text{L}}}{\eta_{\text{G}}} \right)^{0.19} \cdot \left(1 - \frac{\eta_{\text{L}}}{\eta_{\text{G}}} \right)^{0.71}, \tag{A.13}$$

and

$$Fr_{\text{h}} = \frac{G_{\text{total}}^2 \cdot d_{\text{hyd}}}{g \cdot d_{\text{i}} \cdot \varrho_{\text{h}}^2}. \tag{A.14}$$

The Weber number for liquids is defined as

$$We_{\text{L}} = \frac{G_{\text{total}} \cdot d_{\text{hyd}}}{\sigma \cdot \varrho_{\text{h}}}. \tag{A.15}$$

Homogeneous density consist of the vapour quality, the gaseous and liquid density

$$\varrho_{\text{h}} = \left(\frac{x}{\varrho_{\text{G}}} + \frac{1 - x}{\varrho_{\text{L}}} \right)^{-1}. \tag{A.16}$$

The Friedel method is used for ratios of $\frac{\eta_{\mathrm{L}}}{\eta_{\mathrm{G}}} < 1000$. The indices might be a little bit confusing at first sight. The indice h references to the Friedel method and Fr to the Froude number. Grönneruds [55] correlation

$$\Delta p_{\mathrm{frict}} = \Phi_{\mathrm{gd}} \cdot \Delta p_{\mathrm{L}} \tag{A.17}$$

was specially developed for pressure drop with refrigerants and is valid for vapor contents of $0 < x \leq 1$. The single-phase pressure drop is defined as

$$\Delta p_{\mathrm{L}} = 4 f_{\mathrm{L}} \cdot \left(\frac{L}{d_{\mathrm{hyd,swirl}}} \right) \cdot G_{\mathrm{total}}^2 \cdot (1 - x)^2 \cdot \left(\frac{1}{2 \varrho_{\mathrm{L}}} \right). \tag{A.18}$$

With the two-phase multiplier factor

$$\Phi_{\mathrm{gd}} = 1 + \left(\frac{dp}{dz} \right)_{\mathrm{Fr}} \left[\frac{\varrho_{\mathrm{L}}}{\varrho_{\mathrm{G}} \cdot \left(\frac{\eta_{\mathrm{L}}}{\eta_{\mathrm{G}}} \right)^{0.25}} - 1 \right], \tag{A.19}$$

where the indice Fr references to the Froude number. The two-phase multiplier is a function of

$$\left(\frac{dp}{dz} \right)_{\mathrm{Fr}} = f_{\mathrm{Fr}} \cdot \left[x + 4 \cdot \left(x^{1.8} - x^{10} \cdot f_{\mathrm{Fr}}^{0.5} \right) \right]. \tag{A.20}$$

For the condition $Fr_{\mathrm{L}} \geq 1$, the Froude friction factor f_{Fr} is set to 1. If $Fr_{\mathrm{L}} < 1$, the following relationship

$$f_{\mathrm{Fr}} = Fr_{\mathrm{L}}^{0.3} + 0.0055 \cdot \left(\ln \left(\frac{1}{Fr_{\mathrm{L}}} \right) \right)^2 \tag{A.21}$$

applies with

$$Fr_{\mathrm{L}} = \frac{G_{\mathrm{total}}}{g \cdot d_{\mathrm{hyd}} \cdot \varrho_{\mathrm{L}}^2}. \tag{A.22}$$

Another correlation for the two-phase frictional pressure drop is the method of Müller-Steinhagen and Heck [103]

$$\left(\frac{dp}{dz} \right)_{\mathrm{frict}} = G \cdot (1 - x)^{\frac{1}{3}} + \left(\frac{dp}{dz} \right)_{\mathrm{Go}} \cdot x^3, \tag{A.23}$$

with G as

$$G = \left(\frac{dp}{dz} \right)_{\mathrm{Lo}} + 2 \cdot \left(\left(\frac{dp}{dz} \right)_{\mathrm{Go}} - \left(\frac{dp}{dz} \right)_{\mathrm{Lo}} \right) \cdot x \tag{A.24}$$

and

$$\left(\frac{dp}{dz}\right)_{\text{Lo}} = f_{\text{L}} \cdot \frac{2 \cdot G_{\text{total}}}{d_{\text{hyd}} \cdot \varrho_{\text{L}}} \tag{A.25}$$

and

$$\left(\frac{dp}{dz}\right)_{\text{Go}} = f_{\text{G}} \cdot \frac{2 \cdot G_{\text{total}}^2}{d_{\text{hyd}} \cdot \varrho_{\text{G}}}. \tag{A.26}$$

Where $(dp/dz)_{\text{Lo}}$ is for the frictional pressure gradient of the liquid flow and $(dp/dz)_{\text{Go}}$ for the frictional pressure gradient of the vapor flow used from the Chisholm correlation [27]. This correlation is an empirical two-phase extrapolation between the total fluid flow and the total vapor flow thus it is applicable for vapor contents of the fluid of $0 \leq x < 1$.

B. Appendix

B.1. Experiments for HTC Verification

Table B.1.: Experiments conducted to verify the HTC-correlations

No.	Pitch	d_{hyd} in mm	p_{o} in bar	p_{c} in bar	P_{el} in W	$\dot{m}$ in kg/h
1	2	0.84	3.55	9.80	220	3.35
2	2	0.84	3.50	9.73	230	3.27
3	2	0.84	3.46	9.63	240	3.23
4	2	0.84	3.41	9.57	249	3.15
5	2	0.84	3.37	9.54	260	3.13
6	3	1.27	3.41	9.42	200	3.21
7	3	1.27	3.41	9.40	205	3.19
8	3	1.27	3.40	9.38	218	3.16
9	3	1.27	3.36	9.39	227	3.15
10	3	1.27	3.36	9.38	239	3.14
11	3	1.27	3.37	9.40	259	3.06
12	3	1.27	3.29	9.53	238	3.05
13	3	1.27	3.27	9.51	249	3.05
14	3	1.27	3.05	9.50	240	3.30
15	3	1.27	3.16	9.44	250	3.26
16	3	1.27	3.18	9.42	260	3.22
17	3	1.27	2.91	9.40	270	3.24
18	5	1.49	3.24	9.54	220	3.06
19	5	1.49	3.27	9.53	229	3.09
20	5	1.49	3.28	9.51	237	2.98
21	5	1.49	3.23	9.51	241	3.00
22	5	1.49	3.20	9.53	250	3.00
23	2	0.84	3.42	9.54	220	3.21
24	2	0.84	3.36	9.53	230	3.14
25	2	0.84	3.30	9.60	240	3.06
26	2	0.84	3.26	9.66	250	3.02
27	2	0.84	3.25	9.68	255	3.00
28	2	0.84	3.55	9.80	220	3.35
29	2	0.84	3.50	9.73	230	3.27
30	2	0.84	3.46	9.63	240	3.23
31	2	0.84	3.41	9.57	249	3.15
32	2	0.84	3.37	9.54	260	3.13
33	2	0.84	3.36	9.57	250	3.18
34	2	0.84	3.21	9.54	260	3.02
35	2	0.84	3.18	9.58	265	2.99
36	3	1.27	3.41	9.42	200	3.21

37	3	1.27	3.41	9.40	205	3.19
38	3	1.27	3.40	9.38	218	3.16
39	3	1.27	3.36	9.39	227	3.15
40	3	1.27	3.36	9.38	240	3.14
41	3	1.27	3.35	9.40	245	3.10
42	3	1.27	3.37	9.41	259	3.06
43	3	1.27	3.29	9.53	238	3.05
44	3	1.27	3.27	9.51	249	3.05
45	3	1.27	3.05	9.50	240	3.30
46	3	1.27	3.16	9.44	250	3.26
47	3	1.27	3.18	9.42	260	3.22
48	3	1.27	2.91	9.40	270	3.24
49	5	1.49	3.24	9.54	220	3.06
50	5	1.49	3.27	9.53	229	3.09
51	5	1.49	3.28	9.51	237	2.97
52	5	1.49	3.23	9.51	241	3.00
53	5	1.49	3.20	9.53	250	3.00
54	5	1.49	3.26	9.40	240	3.02
55	5	1.49	3.23	9.42	250	3.04
56	5	1.49	3.19	9.45	260	2.98
57	6	1.64	3.21	9.53	200	3.07
58	6	1.64	3.23	9.49	202	3.00
59	6	1.64	3.23	9.35	215	3.00
60	6	1.64	3.24	9.49	221	2.99
61	6	1.64	3.23	9.48	230	2.98
62	6	1.64	3.44	9.67	190	3.19
63	6	1.64	3.41	9.62	200	3.20
64	6	1.64	3.39	9.60	210	3.15
65	6	1.64	3.39	9.59	220	3.18
66	6	1.64	3.34	9.57	230	3.10
67	6	1.64	3.30	9.56	240	3.06
68	6	1.64	3.24	9.58	250	3.01
69	6	1.64	3.22	9.60	260	3.04
70	6	1.64	3.13	9.64	270	2.95
71	6	1.64	3.23	9.63	190	3.06
72	6	1.64	3.29	9.62	200	3.00
73	6	1.64	3.29	9.62	210	3.09
74	6	1.64	3.28	9.62	220	3.04
75	6	1.64	3.30	9.62	230	3.05
76	6	1.64	3.27	9.63	240	3.04
77	6	1.64	3.21	9.63	250	2.98
78	6	1.64	3.17	9.64	260	2.96
79	6	1.64	3.08	9.67	270	2.87
80	6	1.64	3.35	9.48	200	3.14
81	6	1.64	3.34	9.49	210	3.10
82	6	1.64	3.36	9.50	220	3.14

83	6	1.64	3.40	9.52	230	3.18
84	6	1.64	3.38	9.50	240	3.12
85	6	1.64	3.37	9.50	250	3.08
86	6	1.64	3.33	9.52	260	3.12
87	6	1.64	3.23	9.58	270	3.01
88	7	1.81	3.26	9.55	220	2.91
89	7	1.81	3.27	9.52	230	3.06
90	7	1.81	3.26	9.51	240	2.99
91	7	1.81	3.19	9.52	250	2.98
92	7	1.81	3.15	9.61	240	2.94
93	7	1.81	3.29	9.53	190	3.05
94	7	1.81	3.27	9.51	200	3.05
95	7	1.81	3.25	9.50	210	3.02
96	7	1.81	3.26	9.52	220	3.00
97	7	1.81	3.25	9.52	230	3.01
98	7	1.81	3.23	9.54	240	3.01
99	7	1.81	3.20	9.56	250	2.99
100	7	1.81	3.15	9.58	260	2.92
101	7	1.81	3.08	9.63	270	2.81
102	7	1.81	3.35	9.48	200	3.14
103	7	1.81	3.34	9.49	210	3.10
104	7	1.81	3.36	9.50	220	3.14
105	7	1.81	3.40	9.52	230	3.19
106	7	1.81	3.37	9.50	240	3.12
107	7	1.81	3.38	9.50	250	3.09
108	7	1.81	3.34	9.52	260	3.11
109	7	1.81	3.23	9.58	270	3.01

C. Appendix

C.1. Advice for Practitioners

Due to the good surface qualities, micro casting is the most suitable additive manufacturing method for producing swirl geometries. The AlSi7Mg0.6 alloy is recommended here because it can also be used to cast fine structures and offers a good compromise between strength and thermal conductivity. Alternatively, the copper alloy CuBe2 can be used. The use of the pure elements aluminum and copper has not proven itself in practice because they are relatively soft and therefore do not have the necessary dimensional stability. If this is not possible for reasons of time or cost (for example in developing countries), the use of commercially available screws is also possible as an alternative. In case high thermal conductivity of the material should be taken into account and, for example, brass screws should be preferred to stainless steel screws. The use of stereolithography or fused filament fabrication (FFF) 3D printing processes for the production of swirl geometries is suitable at best as a temporary solution or to quickly try something out. Many resins and plastics swell in R-32, and due to the extreme temperature fluctuations, the polymers and resins age faster, become brittle and break easily. It is therefore not advisable to use it permanently in the evaporator.